POLITECNICO DI TORINO

Master's degree in Electronics Engineering

Laser processes for the secondary agro-industry packaging

Supervisors
Prof. Luciano Scaltrito
Prof.ssa Valentina Bertana

Candidate
Paolo Cutillo

A.Y.: 2024-2025

A chi mi vuole bene

Summary

The goal of this thesis is to study the reliability of the LIG (Laser Induced Graphene) process applied to the realization of smart tags for the secondary agro-industry packaging. The LIG process consists in the localized pyrolysis of carbon-based substrates after a direct laser treatment, which induces a photothermal reaction on the surface of the substrate. Thanks to this mechanism, carbon atoms are rearranged to form graphitic structures. In this way conductive porous graphene can be patterned on the material's surface. Nowadays, the secondary agro industrial sector results to be a huge source of worldwide resource consumption. To optimize the resource employment and hence to avoid wastes, smart packaging solutions can be significantly useful and so be integrated in the supply chain. The LIG process, applied to secondary agro-industry packaging materials, can significantly decrease the usage of fossil-based materials enabling to integrate advanced functionalities to the package; such as implementing an integrated antenna for monitoring the product handling and storage conditions. This makes it possible to add functionalities to the package without the need for any labels or inks. Emission frequency, resolution, number of repetitions, scan velocity and the emitting power of the laser can be adjusted to achieve the optimal level of homogeneity of the grown graphene and at the same time to avoid the formation of burnt areas all around the pattern. In this study, the optimization of the LIG process and the subsequent DC and frequency characterization of the implemented graphene tracks have been performed. This also allows to achieve a high degree of flexibility in terms of shape and design of the pattern.

Acknowledgements

Grazie alla mia famiglia, ai miei amici e a Sara, che in questi anni difficili hanno saputo starmi vicino e sopportarmi.
Grazie all'AIA, senza la quale non sarei chi sono oggi.

Contents

List of Tables

List of Figures

Lotta per ciò che ami, sacrificati e non avere rimpianti. Quindi gioisci ed accetta ciò che non è controllabile

Chapter 1

Introduction

1.1 Packaging technologies

Nowadays, the agro-industrial sector is a huge source of worldwide resource consumption. Indeed, the food supply chain requires the employment of resources as the 20% of land, the 70% of water withdrawal and the 32% of the total energy consumption. Furthermore, from the 19% to the 29% of the total greenhouse gas emissions are due to the agro-industrial sector. To optimize the resource employment and hence to avoid waste, smart packaging solutions can be significantly useful whether integrated in the supply chain. Traditional packaging methods rely on fossil-based materials, such as plastic, hence contributing to waste and pollution. Other employable materials for packages can be bamboo baskets, wooden crates or paper-based material, such as CCB (Corrugated Cardboad Boxes). The latter is usually employed for the packaging of horticultural products, such as tomatoes. The previously cited traditional packaging materials present several drawbacks. Those can be the storage and transportation, the handling of bamboo baskets can be challenging as well. Furthermore, wooden craven can be quite expensive and also they can mechanically damage the product. Another important aspect to consider is the use of traditional packages without any advanced functionality. This leads to a lack of control and management of the spoiling process for foods and liquids. An innovation field can hence be the design of integrated sensors in package to detect and monitor the physicochemical and microbiological factors of the products. For these reasons, there is the need to explore sustainable, environmentally friendly and smart solutions for the packaging industry. Fernandez et al. [2023] Khalid et al. [2024]

1.2 Substrates for food packaging

According to the "REGULATION (EU) 2025/40 OF THE EUROPEAN PARLIAMENT AND OF THE COUNCIL", for the period 2010-2021, the 40% of plastics and the 50% of paper used in the European Union (EU) are used in agro-industry packaging. Furthermore, half of the total marine litter is from packaging and packaging constitutes the 36% of municipal solid waste. The trend of the global market in terms of packaging materials

is about the reduction of single-use plastic, improving recycling and refillable solutions. The most used packages vary from plastics, such as polyethylene terephthalate (PET), polyethylene (PE), polypropylene (PP), high-density polyethylene (HDPE), biodegradable plastic such as polylactic acid (PLA), polyhydroxybutyrate (PHB) to paper, cardboard, glass, metals, wood and cork. Commission [a]

1.3 Food packaging legislation

Packaging materials in contact with foods and beverages are called "Food Contact Materials (FCMs)". According to the "REGULATION (EC) No 1935/2004 OF THE EUROPEAN PARLIAMENT AND OF THE COUNCIL", constituents of FCMs must ensure a high level of safety, avoiding any possible contamination of food that can affect the chemical safety of the food and hence affect the human health, as well as the appearance, smell and taste of the product. This legislation applies for all the materials and objects for food contact, including smart packages. On top of that, all the FCMs must be manufactured according to the "COMMISSION REGULATION (EC) No 2023/2006". The "Good Manufacturing Practice (GMP)" encloses all the quality related aspects involved to ensure conformity with the rules applicable to the packaging materials, by guaranteeing the not endangering of the human health, as well as by safeguarding from unacceptable changes both in the composition of the food and in its organoleptic characteristics. At this purpose, the business operator must establish and ensure an effective quality assurance protocol.

The "REGULATION (EU) 2025/40 OF THE EUROPEAN PARLIAMENT AND OF THE COUNCIL" entered into force on the 11^{th} February 2025. This new regulation includes:

- Restrictions on certain single-use plastics
- The aim to minimize the weight and volume of packaging and hence to avoid unnecessary packaging
- The option for costumers to bring their own containers for take-away businesses
- To minimize the use of substances of concern, such as per- and polyfluorinated alkyl substances (PFAS)

This regulation aims to increase the use of recycled plastic, hence to reduce packaging waste through reuse and refill systems and to decrease the use of virgin materials. The goal is to achieve economically viable recyclability of all the packaging by 2030, as well as to set a minimum percentage of recycled content in packaging by 2030-2040 and to reach climate neutrality by 2050. Commission [a] Commission [b]

1.4 Implementation of smart packages

Nowadays, smart packages can be implemented through integrated sensors and smart labels. The most remarkable devices exploited in packages can be:

- **Time Temperature Indicators (TTIs)**: since the temperature variation is a symptom of the spoiling process of food, authors of Fernandez et al. [2023] refer to the possible employment of smart labels that can indicate whether the product is safe to be consumed or not. Indeed, the authors refer that TTIs can be used as smart labels since they can be attached to primary, secondary and pallet packages. An example of a TTI can be appreciated in the figure 1.1

- **Freshness indicators**: the same authors refer also the possibility to implement smart labels which can reveal the chemical reactions based on the spoiling process of food. Those kinds of labels can change color in dependence on the freshness state of the product. Figure 1.2. The indicators are made of two sections: the inner one contains the reagent for the specific chemical compounds released by the food. The outer one acts as a control. The authors also report a smart label produced by 3BP. That smart label can be placed on the package of foods. While the package is intact, the label is white. When the package is opened, the smart label starts becoming darker depending on the freshness of the product. Figure 1.3

- **pH indicators**: other kinds of indicators that can be integrated in labels are pH indicators: indeed, the spoiling process of food is strictly connected with its pH change

- **Gas sensors**: they are used to detect the presence of gases, such as CO_2 (carbon dioxide), O_2 (oxygen), water vapor. Low oxygen levels in the package can extend the product's life, making it not an ideal environment for the growth of bacteria and molds. Oxygen sensors can be implemented by electrochemical sensors, which generate current when in contact with oxygen. A further method to reduce the oxygen levels in the package can be using sachets containing iron-based powder. The latter can react with the water provided by the food, producing an active hydrated metallic reducing agent, which is responsible for reducing the oxygen levels in the package

- **Data carriers**: for instance bar codes, QR (Quick Response) codes and RFID tags (Radio-Frequency IDentification tags). They enable an integrated monitoring of the product throughout the whole supply chain. A remarkable implementation of a QR code relies to the association of a standard QR code to a TTI. Authors of Fernandez et al. [2023] refer to the implementation of a TTI printed with chromatic thermo ink. Hence, it is possible to state if the product has been properly packaged. Figure 1.4. RFID tags consist of a system composed of a radio-frequency antenna, an internal chip and data storage, a reader to interface with the antenna. Fernandez et al. [2023] Biji et al. [2015]

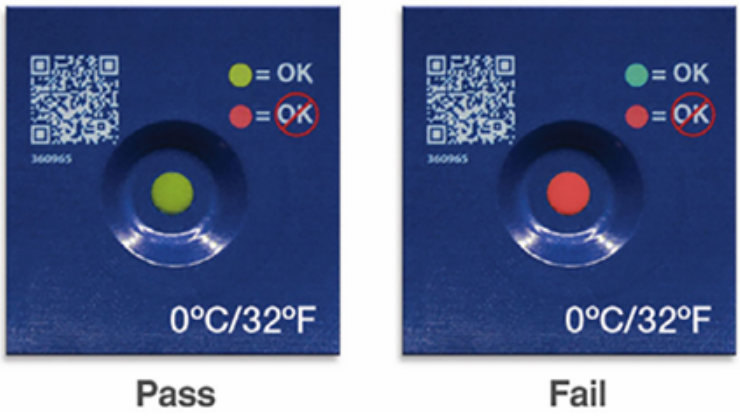

Figure 1.1: Example of a TTI smart label Fernandez et al. [2023]

Figure 1.2: Example of a freshness indicator Fernandez et al. [2023]

Figure 1.3: Smart label developed by 3BP Fernandez et al. [2023]

Figure 1.4: Leftmost: chromatic ink pattern; center: standard QR code; rightmost: smart QR code Fernandez et al. [2023]

1.5 The process of Laser Induced Graphene (LIG)

Laser Induced Graphene (LIG) is a process used to obtain porous graphene-based patterns on a carbon-based substrate. Graphene is a carbon allotrope; it is formed by a single layer of carbon atoms, arranged in a hexagonal lattice. LIG is usually performed by directly applying a CO_2 laser source on a target/substrate material, by inducing photothermal reactions on the surface of the substrate. For instance, during LIG formation on a polymer substrate, the energy carried by the CO_2 laser induces lattice vibrations, which ultimately lead to an increase in the localized temperature of the targeted area to >2500 °C. Consequently, the chemical bonds such as N – C, C – O and C = O are broken, resulting in removal of nitrogen and oxygen atoms and leaving behind aromatic compounds that can rearrange to form graphitic structures. So, the formation of graphene by the application of laser beam is the cause of the conversion of the sp3 hybridized carbon atoms to sp2 carbon atoms. Lin et al. [2014] Le et al. [2022] By using LIG process, it is possible to achieve a superficial, conductive layer of graphene on the surface of carbon rich substrates within few seconds. Following figure 1.5 shows LIG formation on the surface of a polyimide (PI) substrate.

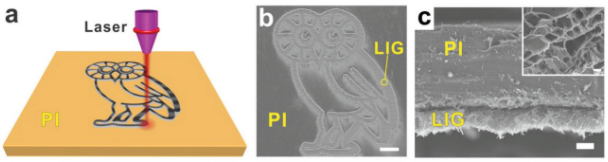

Figure 1.5: LIG formation on PI Ye et al. [2018]

Since the discovery of the LIG process in 2014 by J. Lin and coworkers Lin et al. [2014], LIG has been used for various applications, including manufacturing of biophysical/ biochemical sensors and soft actuators. Moreover, the LIG process was also utilized in the fields of energy storage devices with the implementation of supercapacitors (SCs), devices for sensing sound, photons, temperature, strain, chemical species, and as sensors inside microfluidic devices. Additionally, LIG-based substrates can be also employed for the realization of filters and membranes for water treatment, due to the high porosity of the induced graphene. Misra et al. [2023] The extensive utilization of LIG in above applications is because of its ease of processing according to the desired pattern by simply

applying direct laser writing without the need of wet methods and/or photolithography processes. Ye et al. [2018] Le et al. [2022] LIG patterned materials exhibit high porosity, excellent electrical conductivity, and good mechanical flexibility. The use of raw and common materials as substrates, as well as avoiding the use of chemicals or masks can further reduce the environmental impact. Le et al. [2022]

1.6 Type of process defects

The synthesis of graphene by the LIG process is not free of possible crystallographic defects in the graphene's lattice. The main types of defects that may occur are point and line defects. Point defects, considering a general graphene lattice structure, can be:

- Self-interstitial: when a carbon atom doesn't occupy the correct spot in the lattice structure.
- Interstitial: when an impurity atom doesn't occupy the correct spot in the lattice structure.
- Vacancy: when there's a missing carbon atom that is supposed to fill a correct place in the lattice structure.
- Substitutional impurity: when an impurity atom joins the lattice structure.

The most remarkable point defects in graphene are called Stone-Wales (SW) defects. It may happen that in the crystallographic structure of graphene, which is an ordinate layer of hexagon arranged carbon atoms, a carbon atom from one hexagon may join another adjacent hexagon, leaving at its place one hole. In dependence on the number of vacancies involved, those kinds of defects can be "Single Vacancy (SV)" or "Multiple Vacancies (MV)".

Always talking about point defects, it also may happen that a carbon (or a foreign) atom joins the structure of a hexagon-arranged carbon structure without changing its shape. The extra atom is so called carbon adatom or foreign adatom. Furthermore, adatoms can migrate around the overall graphene lattice even at room temperature. The presence of adatoms, vacancies and SW defects can lead to an increase of the resistance of the graphene, due to the induced scattering mechanism that conduction electrons exhibit. Graphene can also exhibit edge dislocations: they consist in the insertion of an extra half-plane of atoms in the regular lattice. This can distort of course the lattice structure, provoking compression and tension stress. This is called a line defect because the locus of defective points produced in the lattice by the dislocation lies along a line. Therefore, line defects lead to non-hexagonal rings which should enhance the presence of electronic states in the transverse direction and localized all over the line. Hence, that can improve the conductivity along the line because of a larger number of conducting channels. Furthermore, also defects that happens at the boundaries of the graphene's pattern exist. They are called edge defects. Banhart et al. [2011]

1.7 Substrates employable

A feature that makes LIG very versatile is the variety of possible substrates that can be used. Carbon-based materials, such as organic materials can be employed for this purpose, such as coconut, cork, bread and potato. Figure 1.6. Chyan et al. [2018]

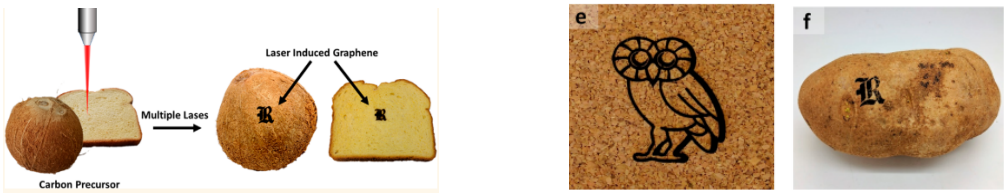

(a) LIG formation on coconut and bread (b) LIG formation on cork and potato

Figure 1.6: Possible organic substrates Chyan et al. [2018]

Also, paper-based materials can be used. Indeed, they are costless, biodegradable and very versatile. Those can be well exploited for Internet of Things (IoT) applications, such as wearable electronics and smart packaging for the agro-industry. Possible drawbacks are their roughness, porosity and insufficient resistance to heat and humidity. Malik et al. [2023] Araki et al. [2023] At this purpose, authors of Malik et al. [2023] implemented a CVD QDs/SLG (Quantum Dots/Single Layer Graphene) PD (PhotoDetector) on a paper substrate. The devices exhibit an external responsivity of 520 A/W under 405 nm illumination at <1 V operating voltage. Figure 1.7.

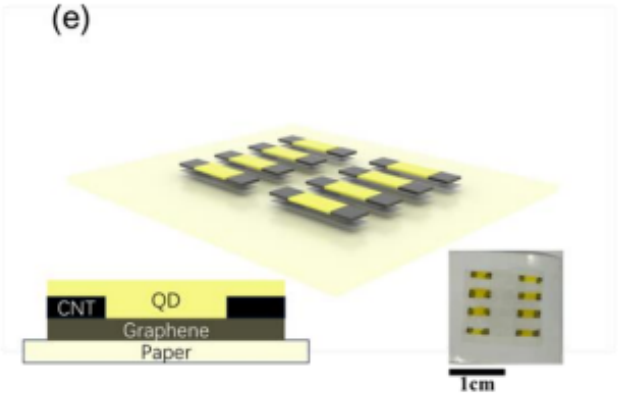

Figure 1.7: QDs/SLG PD on paper Malik et al. [2023]

Other suitable substrate materials are polymers, such as polyimide (PI) Lin et al. [2014] Le et al. [2022] Misra et al. [2023], polyethersulfone (PES) Misra et al. [2023], Kapton. Chyan et al. [2018]
In general, the most suitable materials for performing LIG, according to Lawan et al. [2024], should mainly have:

- High thermal stability: the substrate should be able to withstand the intense heat generated during the laser process. This aspect prevents degradation and aids the formation of quality LIG. Polyimide, which is traditionally used in LIG applications, has excellent thermal stability.
- High char residue: it is the carbonaceous solid residue after the thermal process.
- High toughness: to resist mechanical stresses during the lasing process
- Stacked aromatic hydrocarbon in its structure: materials with that composition exhibit both high thermal stability and char residue

Furthermore, authors of Pinheiro et al. [2022] report that another key aspect for the formation of LIG is the presence of aliphatic carbon rings within the polymeric structure. This is the case of cellulose and that is the reason why paper-based materials are suited for the LIG formation. The authors also mention that aromatic carbon chemical arrangements are more inclined to the graphenization. Their absence in paper-based material is the cause of the reduced conversion process if compared to polyimide or wood.

1.8 Other methods to synthetize graphene

The most remarkable conventional methods that has been used to synthesize graphene are:

- **Mechanical exfoliation**: this technique consists of reducing graphite into graphene layers by mechanical forces. For this scope, adhesive materials can be exploited (sticky tapes or specific polymers such as PMMA/PDMS). Graphene sheets can so be obtained by a combination of shearing and normal mode exfoliation. Robert et al. [2019]
- **CVD (Chemical Vapor Deposition)**: with the CVD process and its variants it is possible to grow layers of graphene on a substrate by chemical reactions with carbon-based gaseous precursors. Most used precursors are gases: methane (CH_4) and acetylene (C_2H_2). Copper has been chosen as the best substrate for growing graphene layers. The precursor and other helping gases (Ar, inert and H_2 to help the graphene growth) can flow through the reaction site: a low pressure quartz tube. Then, after the chemical reactions and the deposition of carbon on the substrate, the reaction products can exit the chamber through a gas ejection module composed by a vacuum pump and the gas outlet. The growth graphene layer can so be detached from its substrate performing wet or dry etching processes. Hernández et al. [2022]
- **Modified Hummer's Method:** the latter is a process that allows the formation of graphene by firstly oxidizing graphite flakes to form Graphene Oxide (GO). To obtain GO, strong oxidizing species are usually used, such as sulfuric acid (H_2SO_4) and potassium permanganate ($KMnO_4$). After GO is obtained, a reduction step can be performed to obtain graphene. This can be done by using reducing species (hydrazine, N_2H_4 or sodium borohydride, $NaBH_4$) or by a thermal process. Zhang [2022]

1.9 Designs on substrates and final applications of LIG-based devices

Among the previously mentioned application fields for the LIG, biochemical wearable sensors for medical applications must be highlighted. Graphene, due to its extraordinary electrical and optical properties, has been used in the past years for the detection of ionic species, micro RNA, DNA, folic acid detection and the monitoring of glucose. The LIG technique can be employed to fill the existing gap between laboratory research and commercialization of the device, due to the incredibly immediate implementation of the highly conductive graphene's patterns. Liu et al. [2022] Le et al. [2022] In the paper Le et al. [2022] the authors refer to the implementation of a LIG biofield effect transistor (bio-FET) that can be used to detect the presence of a targeted biomaterial, the spike protein (s-protein) for the SARS-CoV-2 diagnosis. The referred device is the one depicted in figure 1.8.

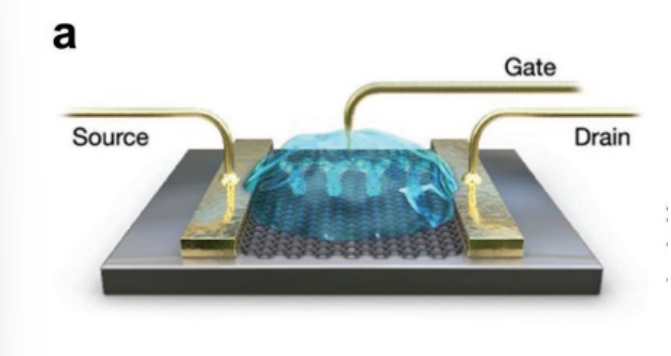

Figure 1.8: LIG bio-FET Le et al. [2022]

The channel of the transistor is the LIG implemented conductive layer, which joins in the metal source and drain terminals of the device. The LIG channel is immersed in an electrolyte solution, such as phosphate-buffered saline (PBS) or ionic liquid. Once the bias window of the device has been set, by applying a proper V_{DS} voltage, the i_{DS} current of the device changes in dependence on the attachment or not of the s-protein on the graphene's substrate. Indeed, thanks to the chemical binding between the target species and the graphene, an electric field close to the channel can be induced. The result is a variation of the transfer current of the device. Another application of the LIG is the implementation of pressure sensors, as still described by the authors in the paper Le et al. [2022]. They report that LIG exhibits a remarkable piezoresistive effect, with higher sensitivity to mechanical stimuli with respect to monolayer graphene. So, according to the mechanical stress in input at the sensor, the LIG sensing device can stretch/compress and this is associated to its resistance variation. Those kinds of flexible pressure sensors can be employed in biomedical applications for monitoring intraocular pressure, tactile perception, heart rate and voice. One of the possible implementations is to enclose polystyrene (PS) microspheres between two LIG polyurethane (PU) layers.

Natural cork can be exploited for this purpose too: LIG rectangular layers have been created on the surface layer of the cork. The two short edges of the LIG pattern, which face with unprocessed cork, are connected to a measurement device to track resistance variations. Figure 1.9a. A $MoS_2 - LIG$ based strain sensor for detecting eye blinking can be observed in figure 1.9b.

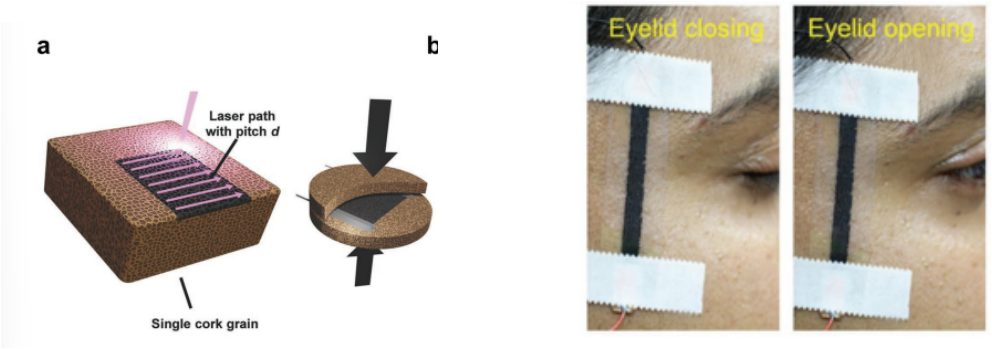

(a) Cork based piezoresistive sensor (b) Mo_2-LIG based piezoresistive sensor

Figure 1.9: Piezoresistive sensors Le et al. [2022]

LIG has also emerged as a very promising material for the design of supercapacitors. Indeed, LIG supercapacitors exhibit a very high capacitance and excellent mechanical flexibility with a low-cost fabrication process. In the paper Lin et al. [2014] the authors implemented a supercapacitor composed by LIG electrodes on a polyimide substrate. Figure 1.10.

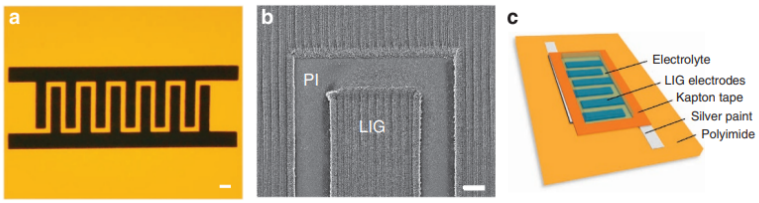

Figure 1.10: LIG based supercapacitor Lin et al. [2014]

That device is built by forming an array of LIG combs interfaced with an electrolyte. Silver paint has been applied on the common positive and negative electrode to improve conductibility and Kapton tape has been used to define the active electrodes. A capacitance value of $C_A > 4\,mF\,cm^{-2}$ has been found, with a scan rate of $20\,mV\,s^{-1}$; this value is comparable with or higher than the value of recently reported GO based supercapacitors. Commercial devices of this kind can be aluminum electrolytic capacitors, thin film Li-ion batteries, and activated-carbon supercapacitors. The so implemented LIG based supercapacitors can offer more energy, power density of both compared to the traditional implementations.

An application of the LIG in the realization of smart packages can be appreciated in figure 1.11.

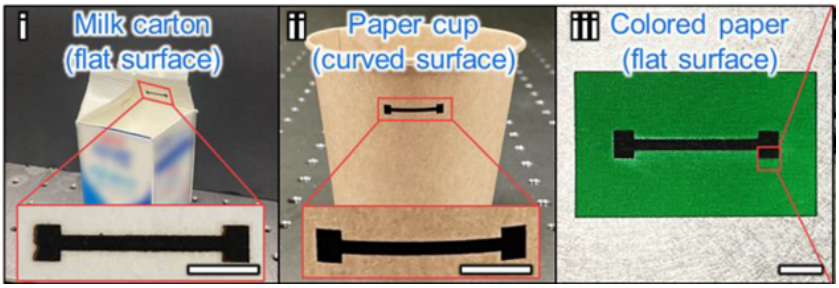

Figure 1.11: i) LIG sample on commercial milk carton ii LIG sample on paper cup iii) LIG sample on a colored paper. Scale bar: 5 mm Jung et al. [2022]

The authors of Jung et al. [2022] realized a sensor for monitoring the food spoiling process. Indeed, the LIG exhibits a temperature dependent profile of the resistance. Indeed, the authors report a progressive decrease of the resistance of the sample when the substrate increases its temperature. Moreover, the resistance of the sample increases with a decrease of the temperature of the substrate. Hence, the authors report an application of this technology to monitor the chemical status of raw pork meat and milk. The LIG sample was placed inside the sealed package of the pork. Furthermore, the LIG sensor was integrated in a wireless sensor module to send information in real time to the user's mobile phone. Indeed, during the spoiling process, the pork meat generates TMA gas over time. When the pork meat was exposed to a warm environment (37 °C), the TMA gas started to be produced. The rapid increase of the resistance of the LIG in the warm environment was the indicator of the spoiling process begin. Indeed, authors report that when the TMA molecules that bond with LIG act as electron donors, the resistance of the LIG increases. This is because of the mechanism of recombination with the holes in the graphene. The best achieved resistance variation with TMA was the 0.1% considering the optimal energy density for the LIG process.

Another example of LIG based devices on packaging materials is the work of the authors of Kulyk et al. [2021]. They implemented a strain sensor on cellulosic materials, specifically paper. Figure 1.12.

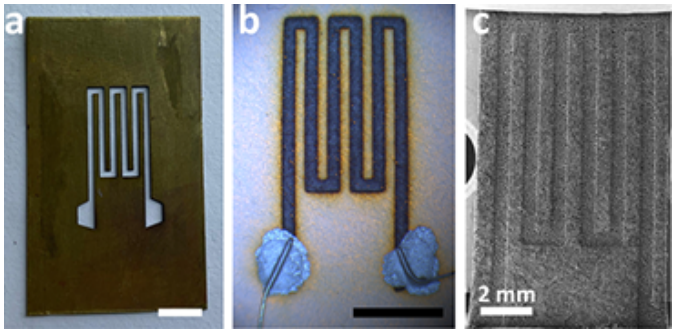

Figure 1.12: LIG strain sensor and behavior: a) LIG sensor on paper b) LIG sensor with the deposition of the contacts c) SE-SEM image of the LIG sensor Kulyk et al. [2021]

According to the bending of the sensor, its resistance exhibits a variation. Figure 1.13.

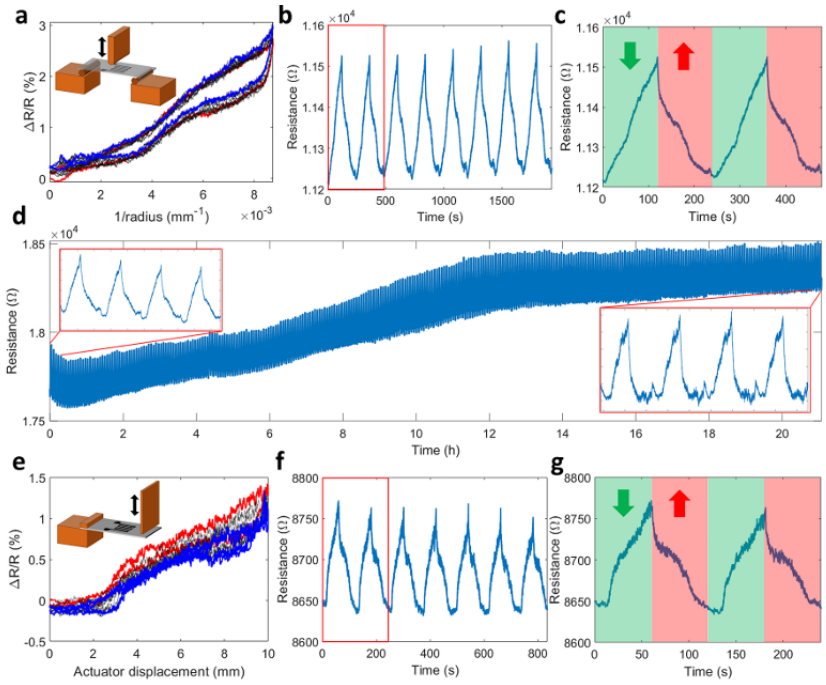

Figure 1.13: Experiments for evaluating the variation of resistance versus strain and time a) Relative variation of the resistance with respect to the inverse of the bending radius in the considered setup b) Resistance variation versus the time of cyclic bending in the considered setup c) Resistance variation considering two cycles in the considered setup d) Behavior of the resistance of the sensor over long time in the three point bending setup e) Relative variation of the resistance with respect to the inverse of the bending radius in the considered setup f) Resistance variation versus the time of cyclic bending in the considered setup g) Resistance variation considering two cycles in the considered setup Kulyk et al. [2021]

In light of their study, the authors suggest the future implementation of this technology in paper LIG electronic devices, suitable for low-cost and eco-friendly applications.

1.10 Aim of the thesis

This research activity aims to optimize the LIG process parameters for biodegradable substrates to achieve conductive patterns without requiring additional processes or materials. This technology can be the basis for the future development of Laser Induced Graphene (LIG) based smart packages. Furthermore, this research work has been conducted in the context of the project Proof Of Concept "PIrolisi selettiva e controllata di materiali polimerici per l'etichettatura intelligente (Smart TAg) di packaging in ambito Agrifood" (PISTA), funded by the European Union - Next Generation EU, Component 1 of Mission 4. Hence, after the optimization process for the lasing parameters to achieve conductive patterns on polymeric materials and paper-based materials, this work relies on the DC characterization of the obtained samples on smart packaging suitable paper-based materials. Finally, the optimized samples are characterized in AC by the application of a voltage signal which frequency sweeps from 20 Hz to 2 MHz to state the future feasibility for the implementation of on-package antennas.

Chapter 2

Laser processes on carbon-based substrates

The goal of the experiments performed in this chapter is to optimize the lasing parameters for the LIG process, to create conductive patterns. Since the involved substrates are all carbon-based materials, the resulting traces are carbonaceous compounds. To state the effective graphene formation, a Raman or SEM analysis should be conducted. The materials under test in the first section of this chapter are Kapton, PET and LDPE. The first is one of the most widely used materials in literature to perform LIG. The other two substrates are frequently used materials for the packaging of foods and beverages. The second section is about paper-based substrates that can be employed as packaging materials for the agro-industry. Many kinds of cardboard and the material of paper-based plates have been investigated for the future implementation of LIG-based smart-packages. The implementation of smart-packages with those materials, indeed, can lead to cost reduction, environmental sustainability and a very flexible design of the implementable functionality due to the direct laser writing without the need of additional processes; apart from the application of spray retardants that prevent the substrate from ablation and burnings. Kulyk et al. [2021] Malik et al. [2023]

Various experiments have been performed using the stand-alone laser marker "Laser Slider" from Microla Optoelectronics S.r.l.. Figure 2.1. The active medium of the laser is CO_2, whose peak emission wavelength is $10.6\,\mu m$. According to the literature Sartanavičius et al. [2023], Sartanavičius et al. [2023], photons with this wavelength can induce a photothermal effect on the substrate, causing lattice vibrations. These can increase the thermal energy in the treated zone with a subsequent break of the carbon's chemical bonds and hence the formation of the graphene structure.

Figure 2.1: Laser Slider machine from the Microla Optoelectronics S.r.l. website: https://www.micro-la.com/open/design-detail/7/marcatura-laser-standalone-laser-slider

The software used is the *Lighter 6.1.0*. The main window of the software for the shape design and the choice of the lasing parameters is shown in figure 2.2.

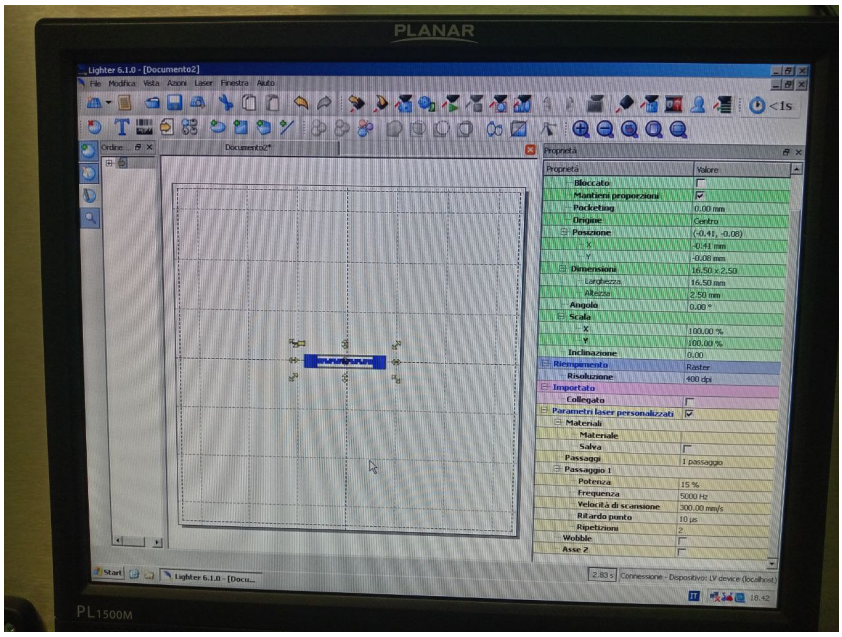

Figure 2.2: Design parameters

2.1 Initial experiments: LIG implementation of various patterns on Kapton, PET, front and back side of an LDPE bag

The goal of the following experiments is to acquire the methodology and awareness of the possible issues in the realization of LIG to further treat paper-based materials.

2.1.1 Processing parameters

To prepare LIG on carbon-based substrates, various parameters must be carefully selected depending upon the type of material.

The following lasing parameters are used to control the LIG formation in the substrate materials: Chyan et al. [2018]

- **Input power**, usually expressed in percentage of the nominal maximum power of the laser machine; e.g. 5% W
- **Scan rate**: the scan velocity of the laser through the pattern that has to be written on the substrate; e.g. 15 mm/s
- **Defocus**: the distance between the focal plane of the laser and the target substrate; e.g. 1 mm. This parameter can be set to change the spot size of the laser
- **Spot size**: the diameter of the laser beam on the material. E.g. from 175 μm at the focal plane, to 300 μm with 1 mm of defocus
- **Density of the spots**: the number of spot sizes per inch (1 in = 2,54 cm), measured in DPI (Dots Per Inch); e.g. 1000 DPI
- **Number of exposures**: how many times the laser beam passes through the whole pattern; e.g. 5
- **Frequency**: the frequency at which the laser beam hits the surfacce; e.g. 5 kHz

Increasing the lasing power, the photothermal effect with the subsequent arrangement in graphene of the carbon atoms in the lattice is enhanced. Considering this, by increasing the lasing power, an increase in the conductivity of the pattern is expected. A drawback is the higher risk of burning the substrate. The same effect is achieved with an increase in spot size, DPI, and number of exposures. Increasing the spot size of the laser beam by increasing the defocus leads to the higher overlap between adjacent beams. By increasing the DPI, the density of the lased area increases, leading to an increase of the lased zones throughout the designed geometry and furthermore to a higher overlap between adjacent beams and provoking a deeper carbonization of the substrate. By increasing the number of repetitions, the laser machine executes multiple scans of the same design area. This can, of course, further improve the conduction of the carbonaceous pattern. The same effect can also be obtained by lowering the scan speed and the frequency. Indeed, with

lower scan speeds and frequencies the energy dose increases. This is because the laser beam hits the target area for more time, locally increasing the photothermal effect.

For achieving good results in the synthetization of graphene with the LIG process, the previously mentioned parameters of the laser must be chosen carefully. A risk during the lasing process is burning the substrate, due to the too high induced overheat. This can obviously compromise the substrate integrity. Another aspect to pay attention to is to carefully adjust the energy dose provided by the laser to avoid unwanted holes and cuts.

2.1.2 Kapton

The Kapton (poly (4,4'-oxydiphenylene-pyromellitimide)), as its name suggests, is a type of polyimide (PI). Various processes have been conducted by varying the scan velocity of the laser and keeping the other parameters constant.

Experiments have been conducted considering different geometries to state which is the best suited for the formation of the conductive pattern.

Straight pattern

The implemented geometry is depicted in figure 2.3. A similar geometry has been implemented by the authors of the previously cited Jung et al. [2022] on paper-based materials. Figure 1.11.

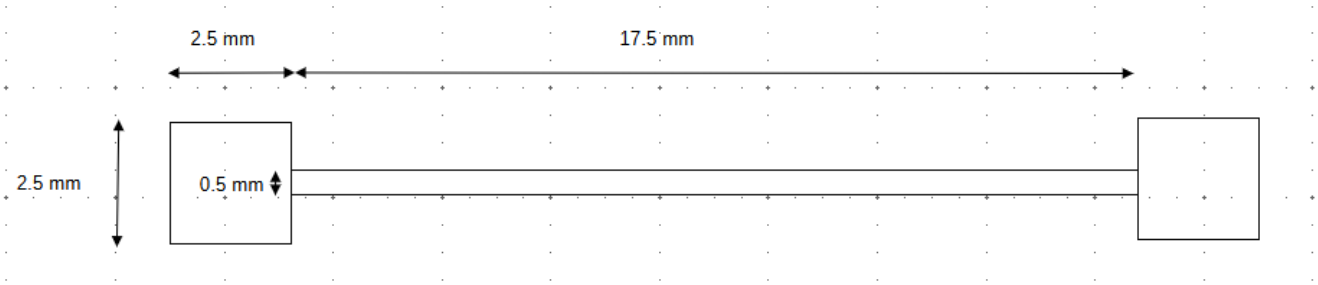

Figure 2.3: Straight geometry on Kapton

The total area of the pattern is 21.25 mm^2. An overview of the experiments can be seen in table 2.1.

Experiment number	Power (% of 30 W)	DPI	Frequency, kHz	Repetitions	Scan velocity, mm s-1
1	15%	400	5	2	350
2	15%	400	5	2	300
3	15%	400	5	2	250

Table 2.1: Experiments for obtaining LIG on Kapton

The first and second experiments lead to the best results in terms of the homogeneity of the grown carbon-based layer, figure 2.4.

Figure 2.4: Best results: leftmost triplet: scan velocity = 350 mm s^{-1}, rightmost triplet: scan velocity = 300 mm s^{-1}

Even if the second attempt is characterized by a scan speed lower than that of the first one, no burning occurred. The third attempt resulted in slightly lower homogeneity, figure 2.5.

Figure 2.5: Third attempt: slightly lower homogenity. Scan velocity = 250 mm s^{-1}

A further implicit parameter is the flatness of the Kapton sheet. Hilly surfaces often cause burning and disrupt the carbonaceous layer, as shown in figure 2.6.

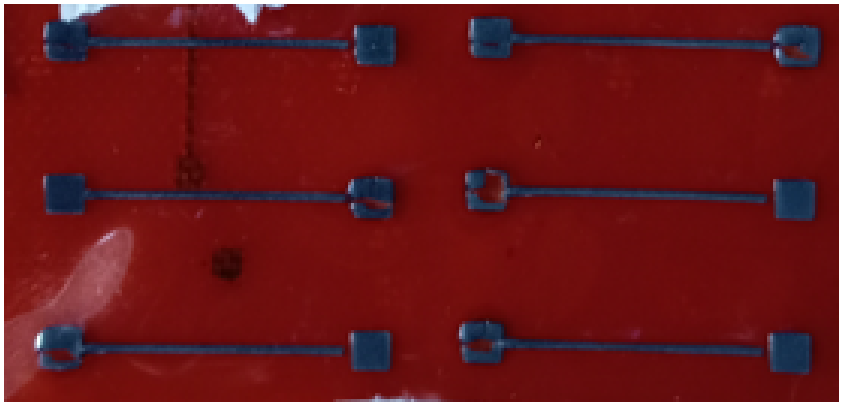

Figure 2.6: Broken patterns, due to the hilly substrate. Leftmost: scan velocity = 350 mm s^{-1}, rightmost: scan velocity = 300 mm s^{-1}

At even lower scan speeds, higher power per unit time damages the pad zones, figure 2.7.

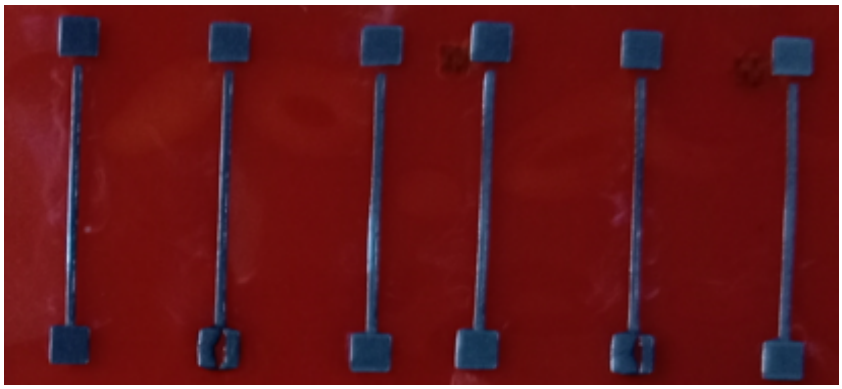

Figure 2.7: Patterns obtained with 200 mm s^{-1} scan speed

Square wave shaped pattern

Another implemented geometry is the square wave design, figure 2.8. As anticipated, the aim of the design and implementation of different geometries is to state which is the most suited to obtain conductive patterns while keeping the substrate not damaged. The area of the geometry is kept constant with respect to the straight geometry; A = 21.25 mm^2.

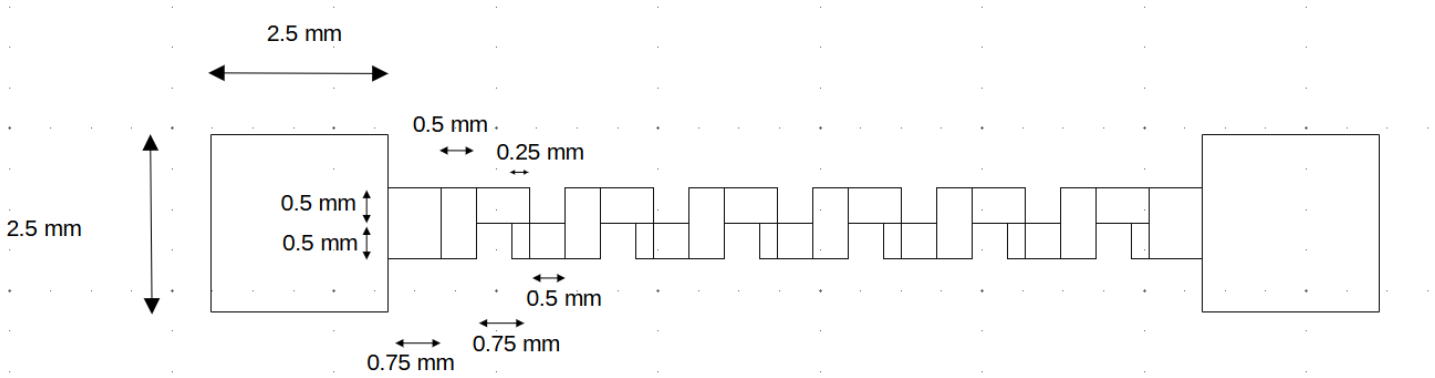

Figure 2.8: Square wave design pattern

The experiment was conducted using the found best parameters:

- **Power (% of 30 W)**: 15%
- **DPI**: 400
- **Frequency, kHz**: 5
- **Repetitions**: 2
- **Scan velocity, mm s^{-1}:** 300

The resulting pattern was well formed and homogeneous, with no burnings or holes. On the other hand, this geometry induced hilliness on the substrate's surface due to the heat generation in nearby areas interspersed with untreated zones. Figure 2.9.

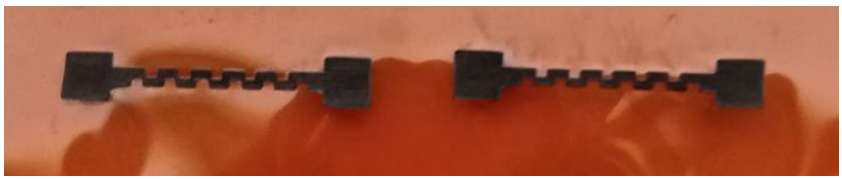

Figure 2.9: Square wave patterns

Zigzag shaped patterns

Two additional geometries were designed as zigzag patterns, shown in figures 2.10 and 2.11. The area is kept constant with respect the one of the previous geometries; A = 21.25 mm^2.

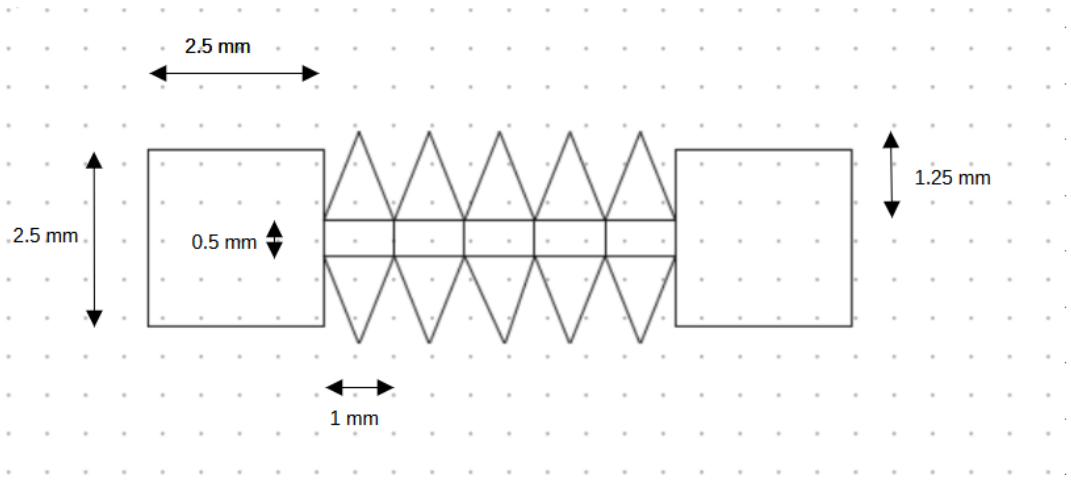

Figure 2.10: First design of the zigzag shaped pattern

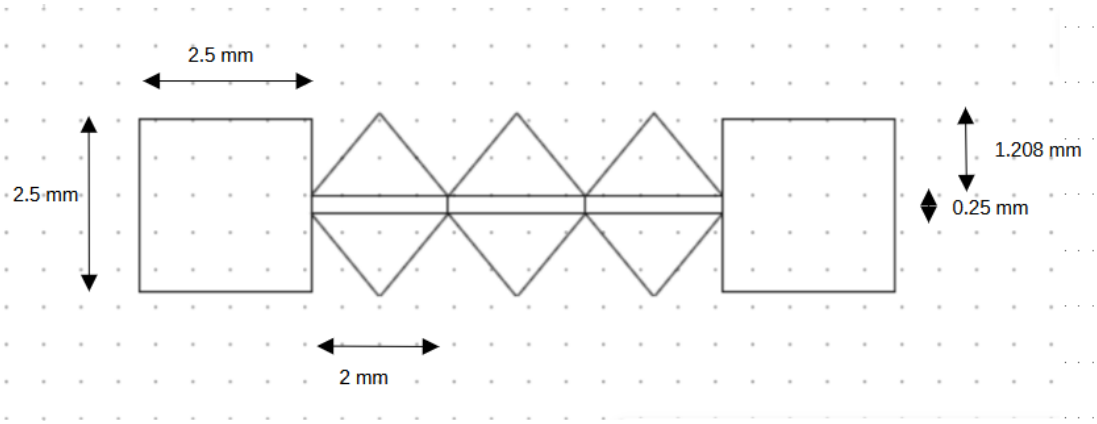

Figure 2.11: Second design of the zigzag shaped pattern

The used laser parameters are the same with respect to the ones used for the square wave pattern. The resulting samples are shown in figure 2.12.

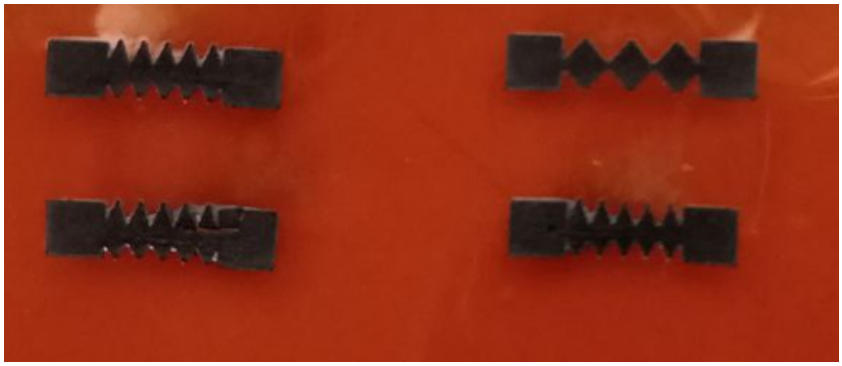

Figure 2.12: Zigzag shaped patterns

All samples show the formation of the carbonaceous without either burnings, holes or cracks. However, the bottom-left sample displays cracks due to substrate unevenness. Furthermore, all the geometries led to a substrate's hilliness. The hilliness of the substrate is more evident considering the zigzag geometry in figure 2.10 due to the heat generation in nearby areas interspersed with untreated zones. Indeed, considering that shape, the triangle-shaped patterns are denser, leading to a higher heat generation which caused the surface to deform.

2.1.3 PET

The second treated material is PET (polyethylene terephthalate). The implemented geometry for patterning the PET and the following polymeric materials is the straight one, figure 2.3. The conducted experiments are summarized in table 2.2.

The first set of parameters is the one that led to the best result for Kapton. The experiments from 1 to 3 only led to a very slight patterning of the substrate, without the formation of a carbonaceous layer. To achieve that, the 4^{th} experiment has been conducted by lowering the scan speed to 50 mm/s and keeping all the other parameters the same as in experiment 2. The sample patterned with this set of parameters exhibits burning regions and holes. In light of this, experiment 5 has been conducted by keeping all the parameters the same as for experiment 4 except for the frequency which has been increased to 10 kHz. The aim is to tune the lasing parameters to provide enough energy dose without holes in the substrate.

Experiment number	Power (% of 30 W)	DPI	Frequency, kHz	Repetitions	Scan velocity, mm s-1
1	15%	400	5	2	300
2	5%	400	5	2	300
3	10%	400	5	2	150
4	5%	400	5	2	50
5	5%	400	10	2	50

Table 2.2: Experiments for obtaining LIG on PET

The results are depicted in figure 2.13.

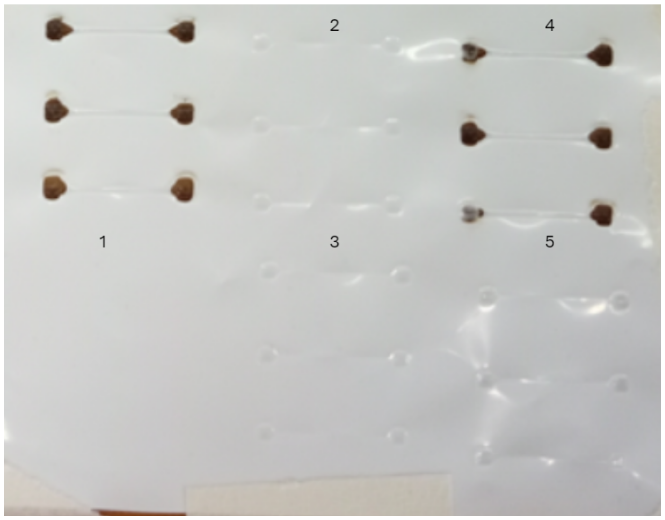

Figure 2.13: Experiments for obtaining LIG on PET

None of the experiments led to the formation of a conductive carbonaceous pattern. PET either burned in the pad zones considering the experiments 1 and 4 or did not exhibit remarkable patterning: experiments 2, 3 and 5.

2.1.4 Back side of a LDPE based bag

LDPE (low-density polyethylene) is a thermoplastic polymer. Experiments on uncoated LDPE were conducted using the parameters in table 2.3. The following parameters have been chosen considering the experiments on PET as the starting point. Indeed, experiments 1 and 2 consider the same parameters as the experiments 4^{th} and 5^{th} respectively for PET.

Experiment number	Power (% of 30 W)	DPI	Frequency, kHz	Repetitions	Scan velocity, mm s-1
1	5%	400	5	2	50
2	5%	400	10	2	50

Table 2.3: Experiments for obtaining LIG on uncoated LDPE

The showed results in figure 2.14 led to a damage of the substrate, without the formation of a carbonaceous conductive pattern.

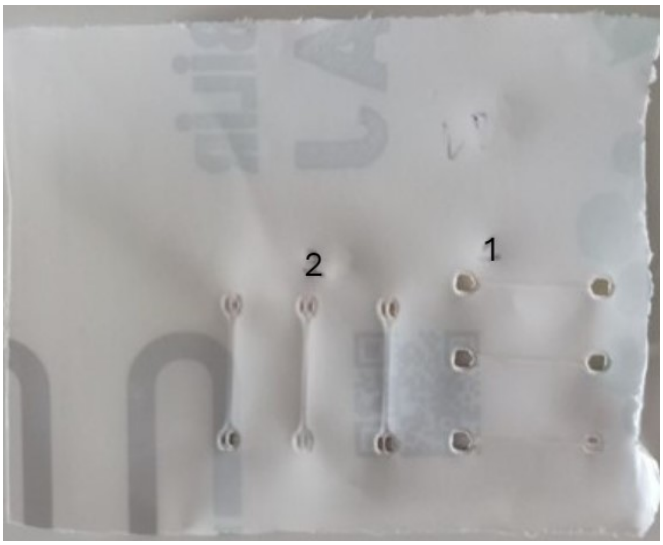

Figure 2.14: Experiments for obtaining LIG on uncoated LDPE

2.1.5 Front side of a LDPE bag

The front side of a LDPE-based bag was used to improve LIG growth, figure 2.15. The previously shown set of parameters is considered also in this case. The results of the experiments can be appreciated in figure 2.15. As it can be seen, the LIG process cannot be implemented on this kind of substrate. Indeed, both unformed patterns: experiment 1 and holes: experiments 2 and 3 are registered on the substrate.

Figure 2.15: Experiments for obtaining LIG on coated LDPE

2.1.6 Conclusions

In the light of the conducted experiments on PET, front and back side of a LDPE bag and differently for Kapton which resulted to be a reliable substrate to obtain LIG, it is not possible to obtain conductive patterns regardless on the combination of the lasing parameters. Indeed, all the plastic materials either burned, creating holes, or the chosen parameters generated insufficient heat resulting only in the deformation and slight melting of the substrate in the patterned zones. Authors of Huang et al. [2018] successfully synthesized LIG on a organic polybenzimidazole (PBI) ink coated PET. The authors used a 355 nm UV laser to induce both photochemical and photothermal effects. The PBI ink is essential because it acts as the precursor for the formation of LIG on PET by a direct writing process. Furthermore, in light of what was explained at the end of section 1.7, one of the key characteristics that the substrates must have to perform LIG is the presence of stacked aromatic hydrocarbon in their structure. Indeed, materials with that composition exhibit both high thermal stability and char residue leading to the formation of laser-induced graphene Lawan et al. [2024]. Furthermore, only the straight patterned samples on Kapton are those which exhibit the highest homogeneity without compromising the substrate integrity and flatness.

2.2 LIG process on paper-based substrates

In this section, experiments were conducted to obtain LIG on cardboard, corrugated cardboard and thick cardboard while considering different parameters. Those indeed, are typical materials for agro-industry packaging. As anticipated in 1.10, the goal with the further experiments on these kinds of substrates is to achieve conductive patterns

for the future development of LIG-based smart packages. At this purpose, the aim of this chapter is to find a reliable set of lasing parameters to achieve the most uniform conductive pattern on these kinds of substrate. It is important to highlight that paper-based materials are highly flammable and this leads to a significant risk of burning and flames during the lasing process. To avoid that, all the paper-based materials have been previously coated with a commercial flame retardant spray: "BBT Antiflame". The spray coating was performed manually with the aim to cover in the most uniform way possible the substrate under study. After having deposited the product on the whole surface, the process is repeated to achieve the required number of coatings. After one hour drying process at room temperature, the substrate is ready to be treated.

2.2.1 Geometry design

As in the case of polymeric materials, different geometries have been considered. This is done to understand which can led to the formation of a conductive pattern, without burnings or more in general without damaging the substrate and hence to be considered for performing further analyses.

Straight shape

The standard geometry for paper-based substrates is different with respect to the one used to pattern polymers: figure 2.16.

Figure 2.16: Standard geometry for paper-based substrates

The size of the two square pads at the edges has been kept constant with respect to the previous design. The channel, instead, has been increased in width and reduced in length. This due to the considerations made in the previous chapter about the lack of aromatic carbon chemical arrangements in paper-based materials: 1.7. The total area is 42.5 mm^2. As in the case of Kapton, other types of geometry have been designed. To make all of them comparable in terms of performance, the same area is kept constant between all the designs.

Square wave shape v1

The following square wave shape has been designed, with the following measures: figure 2.17.

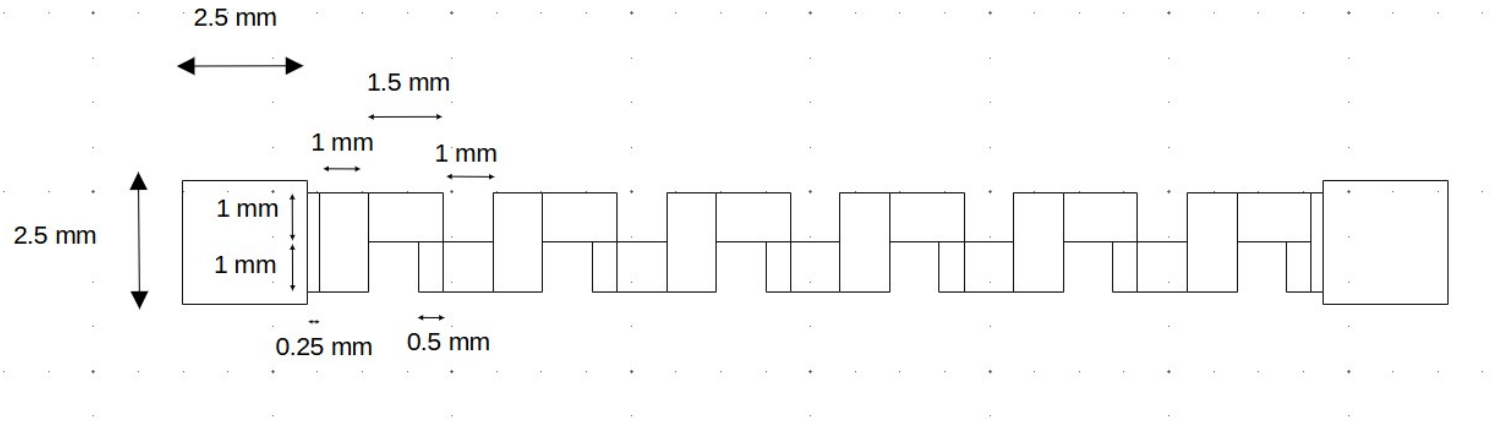

Figure 2.17: Square wave geometry paper-based substrates, v1

Square wave shape v2

The following is another implementation of the square wave geometry, considering the following measures: figure 2.18.

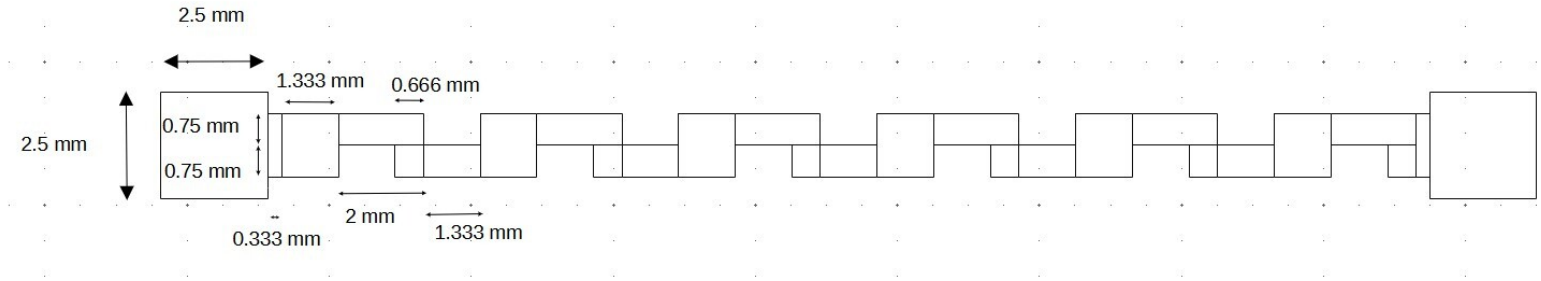

Figure 2.18: Square wave geometry on paper-based substrates, v2

Zigzag shape

Another geometry that has been implemented relies on a zigzag shape. The designed geometry is depicted in figure 2.19.

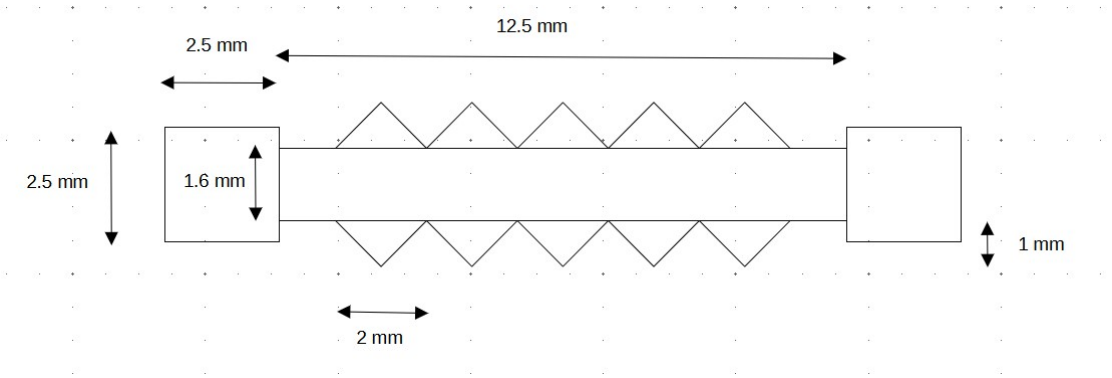

Figure 2.19: Zigzag geometry on paper-based substrates

2.2.2 Experiments

Cardboard

The previously shown geometries have been implemented on two times flame retardant spray coated cardboard. The choice about the number of coatings by the flame retardant spray was made to trade off the improvement of the carbonization process with the risk of burnings on the substrate. Indeed, previous experiments considering only one flame retardant spray coating led to burnings around the patterned geometry.

The following experiments have been considered: the parameters for performing experiment 1 have been chosen to balance the provided energy dose. The second set of parameters have been chosen to reduce the energy dose by lowering the number of repetitions of the laser beam to 2. The last set of parameters have been selected to verify if with a slightly higher energy dose the substrate burns: for this purpose the number of repetitions of the laser beam has been increased to 3.

Experiment number	Power (% of 30 W)	DPI	Frequency, kHz	Repetitions	Scan velocity, mm s^{-1}
1	5%	400	5	5	30
2	5%	400	5	2	30
3	5%	400	5	3	30

Table 2.4: Experiments for obtaining conductive patterns on cardboard, coated twice with flame retardant spray

The results of the experiments are shown in the following figure 2.20.

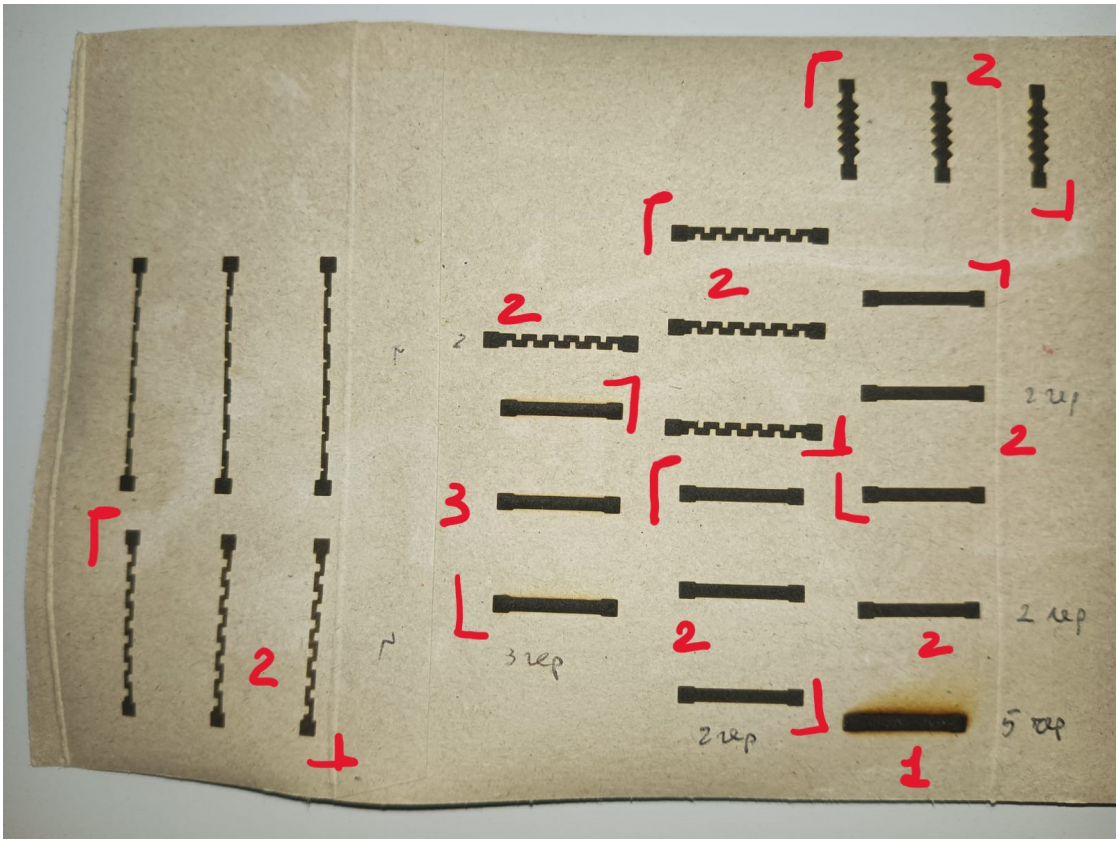

Figure 2.20: Carbonaceous samples on cardboard, coated twice with flame retardant spray

The first experiment in the figure above led to several burning regions on the substrate. This was due to the excessively high number of repetition scans of the laser beam: 5. For this purpose, the second set of parameters was designed considering a lower number of repetitions: 2. This is the best result achieved. All the samples, even with different geometries, registered no burning zones around the resulting conductive layer. Hence, by setting as 2 the number of repetitions, enough energy dose can be provided to the substrate to enhance the pyrolysis reaction. At the same time, this energy dose is not enough to create burning regions on the substrate that can be created due to the overheating. The further experiment has been conducted to verify whether considering a slightly higher number of repetitions: 3, it can lead to an even more homogeneous carbonaceous pattern without burning regions. The resulted samples show a quite homogeneous carbonaceous layer with minimal burning all over the edges. In view of the obtained results, the best set of parameters for obtaining carbonaceous patterns on two times coated cardboard is the 2^{nd} set of parameters in table 2.4.

Corrugated cardboard

The following experiments have been performed, to achieve a conductive pattern on three times flame retardant spray coated corrugated cardboard. The first set of parameters is the same as the experiment 1 in table 2.4. The following two experiments have been performed with a lower energy dose to avoid burnings on the substrate: the power has been kept constant and the number of repetitions was progressively lowered. Since the substrate continued to be damaged by the overheating, the last two experiments have been performed by lowering the laser power to 1%. The 4^{th} experiment was performed considering as 2 the number of repetitions. In the last experiment the number of repetitions was slightly increased to 3 to state if the previous one was the maximum possible energy dose to both create a carbonaceous pattern and to avoid the burning of the substrate.

Table 2.5

Experiment number	Power (% of 30 W)	DPI	Frequency, kHz	Repetitions	Scan velocity, mm s^{-1}
1	5%	400	5	5	30
2	5%	400	5	3	30
3	5%	400	5	2	30
4	1%	400	5	2	30
5	1%	400	5	3	30

Table 2.5: Experiments for obtaining LIG on corrugated cardboard, three times coated with flame retardant spray

The results of the experiments are shown in the following figure 2.21.

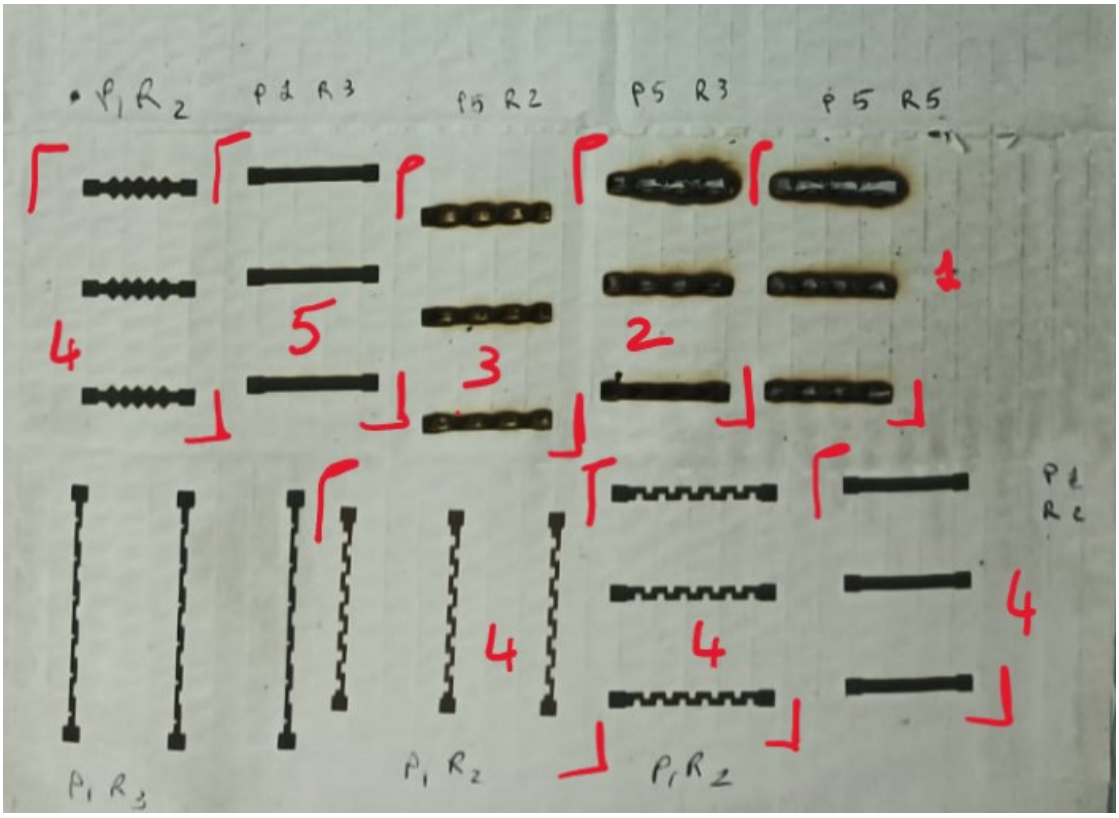

Figure 2.21: Carbonaceous samples on corrugated cardboard, coated three times with flame retardant spray

In view of the implemented samples shown in the figure above, experiments 1,2 and 3 led to a burning of the substrate which severally damaged the formed layer. Hence, further experiments have been performed by lowering the laser power from 1.5 W (5 %) to 0.3 W (1 %) and by varying the number of repetitions. Experiment 4 is the one that led the most homogeneous pattern with all the designed geometries. By slightly increasing the number of repetitions to 3, minimal burning regions around the patterns have been registered: experiment 5.

Thick cardboard

Another substrate that was considered is a type of thick cardboard, covered with the flame retardant spray in the same way as the other substrates: see 2.2. To see the effect of the latter on the resulting conductive pattern, two different experiments have been performed. The two sides of each cardboard piece have been coated with different amounts of spray: one of the two sides has been covered with three times the flame retardant spray and the other side has been treated using seven times the same product. In the following table 2.6 is reported the performed experiment. The parameters have been selected considering experiment 5 in table 2.5 as reference. The scan velocity has been decreased to 15 mm/s

and the number of repetitions has been increased to 7. The choice of the two selected coating layers is related to the greater thickness of this substrate. Indeed, during the absorption process of the product, the flame retardant spray would distribute throughout a larger thickness of the material, making it less concentrated in the lasing area.

Experiment number	Power (% of 30 W)	DPI	Frequency, kHz	Repetitions	Scan velocity, mm s^{-1}
1	1%	400	5	7	15

Table 2.6: Experiment for obtaining LIG on thick cardboard, three and seven times coated with flame retardant spray

The results of the experiments are depicted in the following figure 2.22.

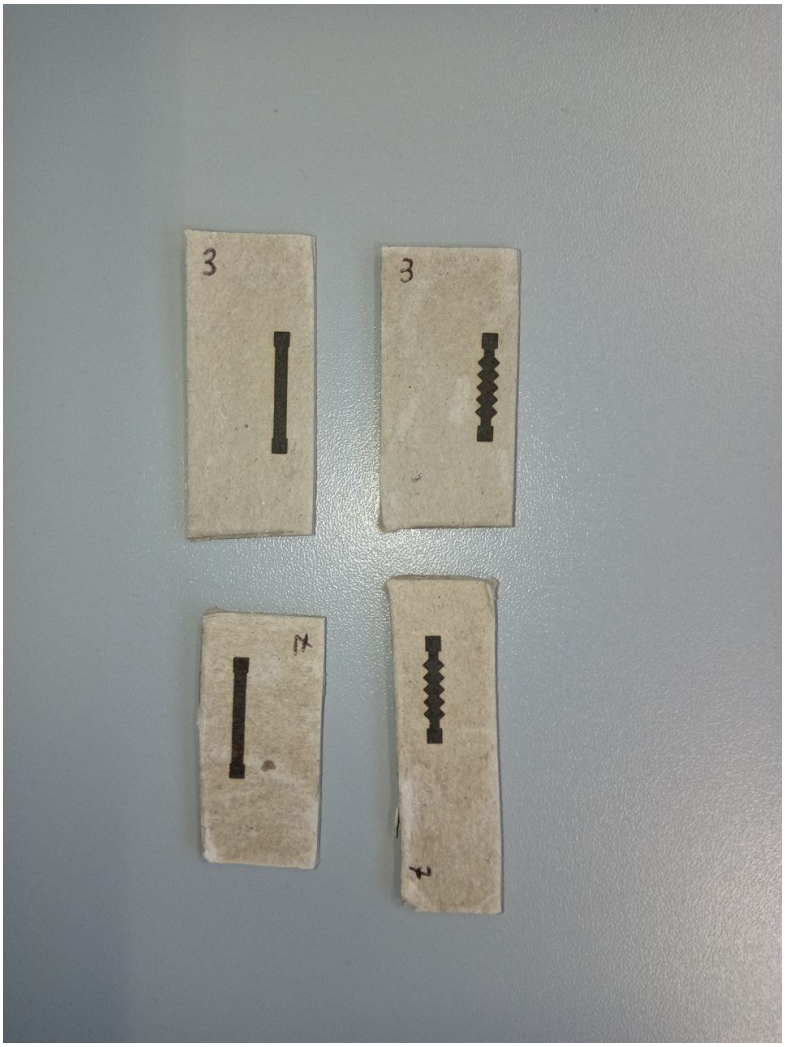

Figure 2.22: Straight and zigzag carbonaceous patterns performed on thick cardboard. Up couple: performed on three times flame retardant spray coated substrate; down couple: performed on seven times flame retardant spray coated substrate

All the samples exhibit burning free carbonaceous layer.

2.2.3 Conclusions

By finding the correct set of parameters, a carbonaceous layer can be formed on the surface of all the considered paper-based materials without the formation of burnings and holes. To state the effectiveness of the process in terms of the conductivity of the created patters, an evaluation of the DC resistance of the samples must be carried out.

Chapter 3

Electrical characterization

In this chapter, the measurement setup and the results in terms of DC resistance of the obtained samples on paper-based materials are going to be analyzed. The lasing parameters that have been chosen are the ones optimized for each sample and they are exactly the ones described in the previous chapter 2.2.

3.1 Measurement setup

To perform the DC resistance measurement, the pads of each pattern have been covered by a first layer of silver paste. This is performed to obtain a better adhesion of the copper wires needed for connecting the sample with the instrument. The deposition of the liquid silver paste avoids the formation of air gaps between the wire and the carbonaceous pad. The presence of air gaps compromises the quality of the measurement. After the silver deposition, the copper wires are placed on the pads and they are then covered with further silver paste to improve the adhesion and the robustness of the connection. Some of the used copper wires had a dielectric coating which protected them from oxidation. For those kinds of wire is necessary to first remove that coating from both the extremities and to cover the latter with a tin-based compound. To do that, a solder machine has been used. The probe of the latter can be heated up to 400 °C. Hence, a tin-based compound can be easily melted when it touches the tip of the probe. Therefore, the edges of the copper wires were covered by the liquid tin-based compound. The high temperature provided by the solder machine was responsible both to remove the dielectric coating on the copper and to deposit the tin-based compound on the naked copper wire. After a 24h drying process at room temperature, it was possible to measure the DC resistance of each sample by connecting the two probes to the two copper wires and choosing the resistance measurement option on the instrument. The multimeter that has been used is the *KEYSIGHT 34401A*. The instrument and the measurement setup can be appreciated in the figure 3.1.

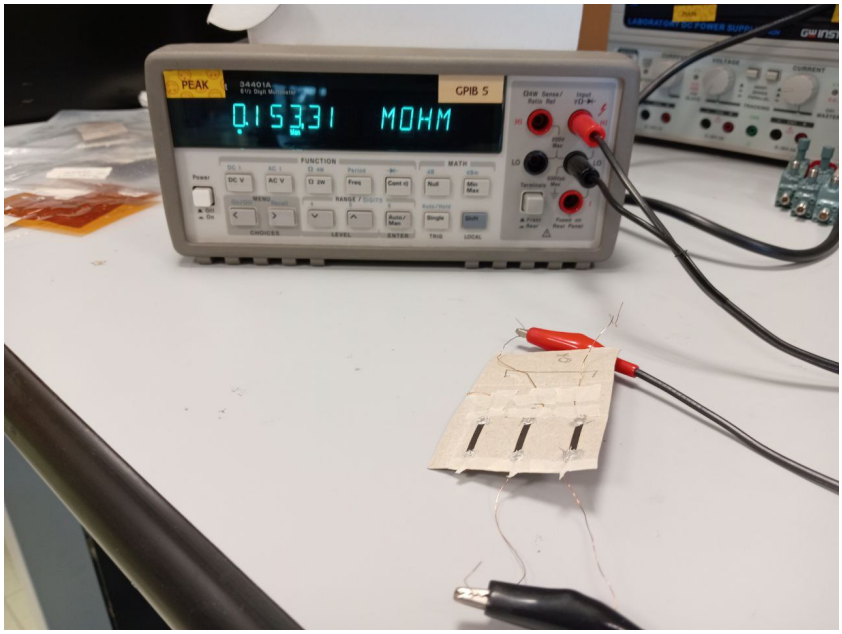

Figure 3.1: Measurement setup for the DC resistance with the KEYSIGHT 34401A multimeter

3.2 Results

In this section, the results in terms of DC resistance are summarized. The considered substrates are cardboard, corrugated cardboard and thick cardboard.

3.2.1 Cardboard

The following samples, performed with the parameters depicted in the table 3.1, are now considered. The substrate has been previously coated twice with flame retardant spray.

Geometry	Position	Power (% of 30 W)	DPI	Frequency (kHz)	Repetitions	Scan velocity (mm/s)	Measure: average ± half range
Straight	A	5	400	5	2	30	(3.8930 ± 0.0180) MΩ
Straight	B	5	400	5	2	30	(153.2000 ± 0.3000) kΩ
Straight	C	5	400	5	2	30	(26.1250 ± 0.0050) kΩ
Zigzag	A	5	400	5	2	30	(17.3900 ± 0.0200) kΩ
Zigzag	B	5	400	5	2	30	(31.0500 ± 0.0300) kΩ
Zigzag	C	5	400	5	2	30	(9.6753 ± 0.0085) kΩ
Straight	A	5	400	5	3	30	(26.5030 ± 0.2550) kΩ
Straight	B	5	400	5	3	30	(9.1995 ± 0.0085) kΩ
Straight	C	5	400	5	3	30	(10.8200 ± 0.0100) kΩ

Table 3.1: DC resistance of the conductive patterns on a two times flame retardant spray coated cardboard

The position of the samples in the triplet is defined in the following figures: figure 3.2a, figure 3.2b and figure 3.2c.

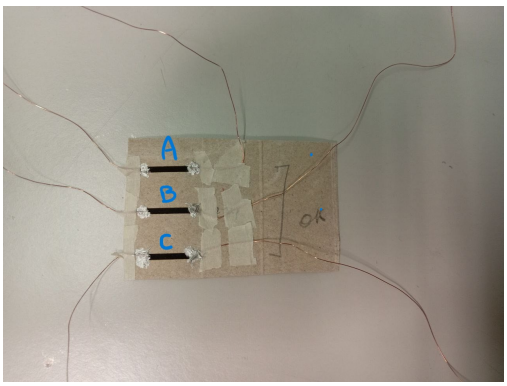

(a) Straight geometry, 2 repetitions

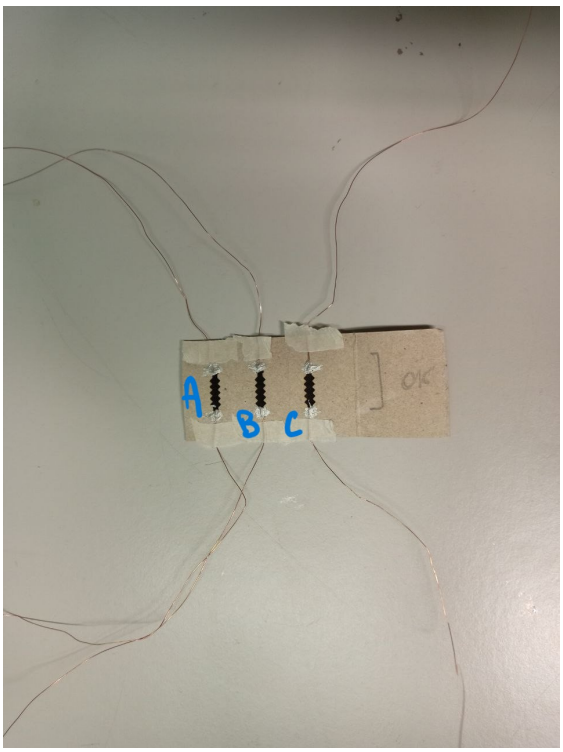

(b) Zigzag geometry, 2 repetitions

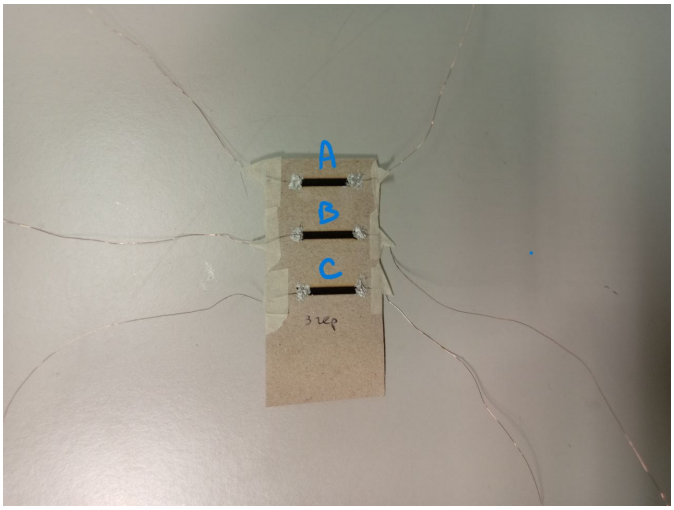

(c) Straight geometry, 3 repetitions

Figure 3.2: Straight geometry carbonaceous patterns on two times flame retardant spray coated cardboard

The samples A and B for the straight geometry exhibit a very high DC resistance, respectively of (3.8930 ± 0.0180) MΩ and of (153.2000 ± 0.3000) kΩ. That could mean a defect in the deposition of the contacts, since the DC resistance of the remaining sample in the triplet is significantly lower, (26.1250 ± 0.0050) kΩ. Indeed, if the wire is not well attached to the substrate, the resistance of the pattern would increase dramatically. It is important to highlight that the straight samples obtained with 3 as the number of repetitions led to a lower resistance with respect to the case of a lower number of repetitions: 2. This result is expected: considering a higher number of repetitions, the layer the formed carbonaceous pattern is more homogeneous and compact since the higher superficial heat that can induce the carbon atoms in the substrate to rearrange and form the char residue. The best result achieved in terms of DC resistance is the straight pattern created with 3 as the number of repetitions. The measured resistance is of (9.1995 ± 0.0085) $k\Omega$. This is the reason for not having persevered in the realization of new samples to state if the DC resistance values for the samples A and B of the first straight triplet depended on the silver deposition and wire attachment method.

3.2.2 Corrugated cardboard

The following samples, performed with the parameters depicted in the table 3.2, are now considered. The substrate has been previously three times covered with flame retardant spray.

Geometry	Position	Power (% of 30 W)	DPI	Frequency (kHz)	Repetitions	Scan velocity (mm/s)
Straight	A	1	400	5	2	30
Straight	B	1	400	5	2	30
Straight	C	1	400	5	2	30

Table 3.2: Experiments to obtain carbonaceous patterns on a three times flame retardant spray coated corrugated cardboard

The samples under study are the ones depicted in the figure 3.3.

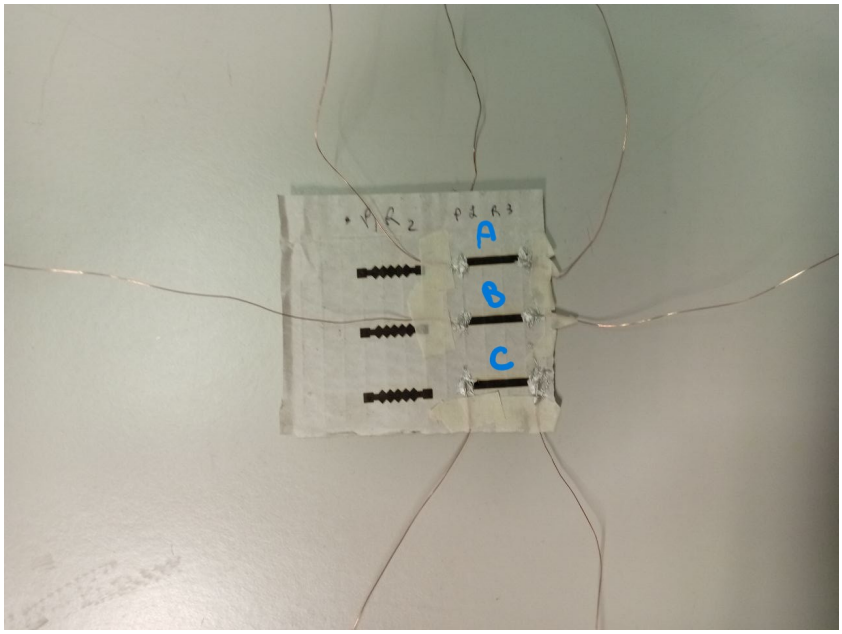

Figure 3.3: Straight geometry patterns on three times flame retardant spray coated corrugated cardboard

The DC measure of all the samples led to overload. Since the corrugated cardboard is made of a very thin layer of material, the LIG process on this substrate could have caused small breaks all along the pattern. This causes an interruption of the conductive path and hence a rise of the DC resistance.

3.2.3 Thick cardboard

The following table summarizes the results in terms of DC resistance of three times flame retardant spray coated thick cardboard. Table 3.3.

Geometry	Position	Power (% of 30 W)	DPI	Frequency (kHz)	Repetitions	Scan velocity (mm/s)	Measure: average ± half range (kΩ)
Straight	A	1	400	5	7	15	(1.3060 ± 0.0015)
Straight	B	1	400	5	7	15	(39.4000 ± 0.0400)
Straight	C	1	400	5	7	15	(9.7853 ± 0.0035)
Zigzag	A	1	400	5	7	15	(7.0090 ± 0.0010)
Zigzag	B	1	400	5	7	15	(5.7555 ± 0.0165)
Zigzag	C	1	400	5	7	15	(7.3478 ± 0.0035)

Table 3.3: DC resistance of the conductive carbonaceous patterns on a three times flame retardant spray coated thick cardboard

Consider the following equation:

$$\Delta R_{\%} = \frac{R_{max} - R_{min}}{R_{min}} \times 100 \tag{3.1}$$

The maximum and minimum DC resistance are registered for the samples of the straight triplet labeled as B and A, respectively of (39.4000 ± 0.0400) kΩ and (1.3060 ± 0.0015) kΩ As a first approximation the found DC resistance value, considering all the straight samples is in the range of: $R \in [R_{min}, R_{min} + \frac{\Delta R_{\%}}{100} R_{min}] = [1.3060, 1.3060 + 38.0960]\, k\Omega$.

The samples under test are those depicted in the following figure 3.4.

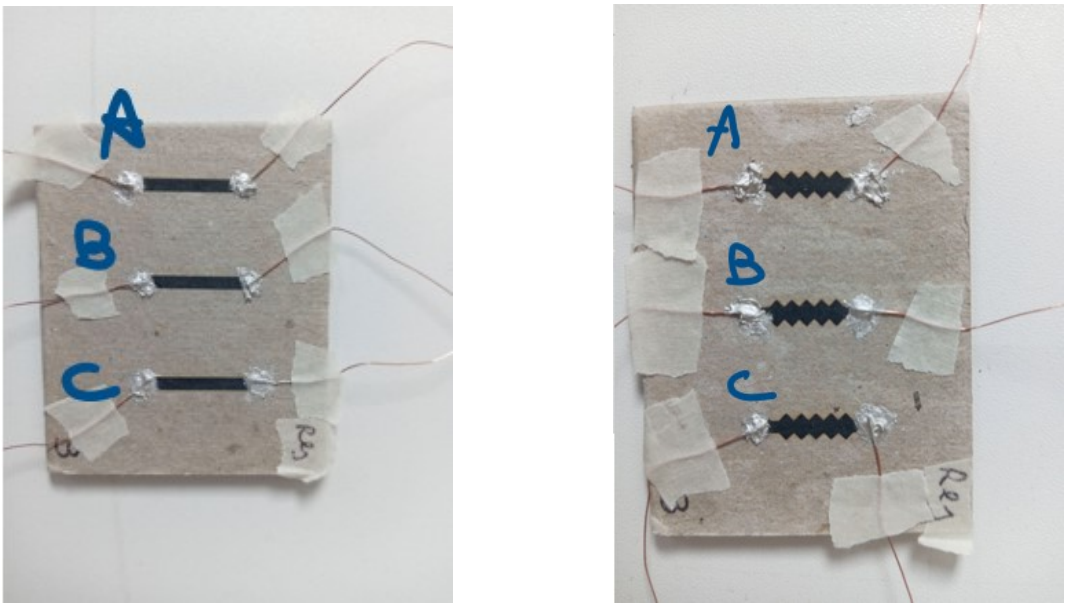

(a) Straight pattern

(b) Zigzag pattern

Figure 3.4: Straight and zigzag geometry patterns on three times flame retardant spray coated thick cardboard

The measured DC resistance for the implemented samples varies from approximately (1.3060 ± 0.0015) kΩ to (39.4000 ± 0.0400) kΩ for the straight geometry patterns and from (5.7555 ± 0.0165) kΩ to (7.3478 ± 0.0035) kΩ for the zigzag geometry patterns. The sample B of the straight geometry shows a DC resistance of (39.4000 ± 0.0400) kΩ. A reason for such a DC resistance could be deposition method of the flame retardant spray. Indeed, as explained in the section 2.2, that product has been deposited manually, trying to cover the whole surface in the most uniform way. Once the surface has been covered with one layer of the product, a new process begins to achieve the required number of anti flame layers. With this method it is inevitable to achieve more treated zones on the material's surface due to the overlapping process of different spray mechanisms. Considering this, the zones in the substrate which are richer in flame retardant spray result to be less suitable for enhancing the pyrolysis reaction needed for the LIG process.

To improve of the deposition method, automatized and controlled deposition processes should be investigated. The final goal is obtain the most uniform layer of flame retardant spray coating.

Considering the seven times coated thick cardboard, the corresponding experiments are shown in the following table 3.4.

Geometry	Position	Power (% of 30 W)	DPI	Frequency (kHz)	Repetitions	Scan velocity (mm/s)	Measure: average ± half range (kΩ)
Straight	A	1	400	5	7	15	OVL.D
Straight	B	1	400	5	7	15	OVL.D
Straight	C	1	400	5	7	15	(392.2000 ± 0.2500)
Zigzag	A	1	400	5	7	15	(614.3800 ± 0.8500)
Zigzag	B	1	400	5	7	15	OVL.D
Zigzag	C	1	400	5	7	15	(31.3200 ± 0.0100)

Table 3.4: DC resistance of the patterns on a seven times flame retardant spray coated thick cardboard

The DC resistances of the samples result to be generally high, of (392.2000 ± 0.2500) kΩ, (614.3800 ± 0.8500) kΩ or leading to overload. This result may depend on the high amount of flame retardant spray deposited. Indeed, the flame retardant spray limits the burning process of the substrate and hence it contrasts the development of the pyrolysis reaction, which is the key process for the formation of char residue. The sample labeled as "C" for the zigzag geometry shows a DC resistance of (31.3200 ± 0.0100) $k\Omega$. This value of DC resistance can be explained by the considerations done for the three times coated substrate: that sample may has been implemented in a less treated zone of the material, hence leading a lower value of DC resistance. Hence, also in this case, an automatized and controlled deposition method for the flame retardant spray should be investigated.

The LIG samples are depicted in the figure 3.5.

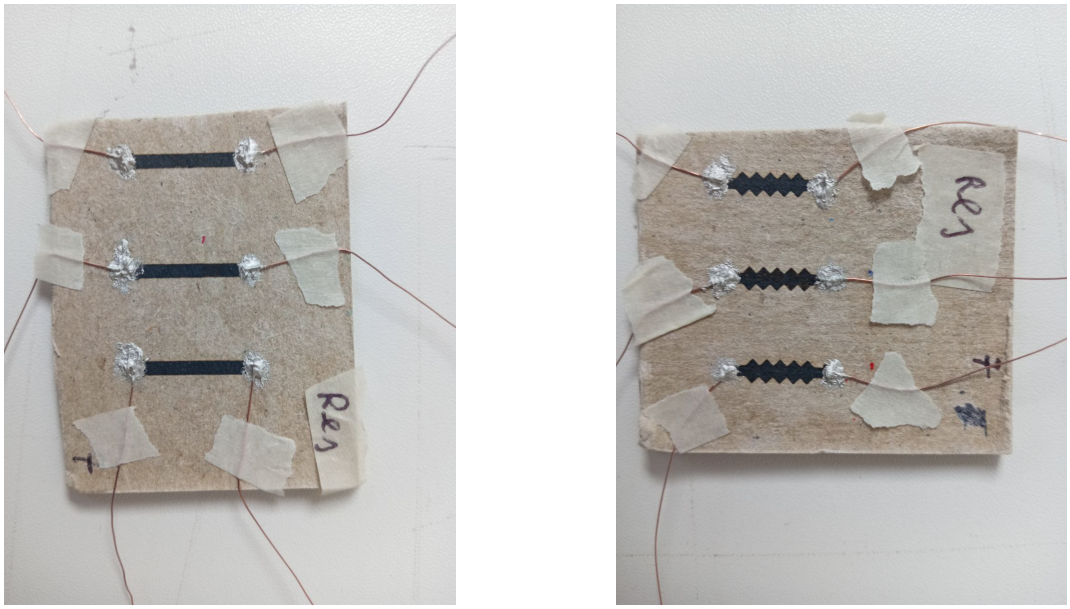

(a) Straight pattern

(b) Zigzag pattern

Figure 3.5: Straight and zigzag geometry patterns on seven times flame retardant spray coated thick cardboard

Considering the set of parameters that led to the best result in terms of DC resistance: table 3.3 and table 3.4, further experiments have been performed to investigate the results in terms of DC resistance of two other paper-based substrates: the front and back side of a paper-based plate. The experiments have also been performed again on cardboard. The latter, unlike corrugated cardboard, led to conductive carbonaceous patterns in light of the previously conducted experiments.

3.2.4 Front side of a paper-based plate

Now the front side of a paper-based plate is considered to perform LIG. The performed experiments are depicted in the following table 3.5. The substrate was firstly covered twice with the flame retardant spray.

Geometry	Position	Power (% of 30 W)	DPI	Frequency (kHz)	Repetitions	Scan velocity (mm/s)	Measure: average ± half range (kΩ)
Straight	A	1	400	5	7	15	(22.0350 ± 0.0150)
Straight	B	1	400	5	7	15	(20.4330 ± 0.0050)
Straight	C	1	400	5	7	15	(23.1280 ± 0.0050)
Zigzag	A	1	400	5	7	15	(14.2300 ± 0.0100)
Zigzag	B	1	400	5	7	15	(16.7900 ± 0.0100)
Zigzag	C	1	400	5	7	15	(17.7580 ± 0.0050)

Table 3.5: DC resistance of the conductive patterns on two times flame retardant spray coated front plate

Considering the equation 3.1, as a first approximation, the found DC resistance value considering all the straight samples is in the range of: $R \in [R_{min}, R_{min} + \frac{\Delta R_{\%}}{100} R_{min}] = [20.4330, 20.4330 + 2.6951]\, k\Omega$

The samples that have been measured are depicted in the following figure 3.6.

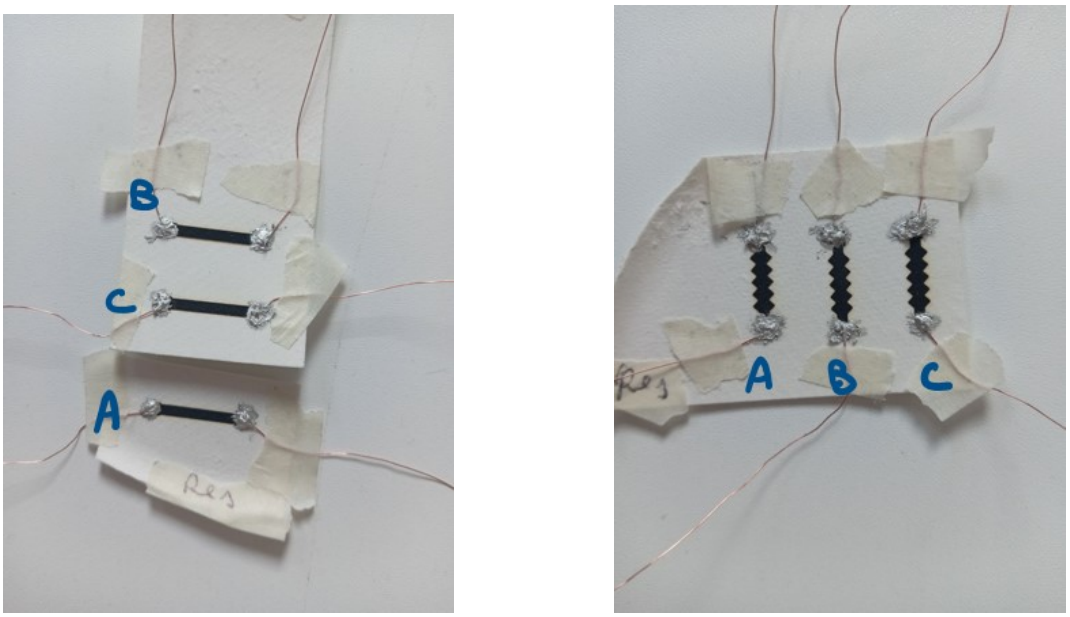

(a) Straight (b) Zigzag

Figure 3.6: Straight and zigzag geometry patterns on two times flame retardant spray coated front plate

3.2.5 Back side of a paper-based plate

The experiments considering the back side of the paper-based plate are now described in the following table 3.6. The substrate has been firstly treated covering it twice with the flame retardant spray.

Geometry	Position	Power (% of 30 W)	DPI	Frequency (kHz)	Repetitions	Scan velocity (mm/s)	Measure: average ± half range (kΩ)
Straight	A	1	400	5	7	15	(72.8800 ± 0.2100)
Straight	B	1	400	5	7	15	(126.2000 ± 0.2500)
Straight	C	1	400	5	7	15	(91.2850 ± 0.0450)
Zigzag	A	1	400	5	7	15	(36.3650 ± 0.0550)
Zigzag	B	1	400	5	7	15	(44.7600 ± 0.0300)
Zigzag	C	1	400	5	7	15	(50.8200 ± 0.0500)

Table 3.6: DC resistance of the conductive patterns on two times flame retardant spray coated back plate

The measured samples are those depicted in the following figure 3.7.

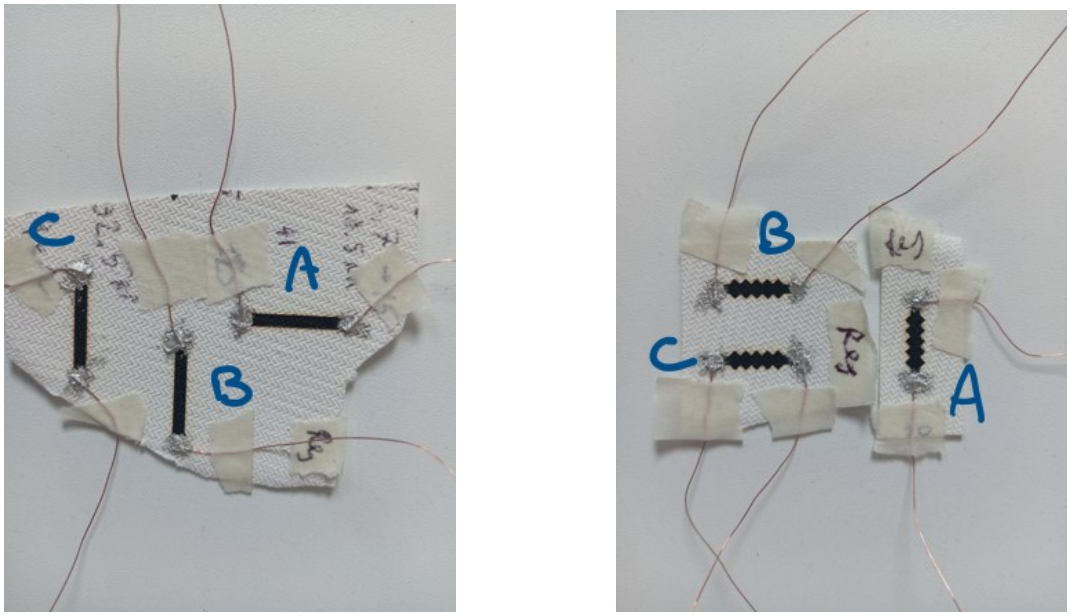

(a) Straight pattern

(b) Zigzag pattern

Figure 3.7: Straight and zigzag geometry patterns on two times flame retardant spray coated back plate

The measured DC resistance results to be higher than the one of the previous samples on the front plate, considering the same lasing parameters for the two substrates. An explanation for this behavior can be related to the flatness of the substrate. The back plate is not flat as the front one. Indeed, it has several grooves all around the surface. Those grooves can make the overall material be able to absorb more flame retardant spray than the front plate substrate. Hence, similarly to the case of using multiple layers of flame retardant spray, an excessive presence of it on the surface acts as a limiting factor for the pyrolysis reaction, resulting in a lower quality graphene layer.

3.2.6 Cardboard

In the following table 3.7 are summed up the performed experiments on cardboard, previously covered twice by the flame retardant spray.

Geometry	Position	Power (% of 30 W)	DPI	Frequency (kHz)	Repetitions	Scan velocity (mm/s)	Measure: average ± half range (kΩ)
Straight	A	1	400	5	7	15	(102.9000 ± 0.1500)
Straight	B	1	400	5	7	15	(231.9800 ± 0.2500)
Straight	C	1	400	5	7	15	(48.3800 ± 0.0250)
Zigzag	A	1	400	5	7	15	(85.5100 ± 0.1100)
Zigzag	B	1	400	5	7	15	(55.0600 ± 0.0750)
Zigzag	C	1	400	5	7	15	(37.9900 ± 0.0200)

Table 3.7: DC resistance of the patterns on two times flame retardant spray coated cardboard

The obtained LIG samples can be appreciated in the figure 3.8.

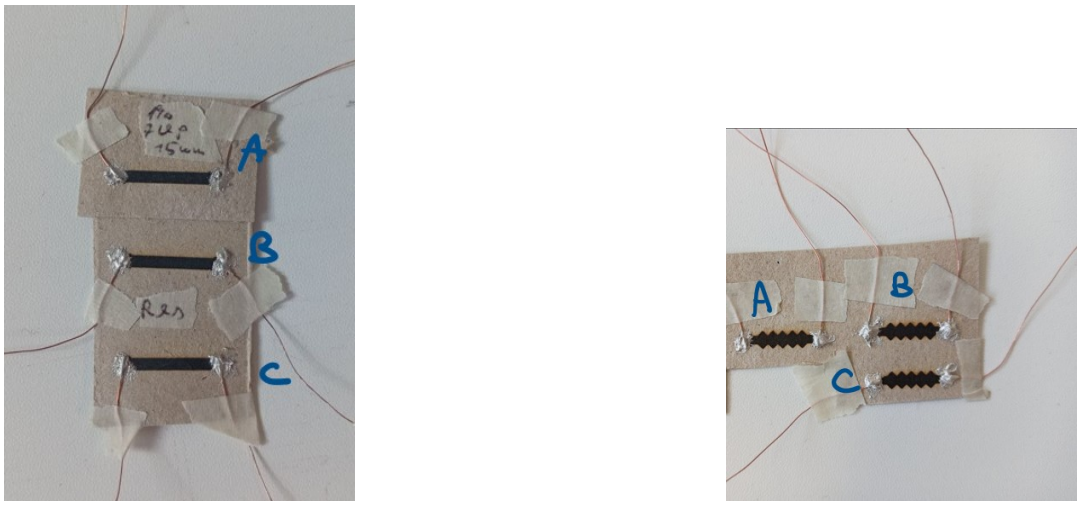

(a) Straight pattern

(b) Zigzag pattern

Figure 3.8: Straight and zigzag geometry patterns on two times flame retardant spray coated cardboard

The minimum and maximum value of the measured DC resistance of the samples is registered to be respectively of (48.3800 $\pm$ 0.0250) $k\Omega$ and (231.9800 $\pm$ 0.2500) $k\Omega$ for the straight geometry; respectively of (37.9900 $\pm$ 0.0200) $k\Omega$ and (85.5100 $\pm$ 0.1100) $k\Omega$ for the zigzag one. The samples exhibit an higher DC resistance with respect to the one obtained with the experiments in table 3.1.

3.3 Conclusions

The considered set of parameters, even if they apparently led a homogeneous and not burnt layer, they don't guarantee a comparable DC resistance with respect to the one of a metal connection. Furthermore, the second set of parameters led to a higher DC resistance considering the twice coated cardboard. To study if the LIG process can be used to implement on package antennas for agro-industry packages, an optimization process devoted to the minimization of the resistance should be conducted. Hence, the following chapter shows the optimization process of the lasing parameters and the relative results for the experiments on:

- Two times coated front side of a paper-based plate
- Three times coated front side of a paper-based plate: to study the impact of one more layer of flame retardant spray
- Three times coated thick cardboard

Chapter 4

Minimization of the DC resistance

The goal of the next set of experiments is to optimize the DC resistance value with respect to those found in the previous chapter 3. To achieve this, the lasing parameters must be carefully adjusted to find the highest possible energy dose required to properly enhance the LIG process and at the same time to avoid burnt areas. For all the substrates under study, the flame retardant spray has been deposited with the known method already explained in 2.2. Once the best set of parameters is found for each of the substrates, all the relative samples are then characterized by measuring their DC resistance.

4.1 Two times coated front plate

To minimize the DC resistance of the samples considering this substrate, the following experiments have been conducted: table 4.1. Both the lasing power and the DPI for experiment 1 have been increased with respect to the previous set of experiments 3.5. The frequency is kept constant, while the number of repetitions and the scan velocity have been adjusted to achieve less energy dose than the one obtainable if the latter two parameters were kept the same as in 3.5. Indeed, in that case the risk of burning the substrate would have been relevant. The second experiment keeps the same parameters as the first except for the lasing power and the number of repetitions, which have been respectively increased to the 3% and decreased to 1.

Experiment number	Power (% of 30 W)	DPI	Frequency, kHz	Repetitions	Scan velocity, mm/s
1	2	900	5	2	800
2	3	900	5	1	800

Table 4.1: Experiments for minimizing the DC resistance of the samples, two times coated front plate

The obtained patterns are shown in the figure 4.1.

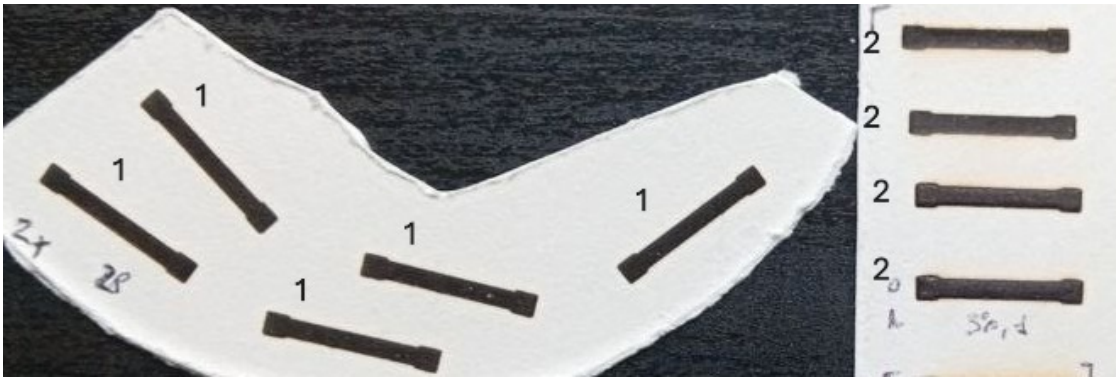

Figure 4.1: Straight samples on two times coated front plate

Experiment 1 is the one that led the best trade off between the homogeneity of the carbonaceous layer and the absence of burned regions.

4.1.1 Three times coated front plate

To evaluate the impact of one more flame retardant coating layer on the substrate, the previous experiments depicted in table 4.1 are performed this time on a three times flame retardant spray coated front plate.

The obtained patterns are shown in the figure 4.2.

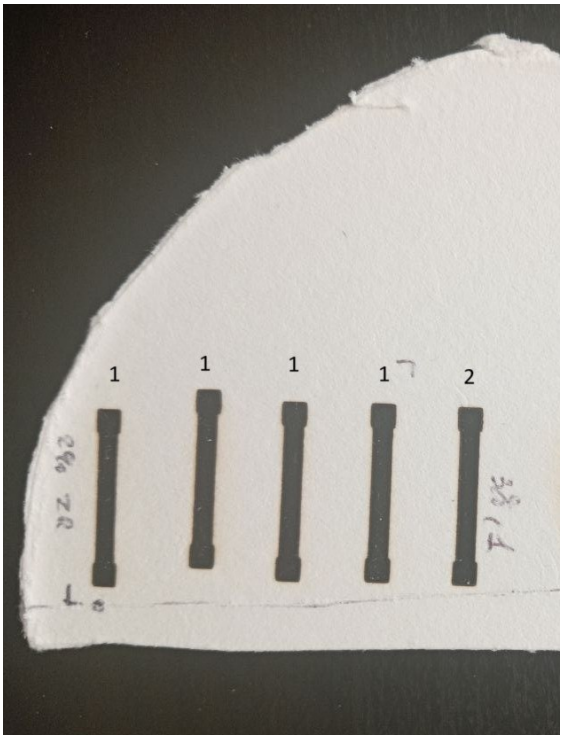

Figure 4.2: Straight samples on three times coated front plate

The found best set of parameters is the one of the experiment 1, as for the case of the two times coated plate. Slightly increasing the lasing power and reducing the number of repetitions led to a non conductive pattern.

4.2 Three times coated thick cardboard

The following experiments have been conducted: table 4.2. The starting point for all the experiments is the set of parameters which led to the best result for the previous substrates, table 4.1. The second and third set of parameters have been chosen by keeping all the parameters constant, except for the lasing power, which has been slightly increased respectively to the 3% and 4% and the number of repetitions, reduced to 1 for both the experiments. The experiment 4 relies on the same parameters of the second, except for the number of repetitions which has been increased to 2. With always the aim to carefully adjust the energy dose, the last experiment has been performed by using the minimum possible lasing power, the 1% and keeping all the other parameters the same as in the experiment 4.

Experiment number	Power (% of 30 W)	DPI	Frequency, kHz	Repetitions	Scan velocity, mm/s
1	2	900	5	2	800
2	3	900	5	1	800
3	4	900	5	1	800
4	3	900	5	2	800
5	1	900	5	2	800

Table 4.2: Experiments for minimizing the DC resistance of the samples, three times coated thick cardboard

The obtained patterns are shown in the figure 4.3.

Figure 4.3: Straight samples on three times coated front plate

The experiment 1 led to the highest level of conductivity and the absence of burns after the LIG process, considering all the performed experiments. Furthermore, the experiment 4 led to clearly visible burned regions around the sample. In the following sections, new samples have been realized, considering the found best set of parameters for each of the considered substrate. By always covering the substrates with the flame retardant spray

as in 2.2, five samples per substrates have been realized. On those, the procedure for the silver paste application and the attachment of the copper wires has been performed as in 3.1. As already done in the chapter 3, four different DC measures have been taken for each of the samples. At the end, a comparison between the obtained results considering the different sets of parameters has been carried out.

4.3 DC resistance of the two times coated front plate

The optimal set of parameters that have been found for this kind of substrate is the following:

- **Power (% of 30 W)**: 2%
- **DPI**: 900
- **Frequency, kHz**: 5
- **Repetitions**: 2
- **Scan velocity, mm s^{-1}**: 800

The new samples, after the silver paste deposition and copper wires attachment can be seen in figure 4.4.

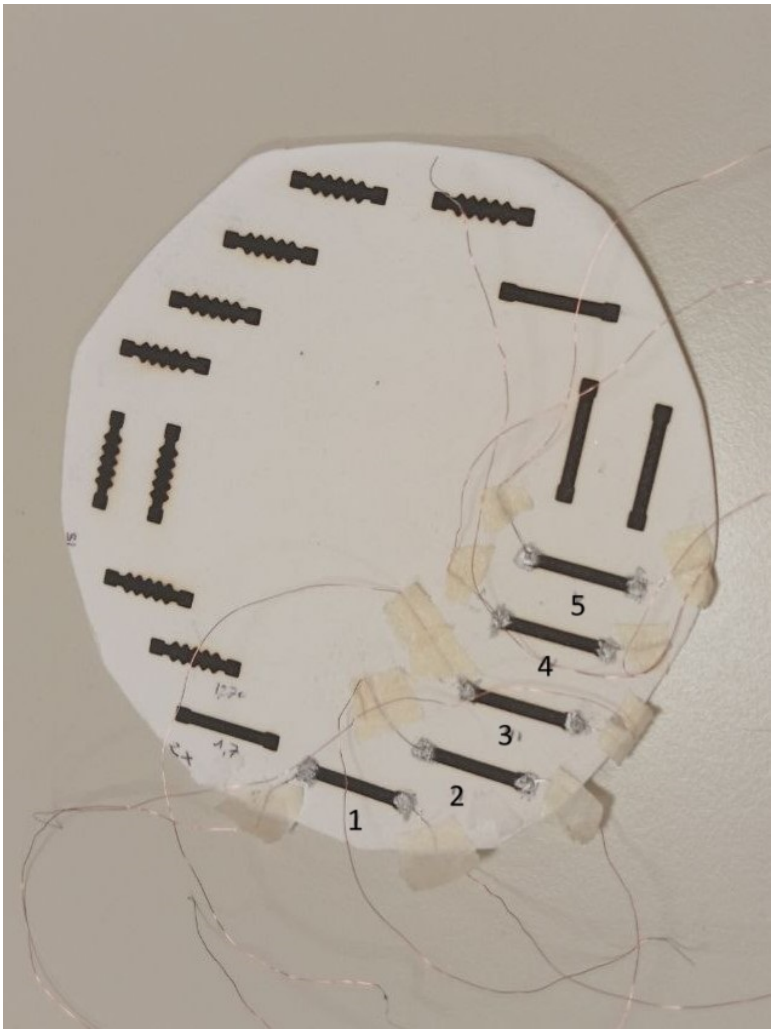

Figure 4.4: Straight patterns on two times flame retardant spray coated front plate

The results of the measurement of the DC resistance for each sample are depicted in the table 4.3.

Sample	Measure: average ± half range (kΩ)
1	(1.5208 ± 0.0005)
2	(1.2618 ± 0.0005)
3	(1.4165 ± 0.0005)
4	(1.5073 ± 0.0005)
5	(1.1858 ± 0.0005)

Table 4.3: DC resistance of straight LIG patterns on two times flame retardant spray coated front plate

In light of the obtained results, the maximum and minimum DC resistance are registered for the first and last sample: approximately (1.5208 ± 0.0005) kΩ and (1.1858 ± 0.0005) kΩ respectively.

As a first approximation, considering the equation 3.1: $R \in [R_{min}, R_{min} + \frac{\Delta R_{\%}}{100} R_{min}] = [1.1858, 1.1858 + 0.3350]\, k\Omega$

4.3.1 Three times coated front plate

The following samples have been obtained using the same lasing parameters as the previous. The resulting samples can be seen in figure 4.5.

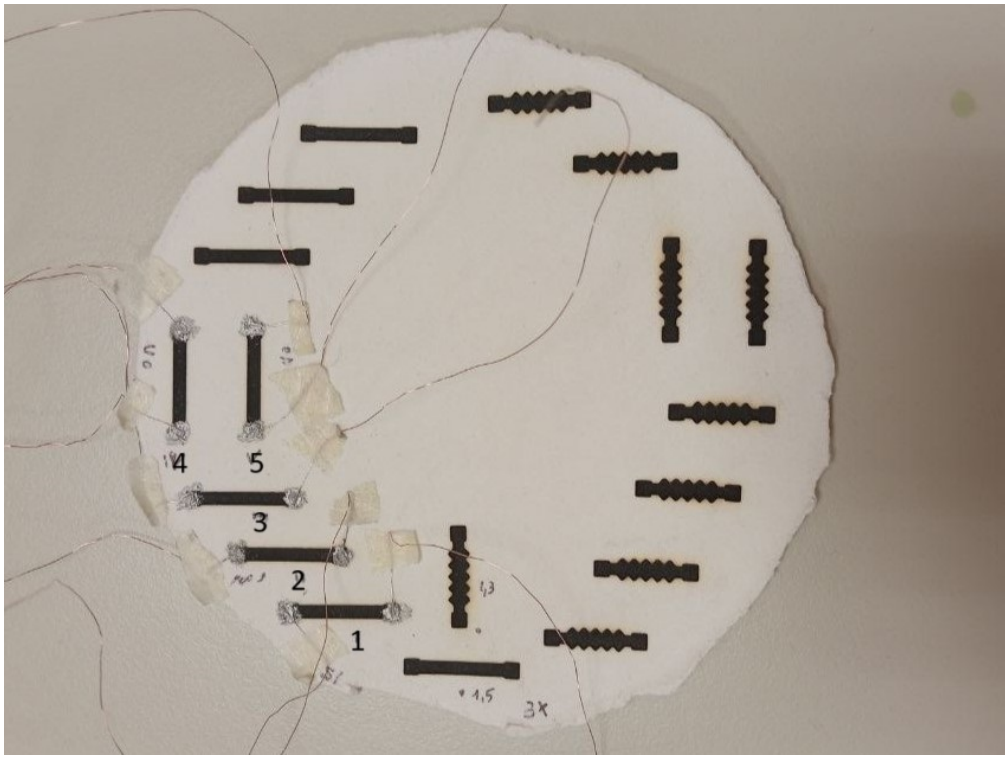

Figure 4.5: Straight patterns on three times flame retardant spray coated front plate

The results of the measurement of the DC resistance for each sample are depicted in the table 4.4.

Sample	Measure: average ± half range (kΩ)
1	(1.9533 ± 0.0005)
2	(3.5615 ± 0.0005)
3	(1.8288 ± 0.0010)
4	(2.8403 ± 0.0005)
5	(2.3028 ± 0.0005)

Table 4.4: DC resistance of straight LIG patterns on three times flame retardant spray coated front plate

In light of the obtained results, the maximum and minimum DC resistance are registered for the second and third sample: (3.5615 ± 0.0005) kΩ and (1.8288 ± 0.0010) kΩ respectively. As a first approximation and according to equation 3.1:

$R \in [R_{min}, R_{min} + \frac{\Delta R_{\%}}{100} R_{min}] = [1.8288, 1.8288 + 1.7328]\, k\Omega$

4.3.2 Three times coated thick cardboard

Always keeping the same lasing parameters, the resulting samples can be seen in figure 4.6.

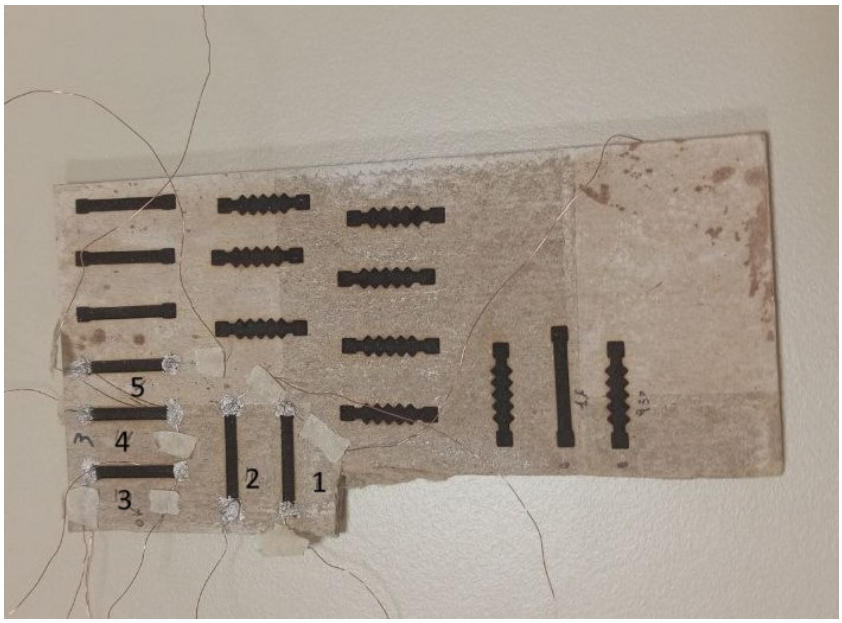

Figure 4.6: Straight patterns on three times flame retardant spray coated thick cardboard

The results of the measurement of the DC resistance for each sample are depicted in the table 4.5.

Sample	Measure: average ± half range (kΩ)
1	(2.7888 ± 0.0005)
2	(1.6585 ± 0.0005)
3	(1.1525 ± 0.0005)
4	(1.2778 ± 0.0005)
5	(0.9165 ± 0.0005)

Table 4.5: DC resistance of straight LIG patterns on two times flame retardant spray coated front plate

In light of the obtained results, the maximum and minimum DC resistance are registered for the first and last sample: (2.7888 ± 0.0005) kΩ and (0.9165 ± 0.0005) kΩ respectively. As a first approximation, according to the equation 3.1:
$R \in [R_{min}, R_{min} + \frac{\Delta R_{\%}}{100} R_{min}] = [0.9165, 0.9165 + 1.8723]\, k\Omega$

4.4 Conclusions

Considering the two front plate substrates, it is possible to appreciate how increasing the number of the flame retardant coatings the DC resistance values for the considered samples fall into ever larger intervals, considering the minimum registered resistance value as the first edge of the interval. Furthermore, all the samples on the three times coated exhibit an higher DC resistance:

- Front plate, two times coated: $R \in [1.1858, 1.1858 + 0.3350]\, k\Omega$
- Front plate, three times coated: $R \in [1.8288, 1.8288 + 1.7328]\, k\Omega$

Furthermore, considering the two substrates coated with the same number of flame retardant passages, the the DC resistance values for the considered samples fall into ever larger intervals as the thickness of the considered substrate increases.

- Front plate, three times coated: $\Delta R = 1.7328\, k\Omega$
- Thick cardboard, three times coated: $\Delta R = 1.8723\, k\Omega$

The first result can be explained by the fact that, according to how the flame retardant spray has been deposited, already explained in section 2.2, increasing the amount of spray, the overlapping mechanism between multiple depositions increases. That leads to the non uniformity of the resulting coating and hence the obtaining of more variable resistance values.

Considering the second result achieved, it can be explained by the fact that considering a thicker substrate, the overlapping mechanism resulting from the flame retardant spray deposition would occur in the direction of the thickness of the substrate also, leading more variable resistance values. Indeed, considering the front plate substrate, the overlapping process can be assumed to occur only on the surface of the material, thanks to the tininess of the substrate. By increasing the thickness of the substrate the overlapping process

becomes relevant in the third dimension also, hence leading to a further non uniformity of the resistance values.

Considering the comparison of the results obtained with the previous set of parameters, consider the following graphs. In each plot, the two DC measurement curves are represented. In this way, it is possible to appreciate the improvement in DC resistance achieved with the new set of lasing parameters. Figure 4.7, figure 4.8.

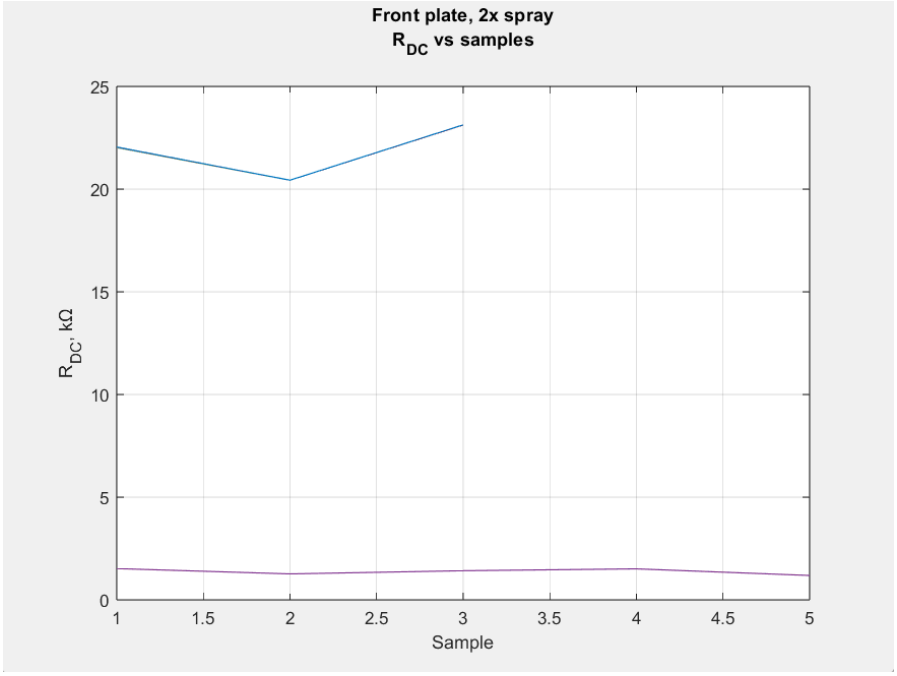

Figure 4.7: Non optimized set of parameters: blue. Optimized set of parameters: purple

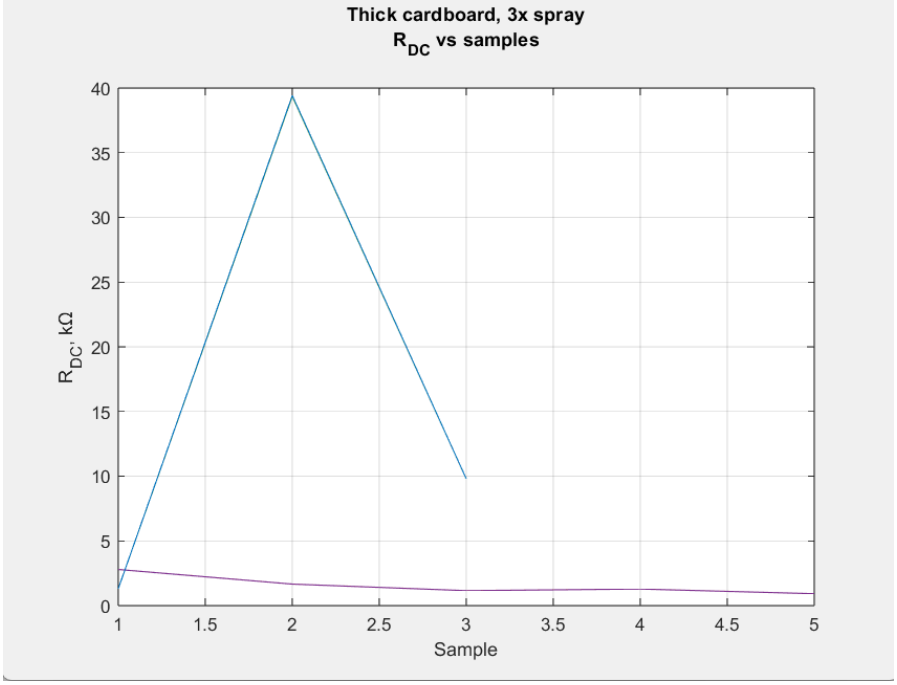

Figure 4.8: Non optimized set of parameters: blue. Optimized set of parameters: purple

The new set of parameters led to an improvement of the conductivity of the samples, for all the two substrates that have been taken into account. The average DC reduction has been:

- $AvRed_{front2x} = 93.5984\%$
- $AvRed_{thick3x} = 23.4929\%$

The average reduction of the DC resistance has been calculated as it follows: for each sample and each measure, the percentage reduction between the two DC resistances has been evaluated: equation 4.1.

$$Red(sample, meas) = \frac{R_{DC_i}(sample, meas) - R_{DC_f}(sample, meas)}{R_{DC_i}(sample, meas)} \times 100 \qquad (4.1)$$

After that, an average value has been obtained, considering the four measures for each sample. The final average value is the average considering all the samples. For the first sample of the thick cardboard, an increasing of the DC resistance was recorded, in contrast from what happens for the other two samples. Indeed, only considering those, the calculated average reduction of the resistance is the 92.0062% The increase of the resistance considering the first sample can be explained taking into account that, in the zone of the substrate where the first sample has been created, an accumulation of the flame retardant spray could has been formed, making the substrate in that zone more

resilient for the creation of conductive patterns. On top of the achieved reduction of DC resistance, the optimized set of parameters led to an improvement of the repeatability of the process also. At this purpose, considering the following table 4.6. The parameter ΔR can be evaluated by the equation 3.1: $\Delta\mathrm{R} = \frac{\Delta R_{\%}}{100} \times R_{min}$; $R \in [R_{min}, R_{min} + \Delta R]$

Substrate	ΔR (kΩ), first set	ΔR (kΩ), optimized set	Reduction (%)
Front plate, 2x	2.6951	0.3350	87.5700
Thick cardboard, 3x	38.0960	1.8723	95.0853

Table 4.6: Comparison of the achieved DC resistance range, between the not optimized and the optimized set of parameters

In the following chapter an AC characterization of the previous samples is conducted to evaluate the magnitude and phase of their impedance versus frequency.

Chapter 5

AC study of the impedance

The aim of this chapter is to understand the behavior of the samples versus frequency to state the future feasibility of the LIG process to implement on package antennas. The "Agilent E4980A Precision LCR Meter" was used as the instrument to perform the following analysis. The latter is a vector impedance meter with which four-probe measurements have been conducted. In particular, the measurement of the magnitude and the phase of the impedance for each sample has been conducted.

The instrument and the measurement setup can be appreciated in the following figure 5.1.

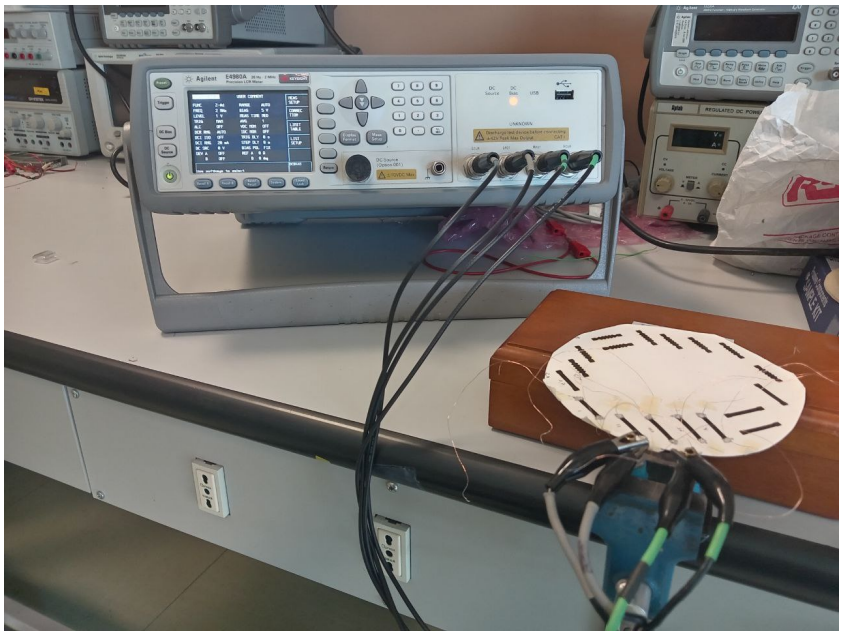

Figure 5.1: Agilent E4980A Precision LCR Meter and measurement setup

As anticipated, the instrument provides four probes: H_{pot}, H_{curr}, L_{pot}, L_{curr}. Each

measure has been conducted by shorting the H_{pot}, H_{curr} and the L_{pot}, L_{curr} probes. Consider the resulting equivalent circuit: figure 5.2.

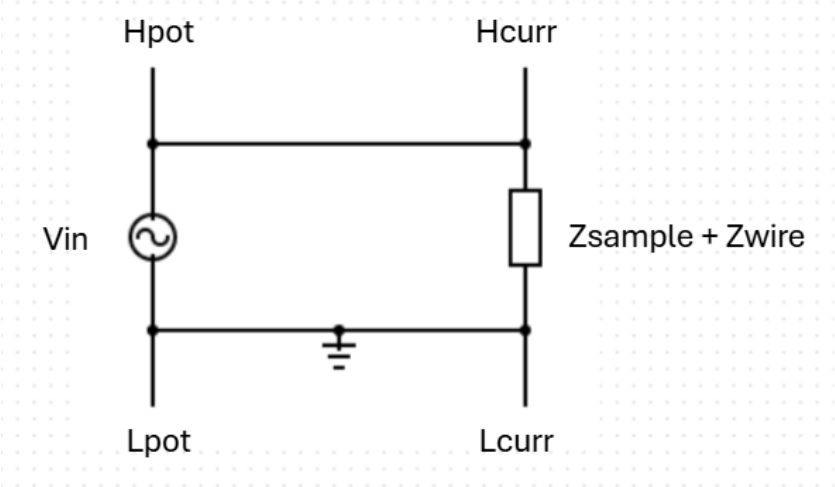

Figure 5.2: Equivalent electric circuit for the measures

In this way, since the input voltage is taken at the source and the relative current is evaluated exactly at the load, there are no effects of the connecting wires from the instrument. Instead, the effect of the copper wires that connect the probes to each sample is considered in the measures. At the frequencies under study, their effect is negligible. Indeed, a calibration of the instrument has been firstly done. At this purpose, consider the section 5.5 where the magnitude and the phase of the copper wires have been measured. The AC characterization relies on 30 frequencies from 20 Hz to 2 MHz, linearly distributed. The measurements, while not explicated, have been evaluated considering an AC voltage signal with 0 V bias and 1 V_{rms} as amplitude. The performed analysis are the following:

- Extraction of R_s and C_s: equivalent series resistance and capacitance of the sample, from the series model: figure 5.3a. This analysis aims to understand if the sample under test can be modeled as a resistance and a capacitance in series for all the considered frequencies
- Extraction of R_p and C_p: equivalent parallel resistance and capacitance of the sample, from the parallel model: figure 5.3b. This analysis aims to understand if the sample under test can be modeled as a resistance and a capacitance in parallel for all the considered frequencies
- Measure of magnitude $|Z|$ and phase θ of the sample's impedance
- With the extracted R_s and C_s, the relative magnitude $|Z_s|$ and phase θ_s have been computed. Then, those are compared with $|Z|$ and θ. This analysis aims to verify the correctness of the extraction of the series model: the impedance $|Z_s|$ and the phase θ_s should overlap with the measured magnitude and phase respectively

- With the extracted R_p and C_p, the relative magnitude $|Z_p|$ and phase θ_p have been computed. Then, those are compared with $|Z|$ and θ. This analysis aims to verify the correctness of the extraction of the parallel model: the impedance $|Z_p|$ and the phase θ_p should overlap with the measured magnitude and phase respectively

For the first and second samples for each substrate, the following further analysis are performed:

- AC linearity: evaluation of the dependence of the magnitude $|Z|$ and the phase θ of the sample's impedance with a variation of the amplitude of the input AC voltage signal. The second amplitude considered for the input AC voltage signal is of $0.5\,V_{rms}$
- DC linearity: evaluation of the dependence of the magnitude $|Z|$ and the phase θ of the sample's impedance a variation of the DC bias of the input AC voltage signal. The considered bias voltages are: 1 V, 3 V and 5 V

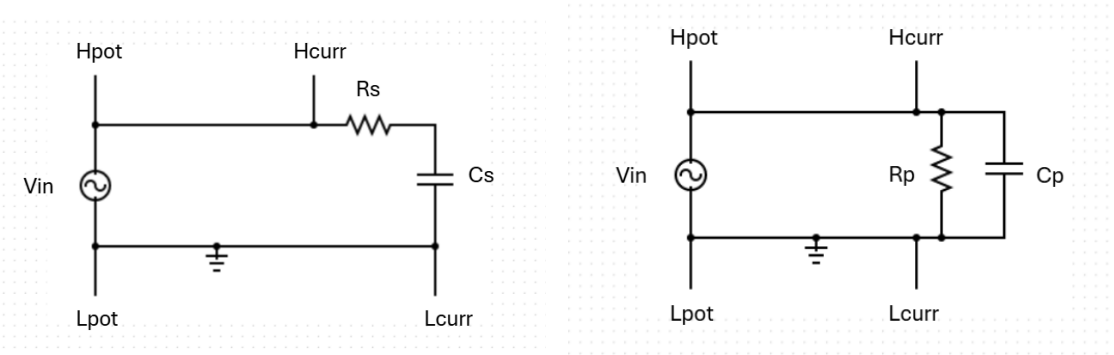

(a) Series model (b) Parallel model

Figure 5.3: Equivalent circuit models

The series and parallel resistances and capacitances, as well as the magnitudes and phases of the impedances have been determined by performing four different measurements. All these measurements have been superimposed on the corresponding graphs. Furthermore, considering the plots of the magnitude and phase; the series, the parallel magnitude and the corresponding phases have also been included in the relative graphs to state, as anticipated, the correctness of the model's extraction. In this chapter, the results considering the first two samples for each substrate are reported and examined. The results for the other samples can be seen in the appendix A. As it can be seen for the corresponding plots, the parallel model is the best suited for replicating each sample's behavior. This conclusion is expected. Indeed, considering the plots in figures 5.10, 5.17, 5.24, 5.31, 5.38, 5.45, where the behavior of the samples versus the DC bias is examined, there's a minimal dependence with the DC. This clearly states the impossibility to model the sample with a series capacitance.

5.1 Two times coated front plate

The lasing parameters to obtain the samples in figure 4.4 can be consulted in the section 4.3.

5.1.1 1st sample

The results for the previously depicted analysis can be seen in the figures 5.4, 5.5, 5.6, 5.7, 5.8, 5.9, 5.10.

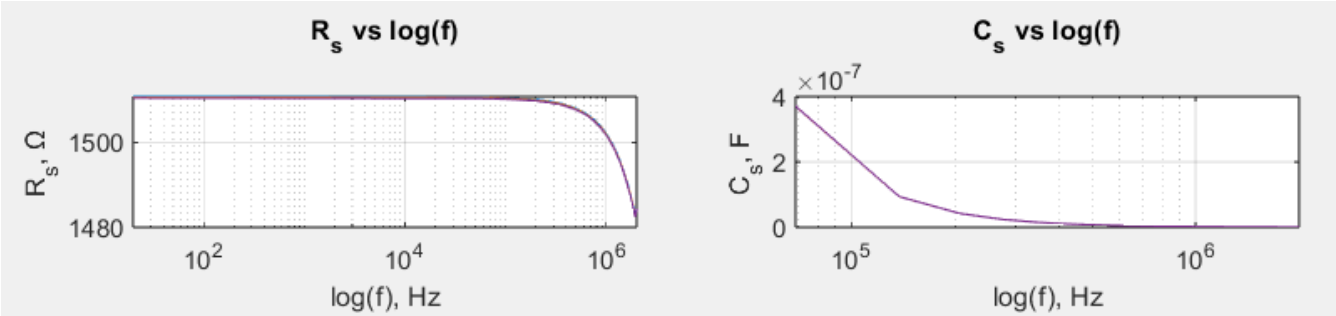

Figure 5.4: R_s and C_s versus log(f)

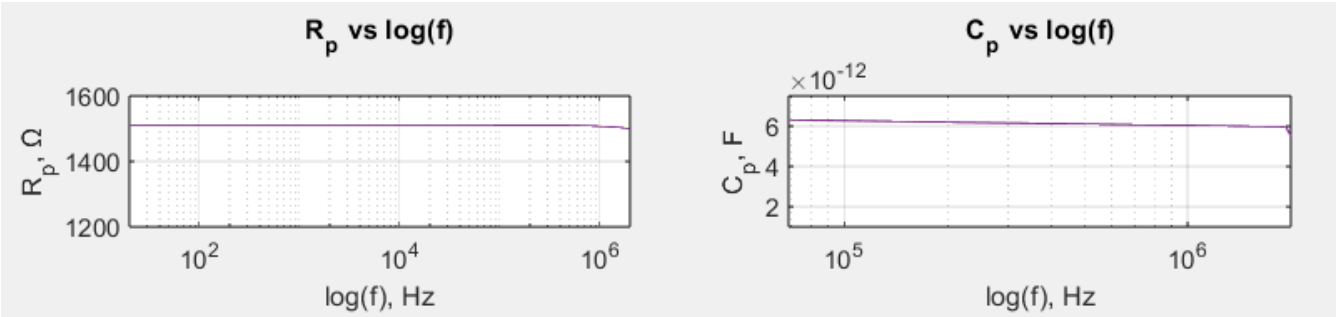

Figure 5.5: R_p and C_p versus log(f)

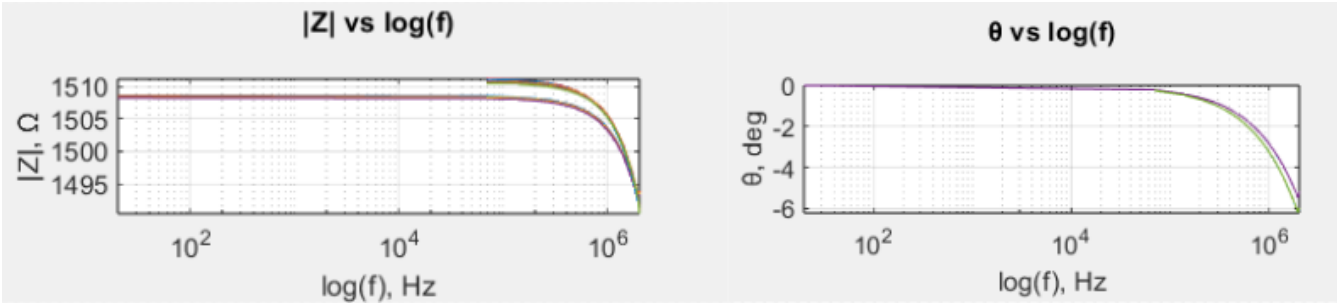

Figure 5.6: $|Z|$ and θ versus log(f)

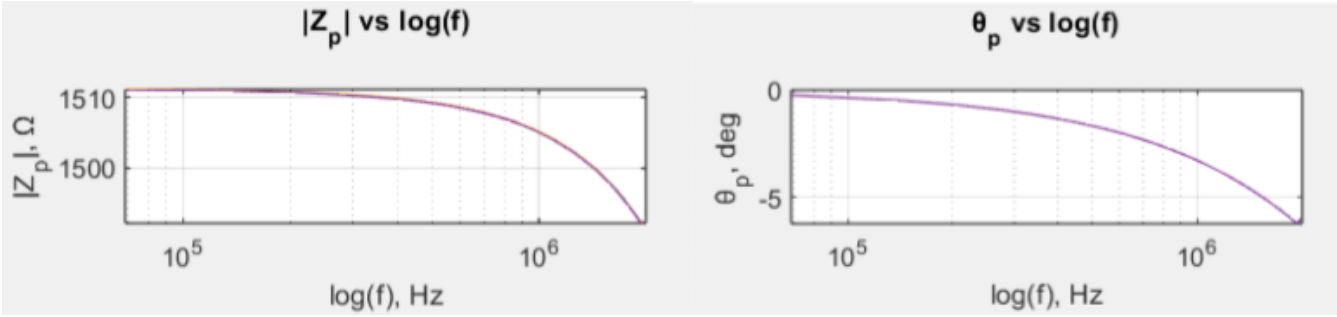

Figure 5.7: $|Z_p|$ and θ_p versus log(f)

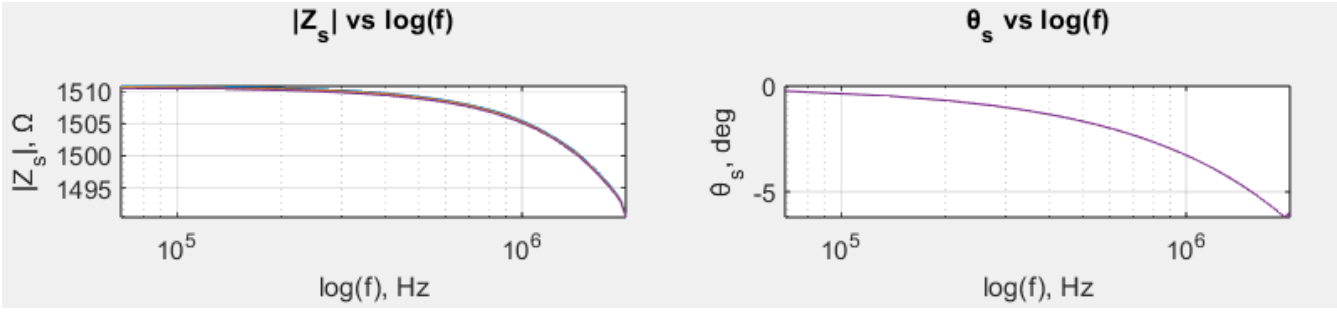

Figure 5.8: $|Z_s|$ and θ_s versus log(f)

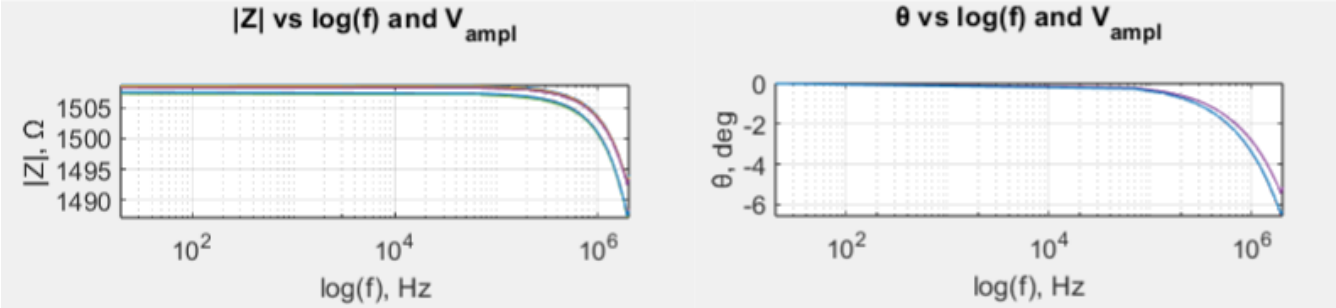

Figure 5.9: $|Z|$ and θ versus log(f) and V_{amp}, V_{rms}

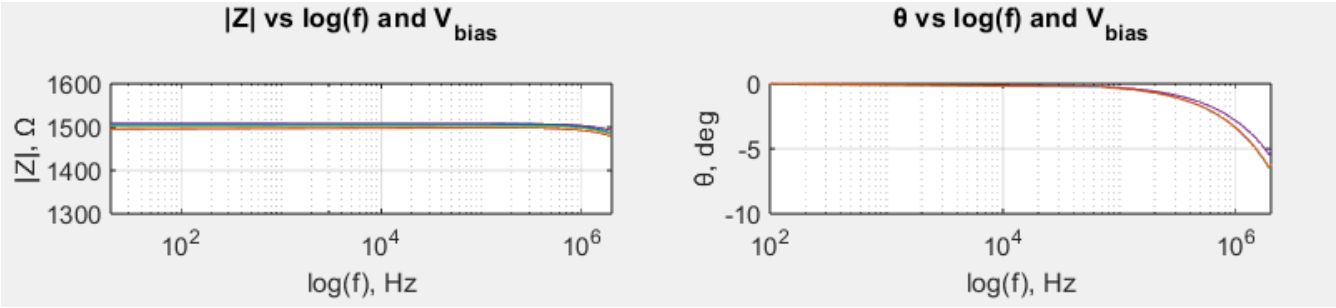

Figure 5.10: $|Z|$ and θ versus log(f) and V_{bias}

5.1.2 2nd sample

The results for the previously depicted analysis can be seen in the figures 5.11, 5.12, 5.13, 5.14, 5.15, 5.16, 5.17.

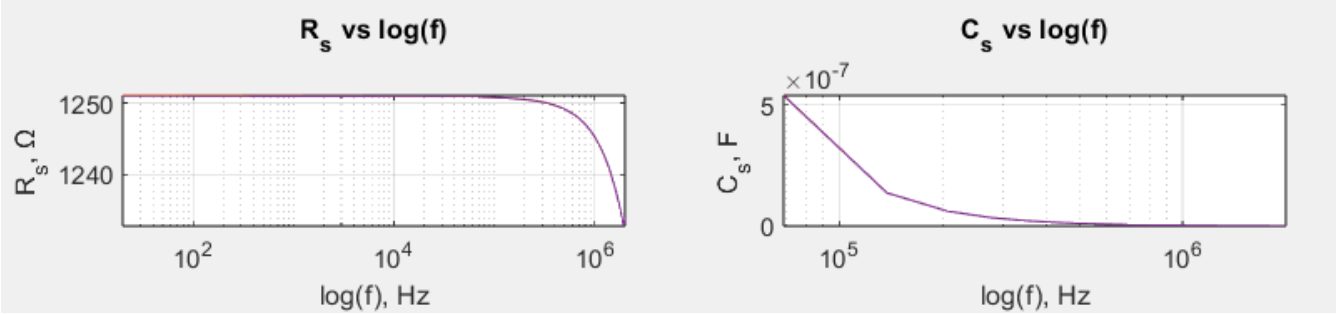

Figure 5.11: R_s and C_s versus log(f)

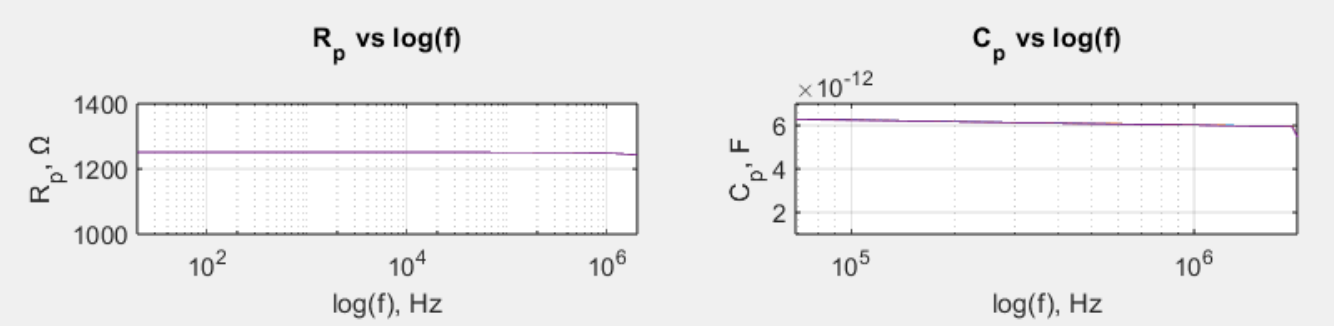

Figure 5.12: R_p and C_p versus log(f)

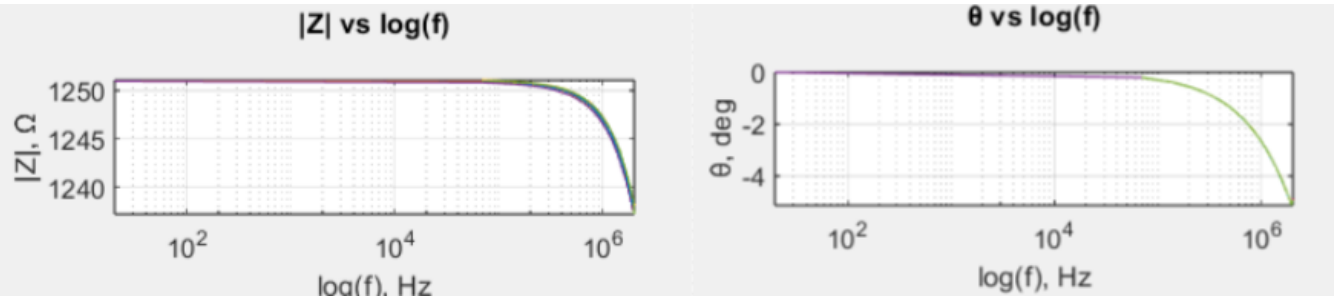

Figure 5.13: $|Z|$ and θ versus log(f)

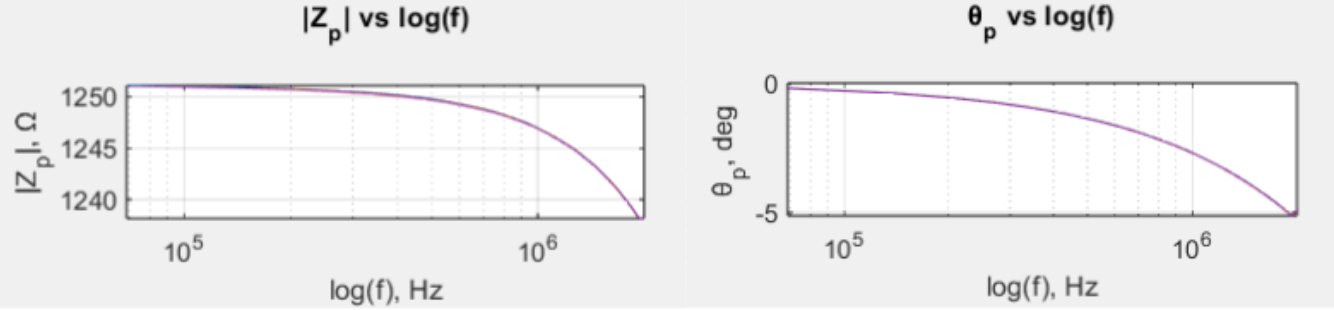

Figure 5.14: $|Z_p|$ and θ_p versus log(f)

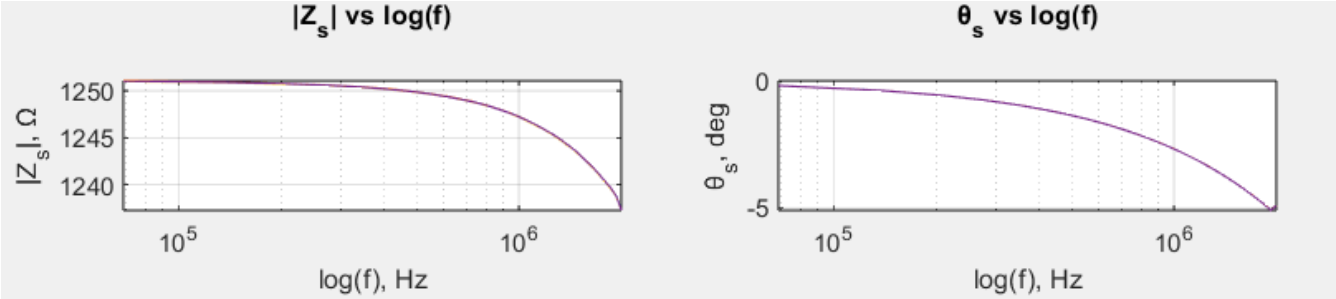

Figure 5.15: $|Z_s|$ and θ_s versus log(f)

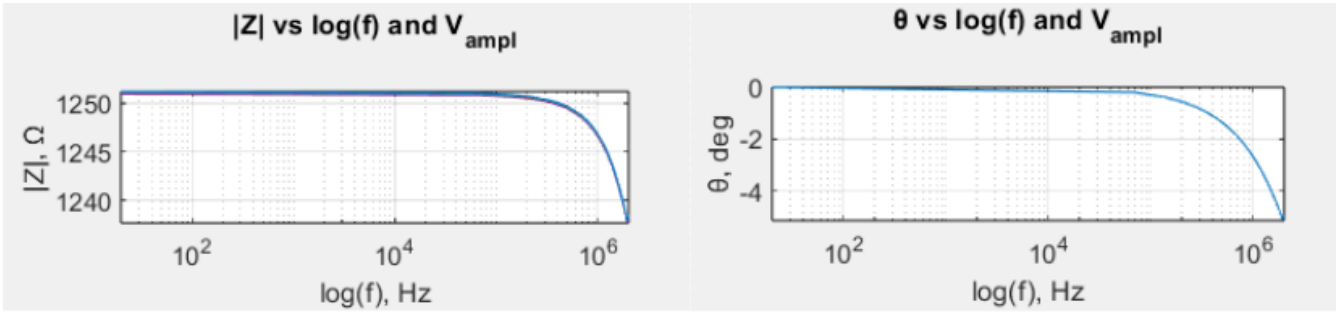

Figure 5.16: $|Z|$ and θ versus log(f) and V_{amp}, V_{rms}

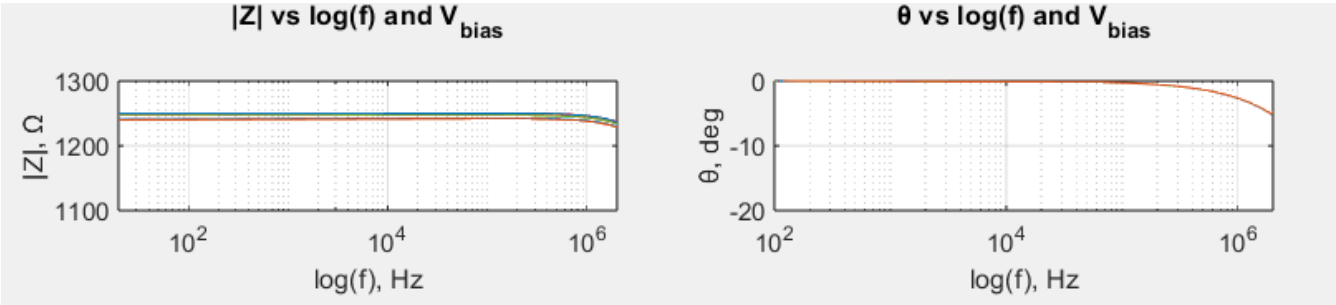

Figure 5.17: $|Z|$ and θ versus log(f) and V_{bias}

5.2 Three times coated front plate

The lasing parameters to obtain the samples in figure 4.5 can be consulted in the section 4.3.1.

5.2.1 1st sample

The results for the previously depicted analysis can be seen in the figures 5.18, 5.19, 5.20, 5.21, 5.22, 5.23, 5.24.

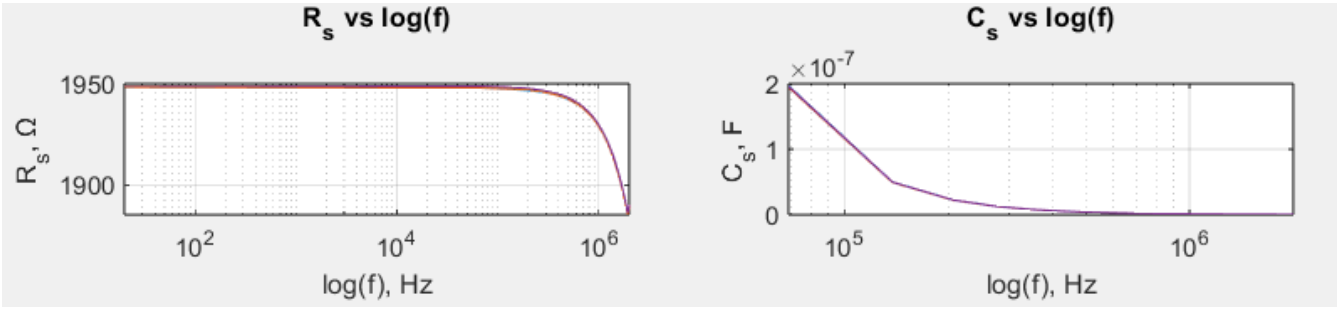

Figure 5.18: R_s and C_s versus log(f)

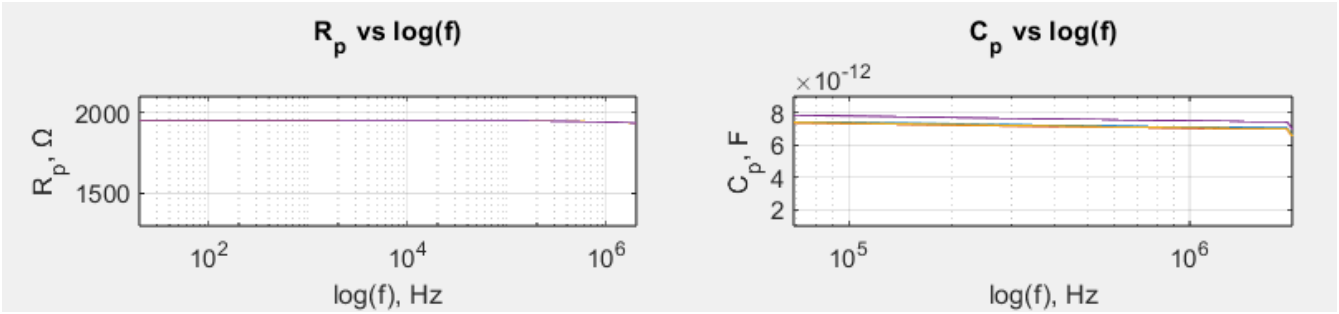

Figure 5.19: R_p and C_p versus log(f)

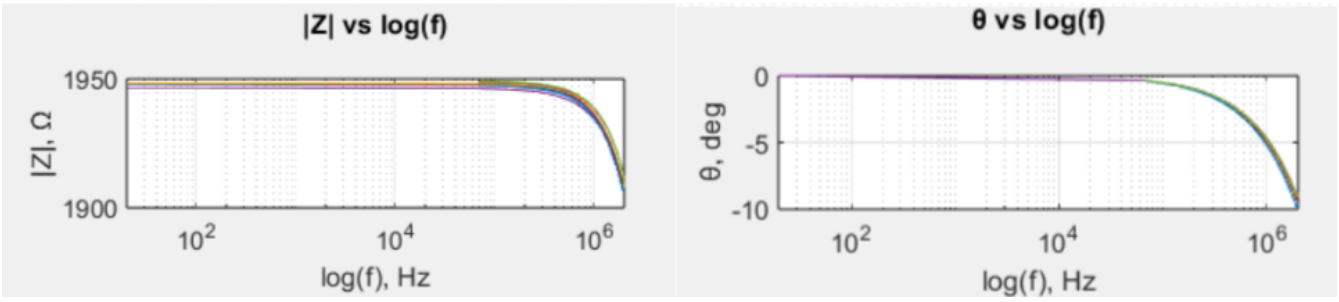

Figure 5.20: $|Z|$ and θ versus log(f)

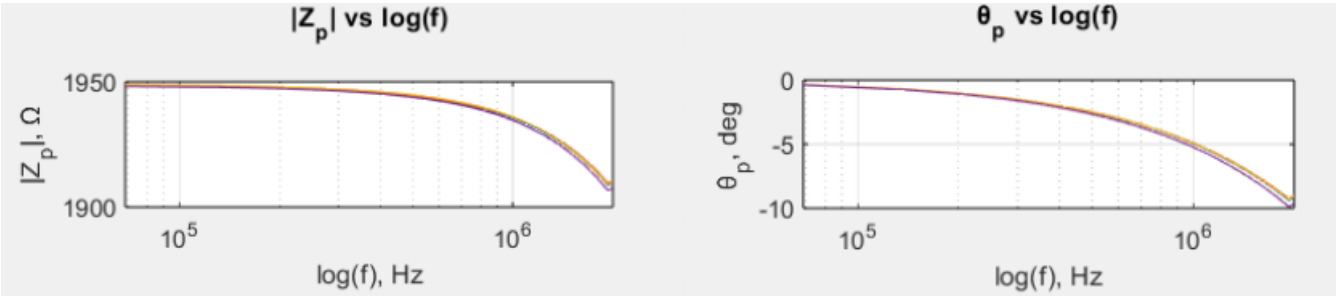

Figure 5.21: $|Z_p|$ and θ_p versus log(f)

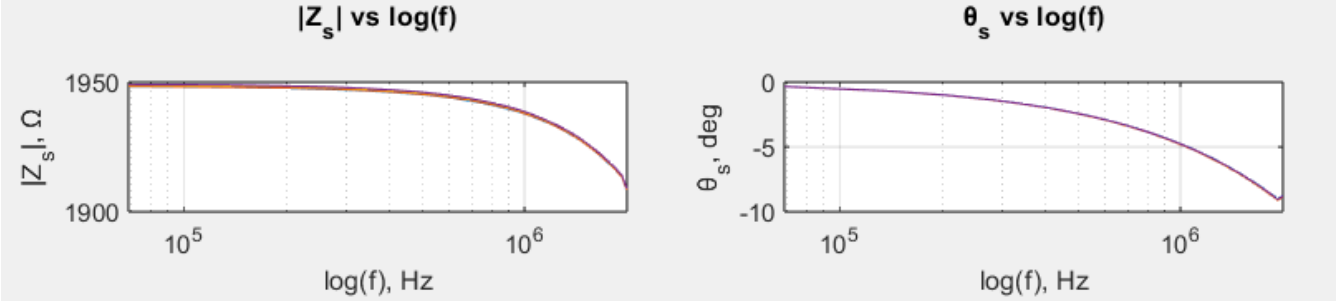

Figure 5.22: $|Z_s|$ and θ_s versus log(f)

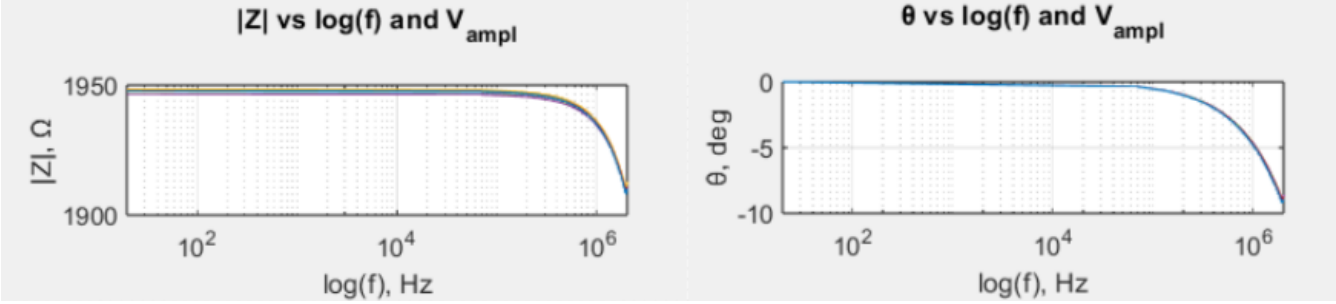

Figure 5.23: $|Z|$ and θ versus log(f) and V_{amp}, V_{rms}

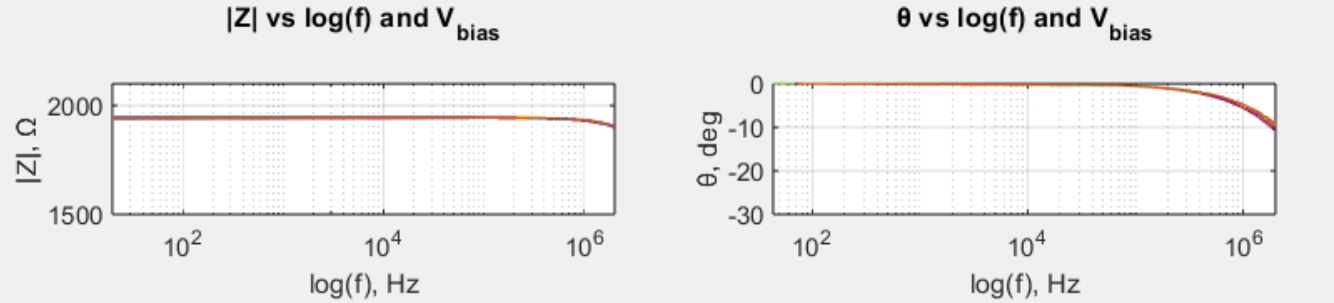

Figure 5.24: $|Z|$ and θ versus log(f) and V_{bias}

5.2.2 2nd sample

The results for the previously depicted analysis can be seen in the figures 5.25, 5.26, 5.27, 5.28, 5.29, 5.30, 5.31.

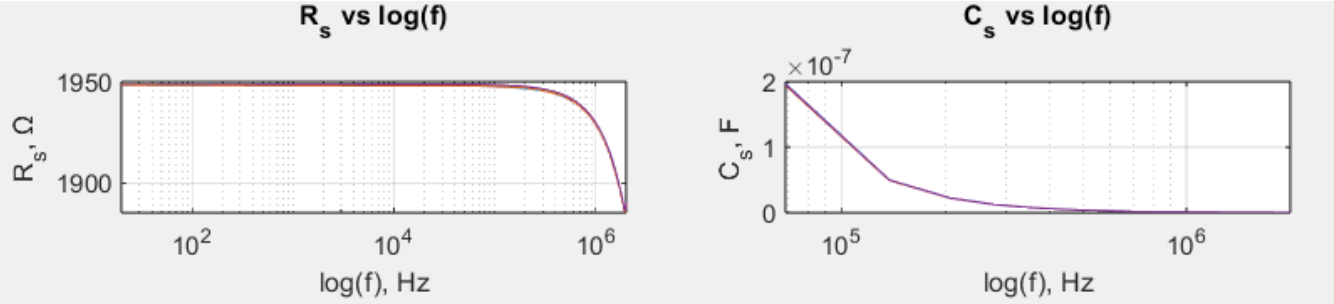

Figure 5.25: R_s and C_s versus log(f)

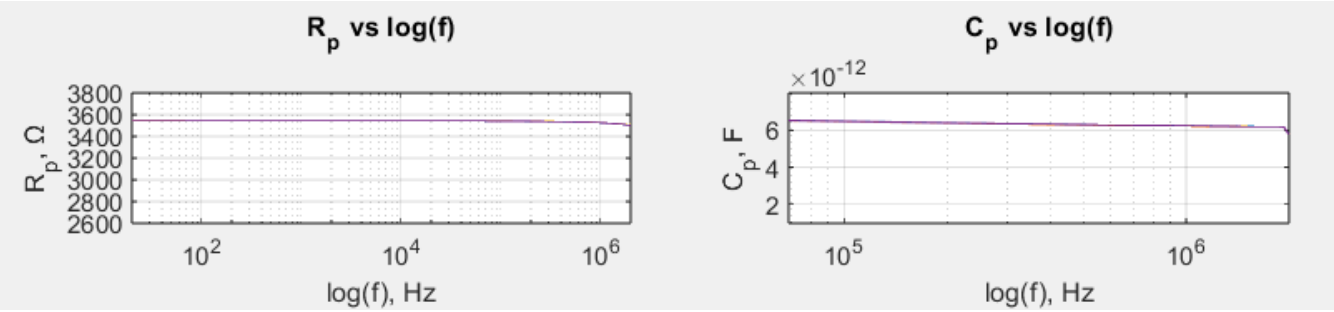

Figure 5.26: R_p and C_p versus log(f)

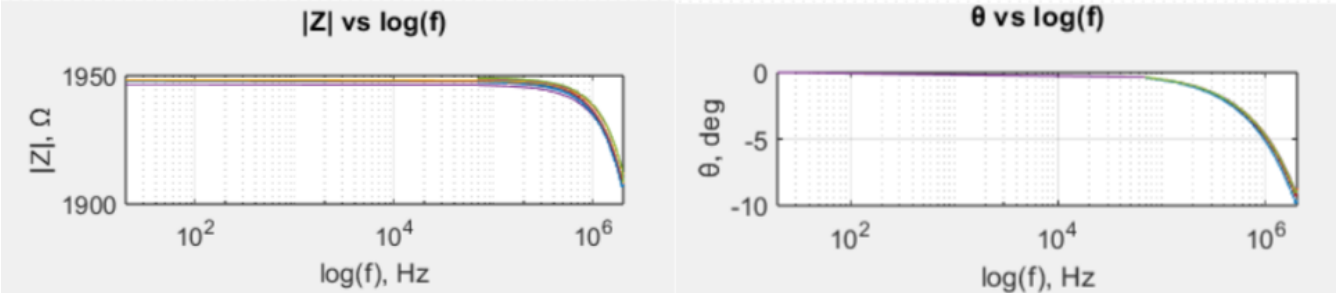

Figure 5.27: $|Z|$ and θ versus log(f)

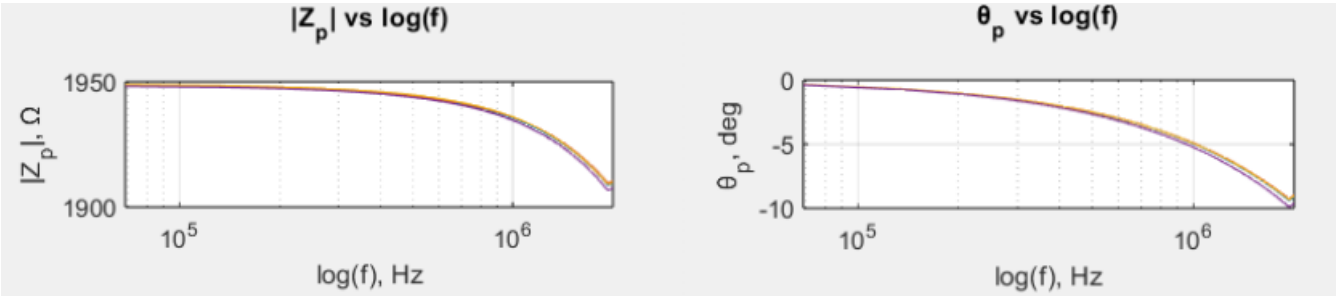

Figure 5.28: $|Z_p|$ and θ_p versus log(f)

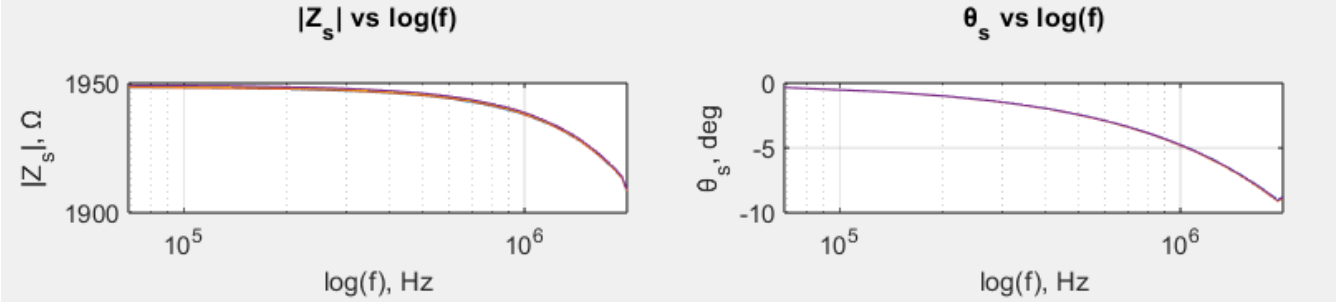

Figure 5.29: $|Z_s|$ and θ_s versus log(f)

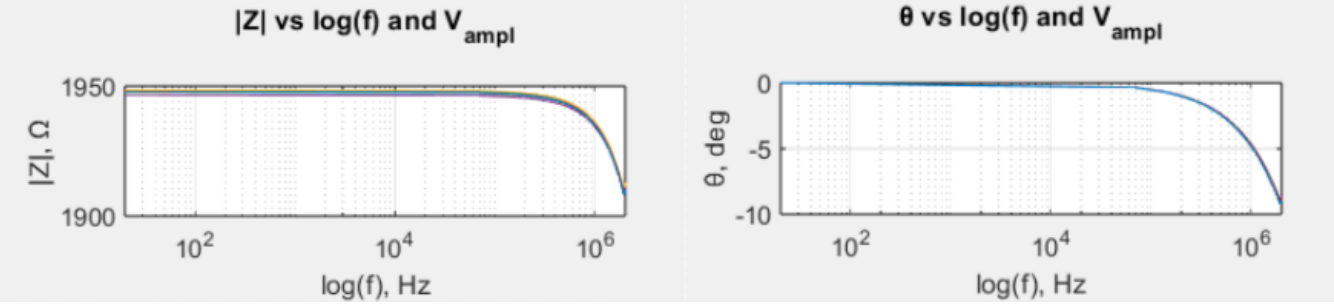

Figure 5.30: $|Z|$ and θ versus log(f) and V_{amp}, V_{rms}

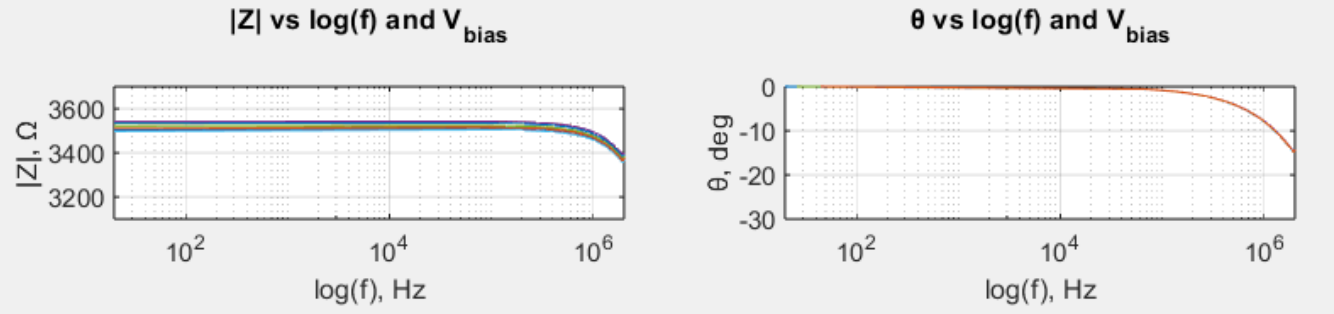

Figure 5.31: $|Z|$ and θ versus log(f) and V_{bias}

5.3 Three times coated thick cardboard

The lasing parameters to obtain the samples in figure 4.6 can be consulted in the section 4.3.2.

5.3.1 1st sample

The results for the previously depicted analysis can be seen in the figures 5.32, 5.33, 5.34, 5.35, 5.36, 5.37, 5.38.

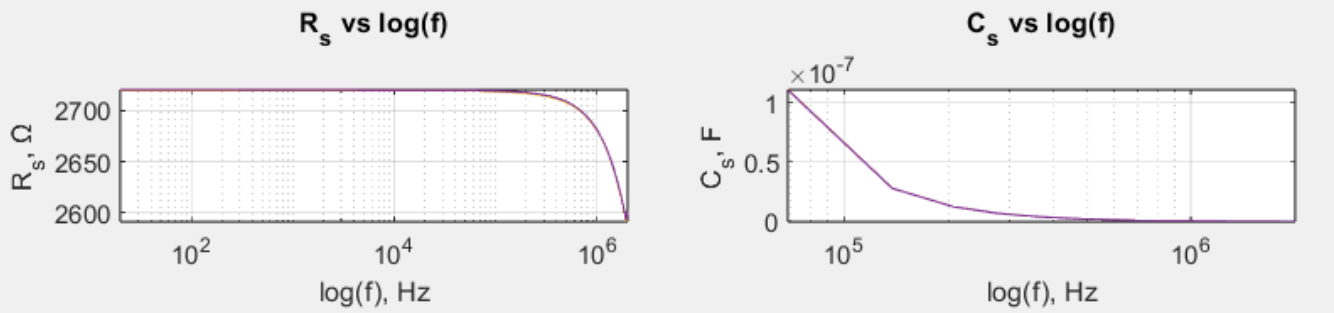

Figure 5.32: R_s and C_s versus log(f)

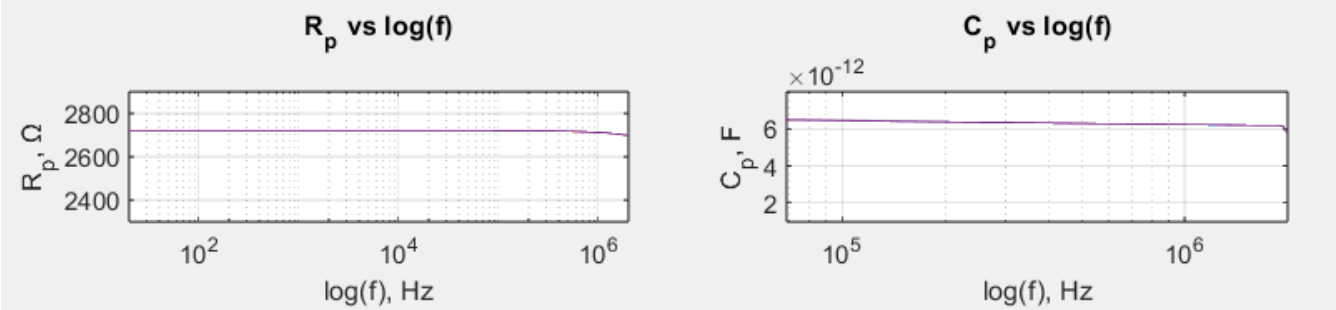

Figure 5.33: R_p and C_p versus log(f)

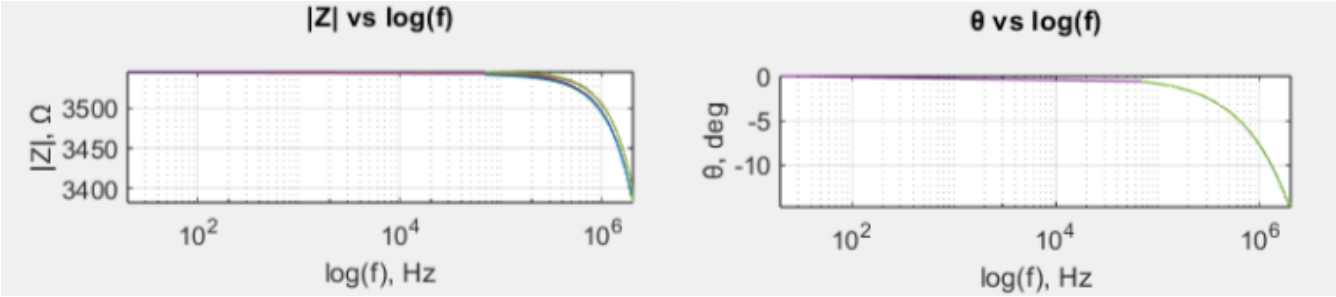

Figure 5.34: $|Z|$ and θ versus log(f)

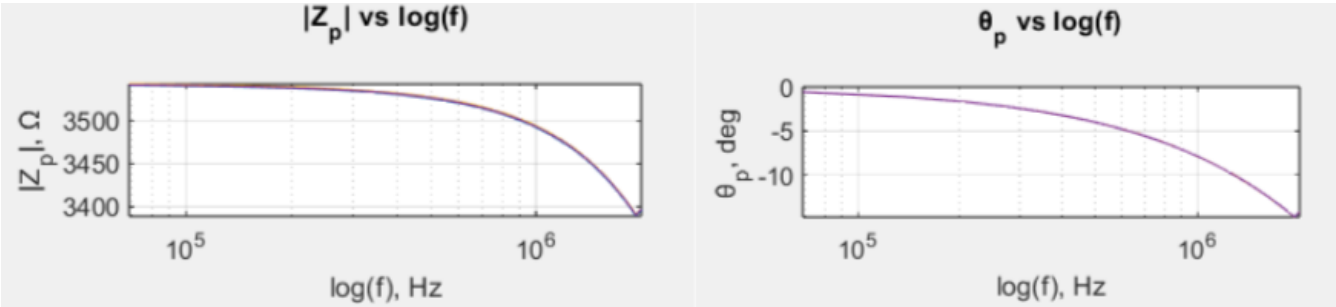

Figure 5.35: $|Z_p|$ and θ_p versus log(f)

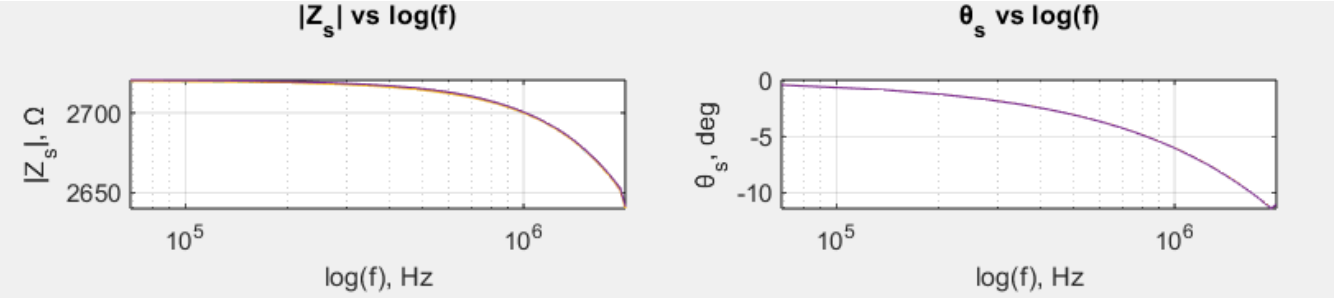

Figure 5.36: $|Z_s|$ and θ_s versus log(f)

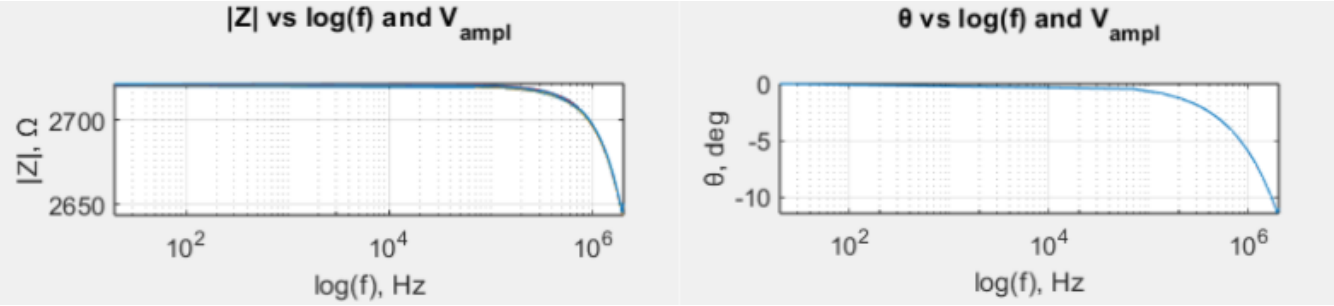

Figure 5.37: $|Z|$ and θ versus log(f) and V_{amp}, V_{rms}

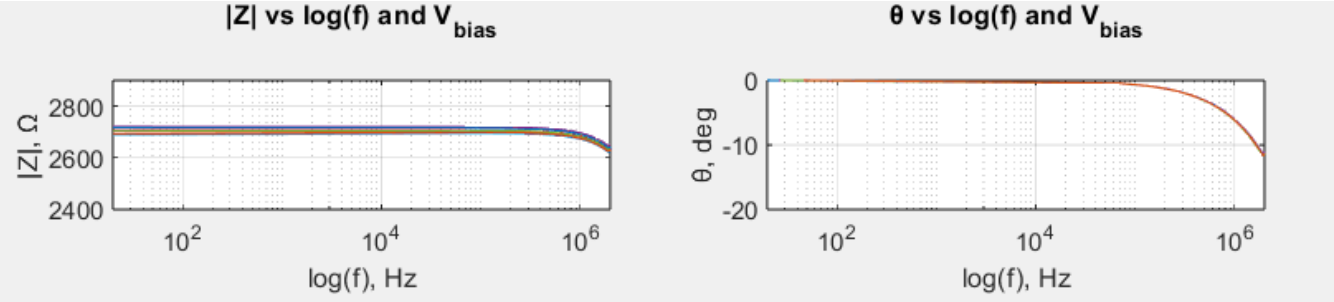

Figure 5.38: $|Z|$ and θ versus log(f) and V_{bias}

5.3.2 2nd sample

The results for the previously depicted analysis can be seen in the figures 5.39, 5.40, 5.41, 5.42, 5.43, 5.44, 5.45.

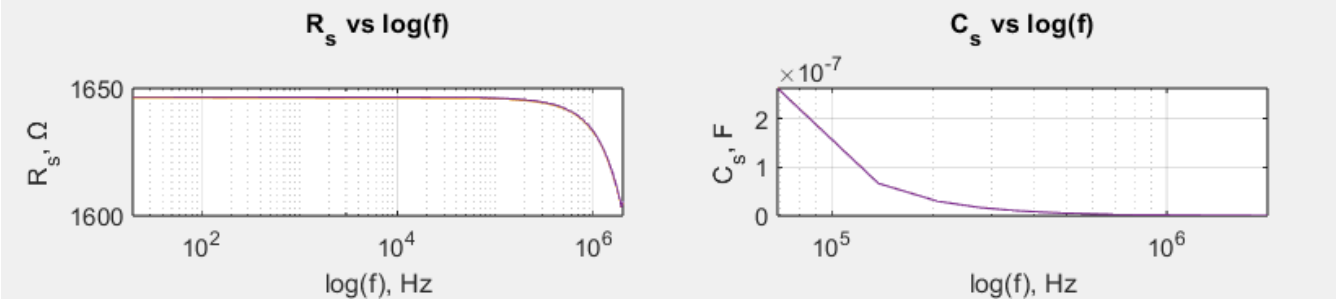

Figure 5.39: R_s and C_s versus log(f)

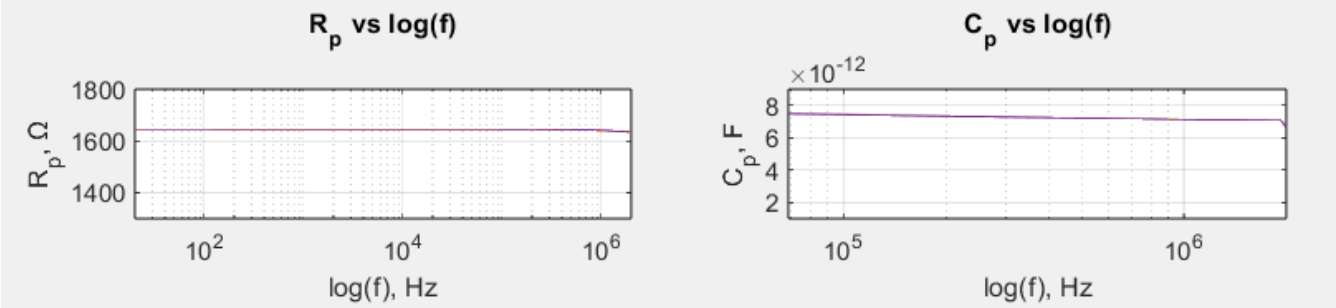

Figure 5.40: R_p and C_p versus log(f)

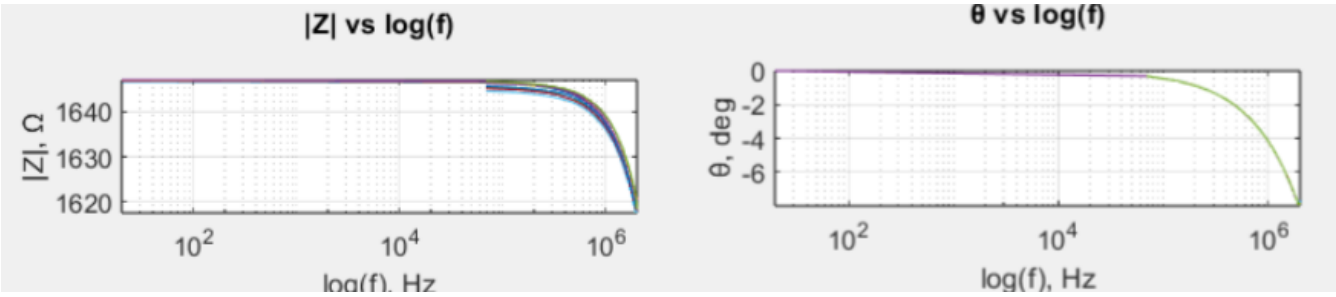

Figure 5.41: $|Z|$ and θ versus log(f)

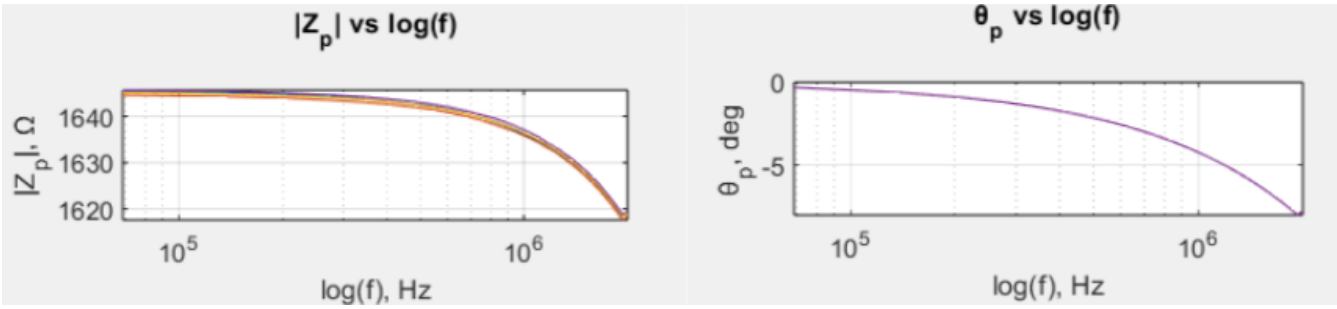

Figure 5.42: $|Z_p|$ and θ_p versus log(f)

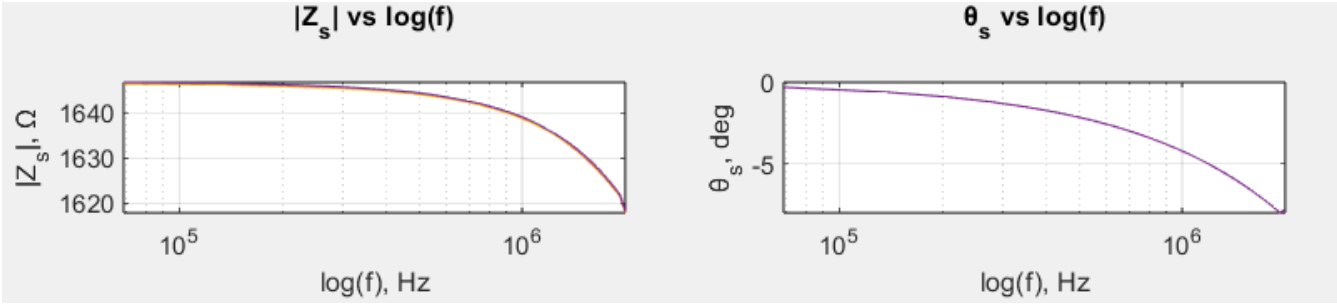

Figure 5.43: $|Z_s|$ and θ_s versus log(f)

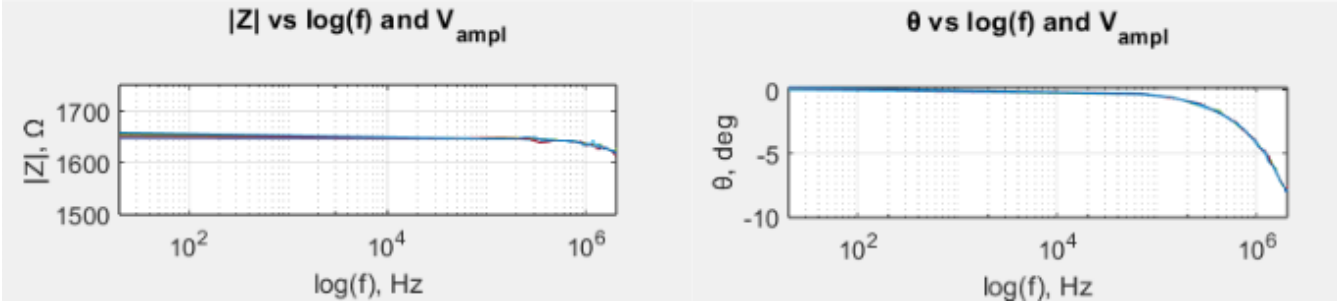

Figure 5.44: $|Z|$ and θ versus log(f) and V_{amp}, V_{rms}

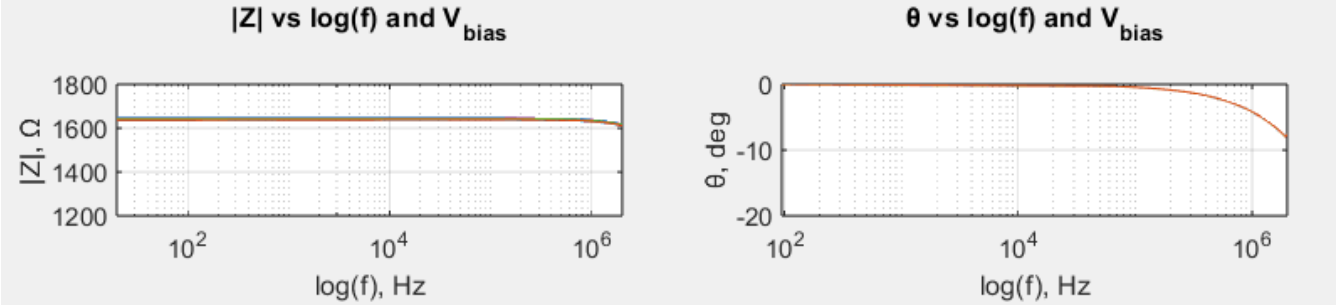

Figure 5.45: $|Z|$ and θ versus log(f) and V_{bias}

5.4 Results

The frequency behavior of the measured electrical parameters can be considered the same for all the samples and substrates under test. Considering the plots in figures 5.6, 5.13, 5.20, 5.27, 5.34 and 5.41, the curves superimpose, stating the correctness of the extraction of the series and parallel models. As a confirm to what previously stated, the correct model for each sample is the parallel one. Indeed, considering the plots in figures 5.5, 5.12, 5.19, 5.26, 5.33 and 5.40, both the parallel resistance and capacitance remain approximately constant for the whole frequency range. Hence, a couple of parallel resistance and capacitance can be considered to replicate the sample's behavior in more complex circuits that can be studied through circuit simulators. To finely select the best suited couple, the magnitude of the impedance and the correspondent phase can be calculated for each R_p/C_p couple and they can be compared with the sample's magnitude and phase. Hence, the best R_p/C_p couple is the one which minimizes the error between the two correspondent curves. The magnitude of the impedance remains nearly constant throughout the considered frequency range. Indeed, at 2 MHz, the reduction of the impedance's magnitude is at most:

- Front plate, 2x coated: 3^{rd} sample: 1.4372%
- Front plate, 3x coated: 2^{nd} sample: 4.5363%
- Thick cardboard, 3x coated: 1^{st} sample: 2.9093%

For what concerns the linearity of the samples, graphs in figure 5.9, 5.16, 5.23, 5.30, 5.37, 5.44 show the non changing behavior of the electrical parameters under study with a variation of the input amplitude. In those graphs, there's a superposition of four measures with $V_{amp} = 1\,V_{rms}$ and with $V_{amp} = 0.5\,V_{rms}$.

Considering the dependence of the sample's magnitude and phase with the bias point, graphs in figures 5.10, 5.17, 5.24, 5.31, 5.38, 5.45, four measures considering four different bias points have been superimposed. The considered values of the bias voltage have been:

- $V_{bias} = 0\,V$
- $V_{bias} = 1\,V$

- $V_{bias} = 3\,V$
- $V_{bias} = 5\,V$

Both the magnitude and the phase exhibit a non relevant changing behavior with bias point. At the frequency of 20 Hz and by applying an input signal with $V_{bias} = 5\,V$ as bias point, the variation of the true impedance's magnitude is registered to be, at most:

- Front plate, 2x coated: 2^{nd} sample: 0.9105%
- Front plate, 3x coated: 2^{nd} sample: 1.3265%
- Thick cardboard, 3x coated: 1^{st} sample: 1.1751%

5.5 Impact of the copper wires on the measurements

In order to evaluate the effect of the copper wires, the following circuit model has been considered: figure 5.46. In this section, the effect of the copper wire on the measurement of the first sample for the two times coated front plate has been considered.

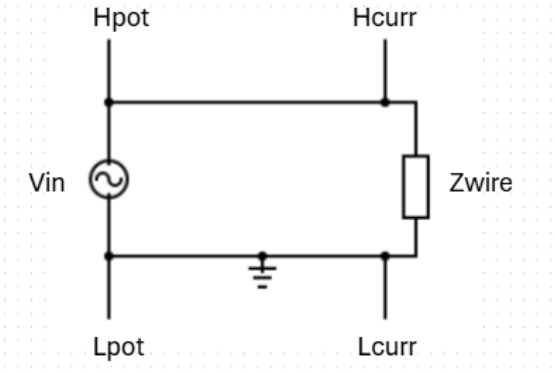

Figure 5.46: Equivalent circuit model

The measurement setup is described in the figure 5.47.

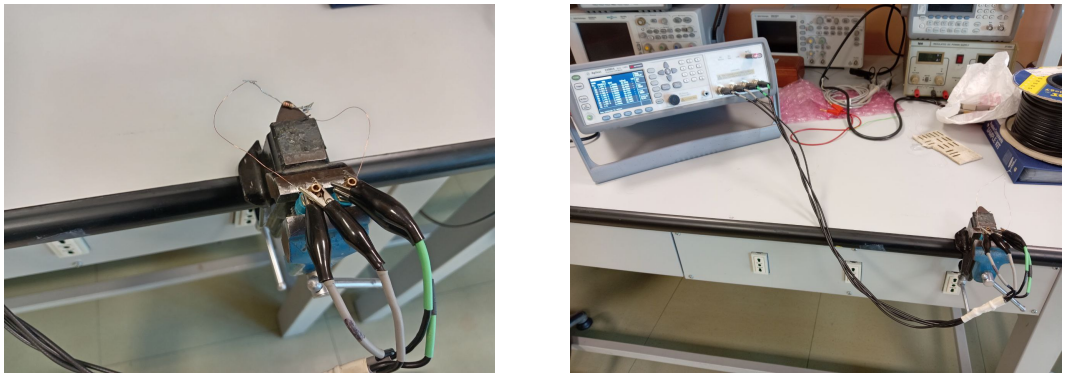

Figure 5.47: Measurement setup

Considering the equivalent circuit in figure 5.2 and the series model, figure 5.3a, the magnitude and the phase of the resulting series impedance result to be:

$$|Z_{eq}| = |Z_s + Z_w| = \sqrt{(R_s + R_w)^2 + (-\frac{1}{\omega C_s} + \omega L_w)^2} \tag{5.1}$$

$$\theta_{eq} = tan^{-1}(\frac{-\frac{1}{\omega C_s} + \omega L_w}{R_s + R_w}) \tag{5.2}$$

The figure 5.48 shows the behavior with frequency of magnitude and phase of the short.

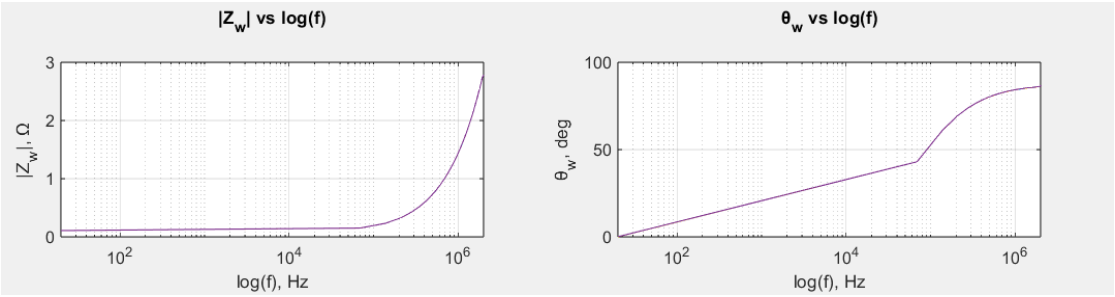

Figure 5.48: Magnitude and phase of the impedance of the short

In the following figure 5.49 are depicted the magnitude and the phase of the sample purified from the effect of the wire. At this purpose, consider the equations 5.3 and 5.4. The curves with and without the wire effect overlap, stating the negligible effect of the wire on the measurements of the samples at the considered frequency range.

$$|Z_s| = \sqrt{(R_s^2 + (-\frac{1}{\omega C_s})^2} \tag{5.3}$$

$$\theta_s = tan^{-1}(\frac{-\frac{1}{\omega C_s}}{R_s}) \tag{5.4}$$

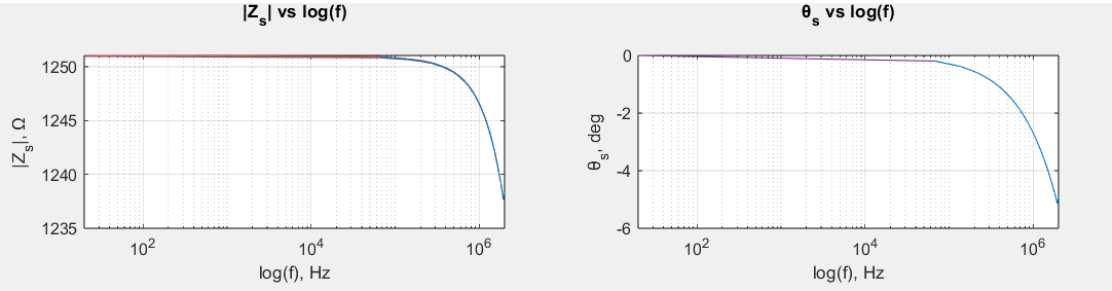

Figure 5.49: Magnitude and phase of the impedance with and without the effect of the wire

5.6 Future feasibility for the implementation of antennas and further studies

Nowadays the LIG process is deeply under study to investigate the feasibility for the implementation of low cost and eco friendly antennas working at high frequencies, from MHz to even GHz on. Authors of Mostaccio and Marrocco [2024] report the implementation of LIG antennas since 2020 by Abdul-Aziz et al. [2020], where the authors implemented a coplanar waveguide (CPW) monopole resonating at 5.8 GHz, using polyethersulfone (PES) as the substrate for the LIG process Abdul-Aziz et al. [2020].

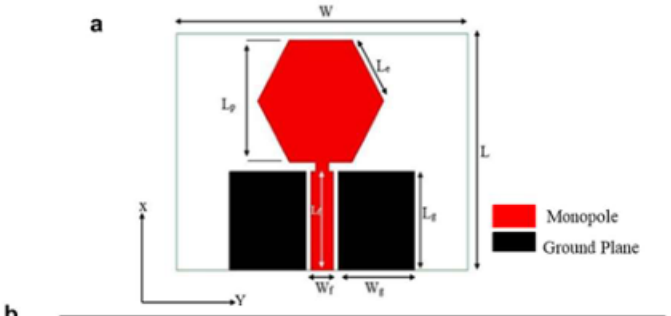

b

Geometrical parameters for the hybrid antenna in (mm)							
W	L	L_p	L_e	L_g	L_f	W_f	g
30	25	12.5	7.2	10	10	2.6	0.3

Figure 5.50: a)Geometry of the antenna b)Structural design parameters Abdul-Aziz et al. [2020]

The authors of Mostaccio and Marrocco [2024] also report the implementation in literature of LIG based patch antennas and RFID tags. Furthermore, they implemented LIG based rectangular monopole, ring monopole and rectangular dipole antennas. With the optimized set of lasing parameters authors achieved a sheet resistance $R_{sh} \simeq 12\,\Omega/\square$ which can be suited for the antenna fabrication. Authors of Abdul-Aziz et al. [2020]

achieved a mean value of $R_{sh} \simeq 8\,\Omega/\square$ for the implementation of their coplanar waveguide. Another example of LIG based antennas is from the paper of Chietera et al. [2022]. The authors implemented an Ultra High Frequency (UHF) RFID LIG on Kapton antenna, which frequency range is between 860 MHz and 960 MHz. Figure 5.51.

Figure 5.51: LIG on Kapton RFID: junction's length: $29.7\,mm$; junction's width: $0.95\,mm$ Chietera et al. [2022]

The authors obtained a side-to-side total resistance of approximately 1 kΩ with a correspondent sheet resistance of $R_{sh} \simeq 85\,\Omega/\square$. The performance of the implemented RFID tag in terms of the estimated maximum reading distance is in figure 5.52.

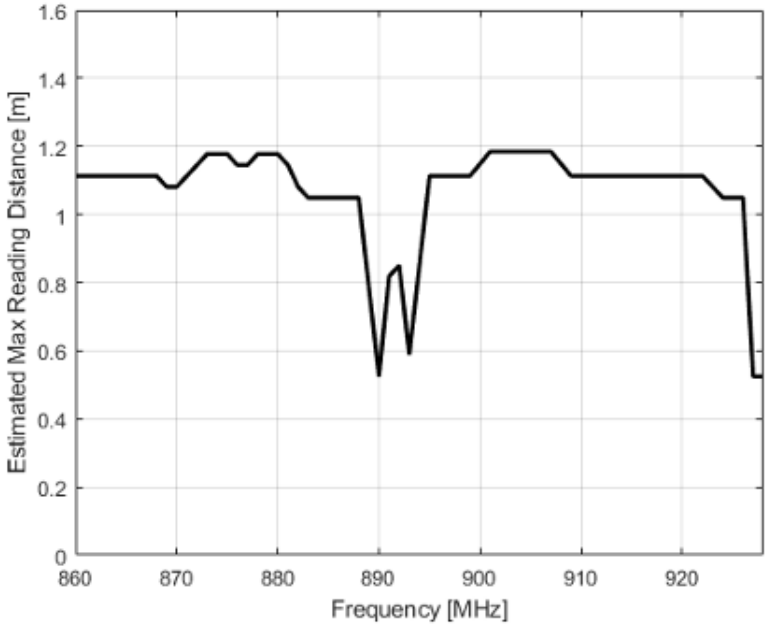

Figure 5.52: Estimated maximum reading distance for LIG on Kapton RFID tag Chietera et al. [2022]

This can be explained by the higher resistivity of the LIG pattern in comparison to conductors. The authors also report that the reason of that is the designed geometry layout, which is not well suitable for the LIG implementation: there's a very narrow path width which makes inevitably increase the resistance. In the study presented in this document, the best result achieved in terms of pattern's resistance is by considering the 5^{th} sample of the three times flame retardant spray coated thick cardboard. See the

appendix, figure A.43. In this case, the side-to-side resistance at 20 Hz results to be of $R \simeq 895\,\Omega$. The relative sheet resistance can be calculated as:

$$R_{sh} = \frac{\rho}{t} = R\frac{W}{L} \tag{5.5}$$

Where:

- ρ : resistivity of the material, $\Omega\, m$
- t: thickness of the sample, m
- W: width of the sample, m
- L: length of the sample, m

The sheet resistance for that sample is $R_{sh} \simeq 119\,\Omega/\square$.

5.7 Conclusions

In light of this, future studies can investigate the possibility to implement the technology depicted in this work for the realization of RFID tags on paper-based materials used for the agro-industry packages. This, even if the performances should be worse than the case of Chietera et al. [2022] due to the higher sheet resistance of the optimized obtained samples: $R_{sh} \simeq 119\,\Omega/\square$. Further studies can also fucus on to deeply optimize the lasing parameters in order to achieve a minimization of the sheet resistance. Other improvements may address the method of depositing the flame retardant spray on the substrate to achieve a more uniform and predictable layer of the product on the material under test. Furthermore, the obtained samples are linear both in DC and AC. The parallel model consisting in a parallel resistance and capacitance, since they approximately exhibit a non changing behavior throughout the frequency range, they well replicate the sample's behavior and hence that model can be employed for simulating the sample in more complex systems through circuit simulators. All these improvements can make the LIG process applied to the agro-industry packaging materials a key factor for the eco friendly and sustainable mass production. Furthermore, such integrated on-package devices can deeply revolutionize the storage and quality control of foods and drinks, leading to highly functionalized but at the same time environmental friendly packages.

Appendix A

Plots for the AC analysis

A.0.1 Two times coated front plate

3^{rd} sample

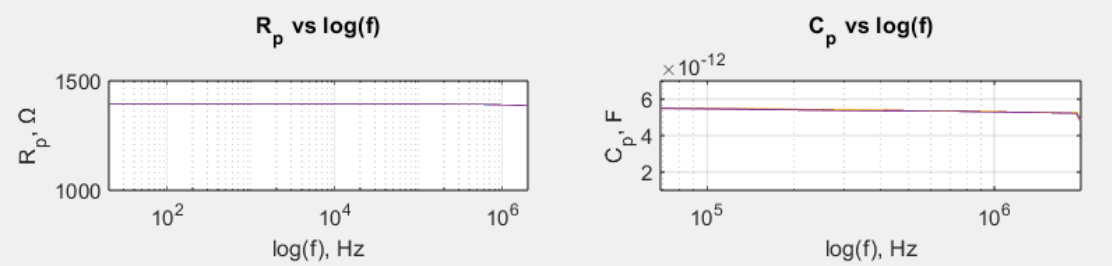

Figure A.1: R_p and C_p versus log(f)

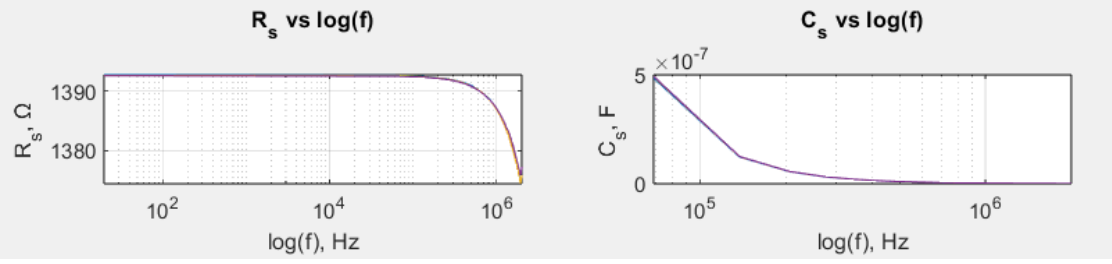

Figure A.2: R_s and C_s versus log(f)

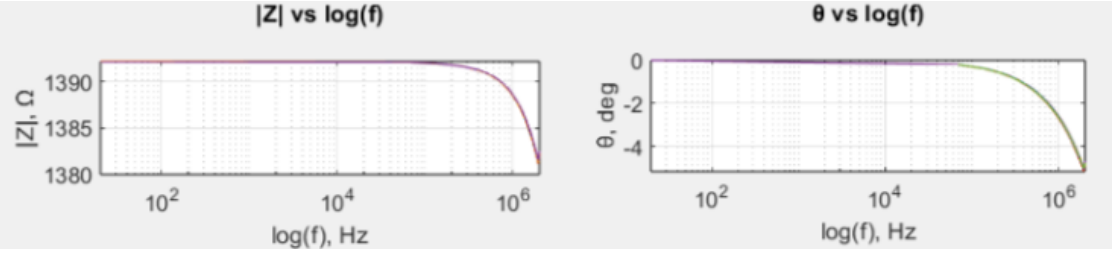

Figure A.3: $|Z|$ and θ versus log(f)

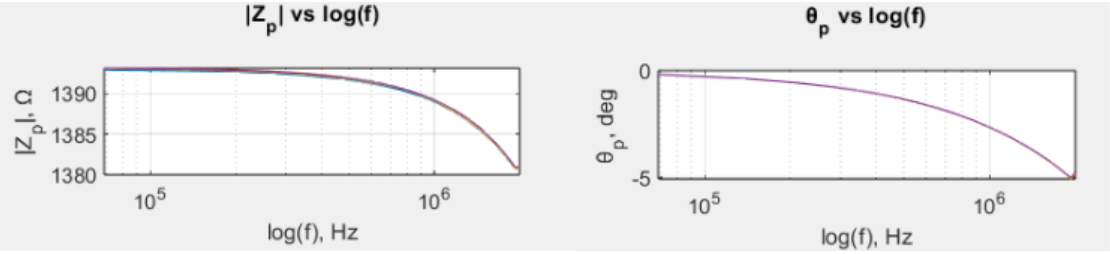

Figure A.4: $|Z_p|$ and θ_p versus log(f)

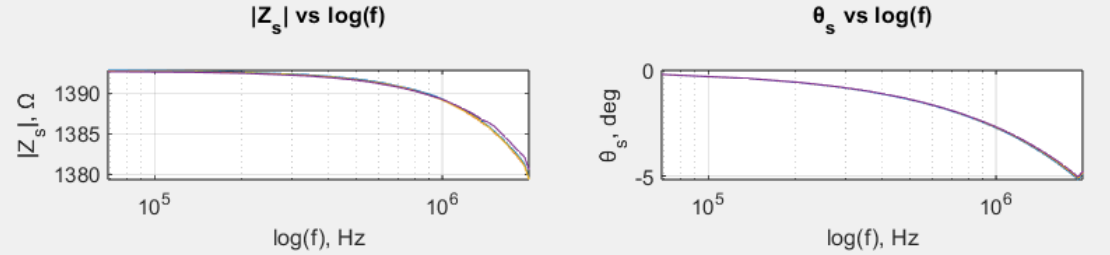

Figure A.5: $|Z_s|$ and θ_s versus log(f)

4^{th} sample

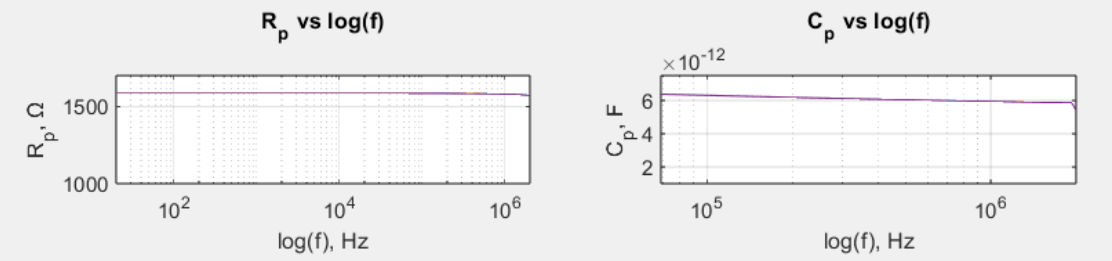

Figure A.6: R_p and C_p versus log(f)

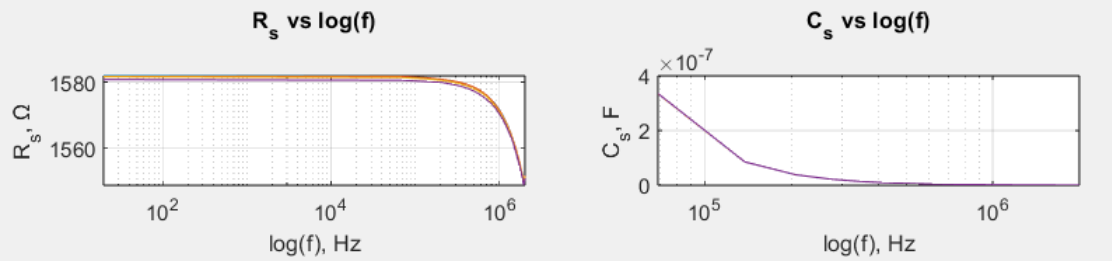

Figure A.7: R_s and C_s versus log(f)

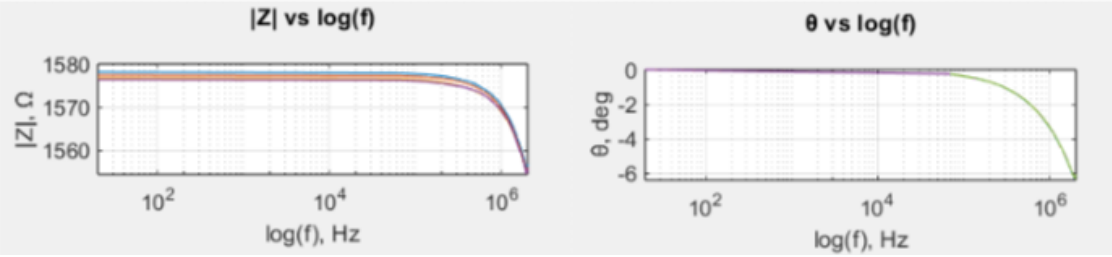

Figure A.8: $|Z|$ and θ versus log(f)

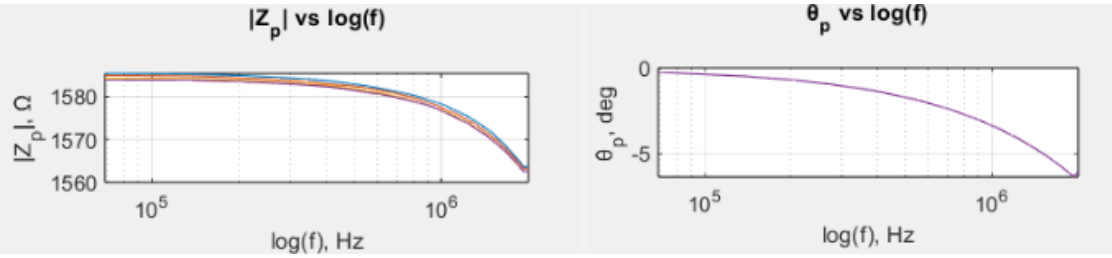

Figure A.9: $|Z_p|$ and θ_p versus log(f)

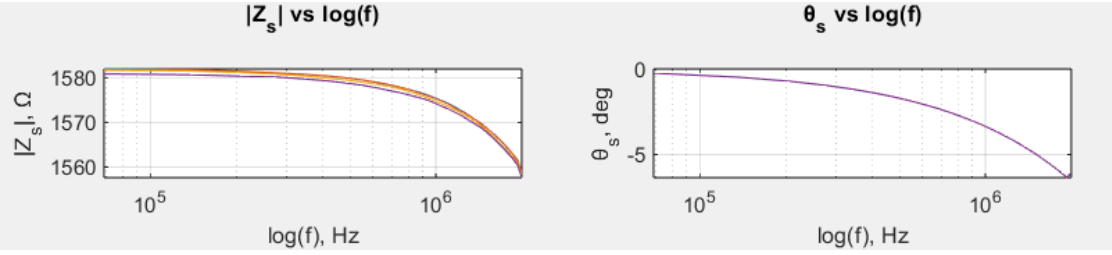

Figure A.10: $|Z_s|$ and θ_s versus log(f)

5^{th} sample

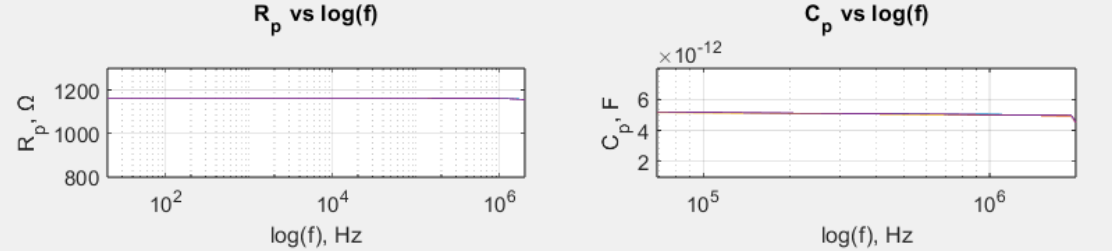

Figure A.11: R_p and C_p versus log(f)

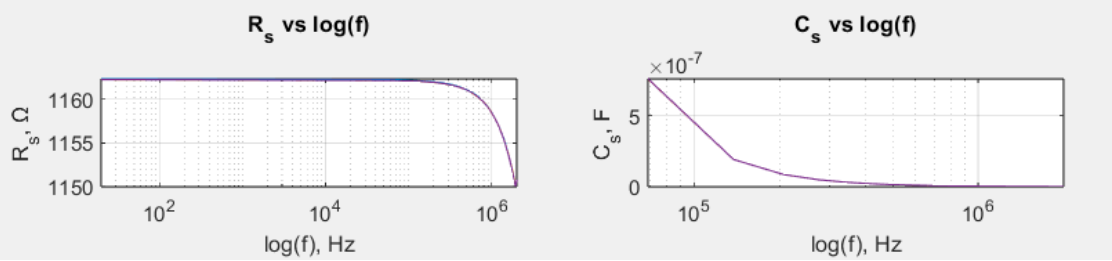

Figure A.12: R_s and C_s versus log(f)

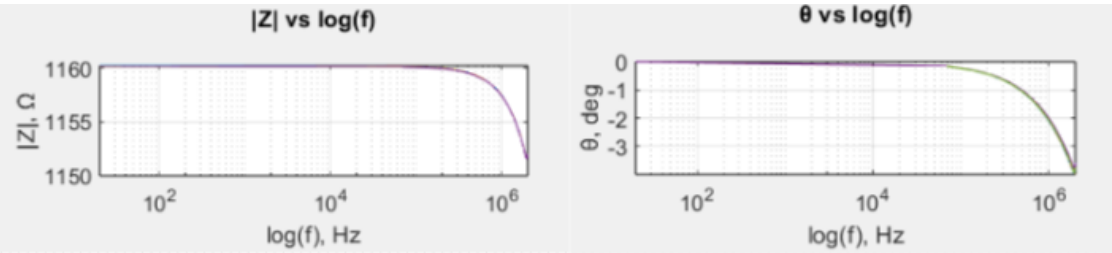

Figure A.13: $|Z|$ and θ versus log(f)

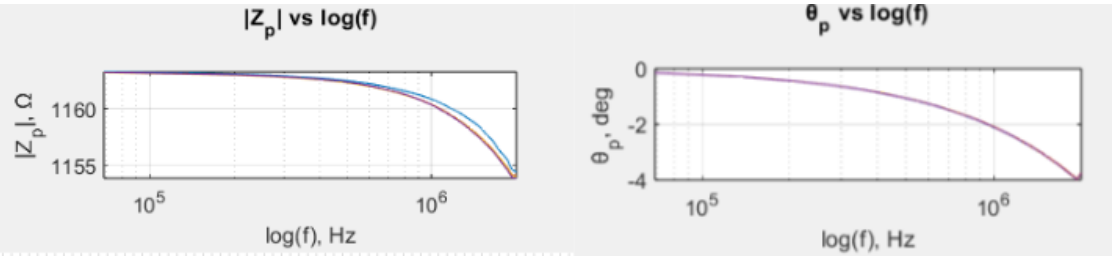

Figure A.14: $|Z_p|$ and θ_p versus log(f)

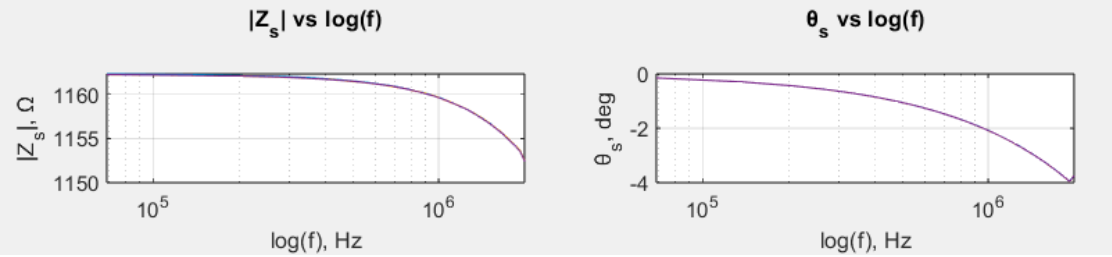

Figure A.15: $|Z_s|$ and θ_s versus log(f)

A.0.2 Three times coated front plate

3^{rd} sample

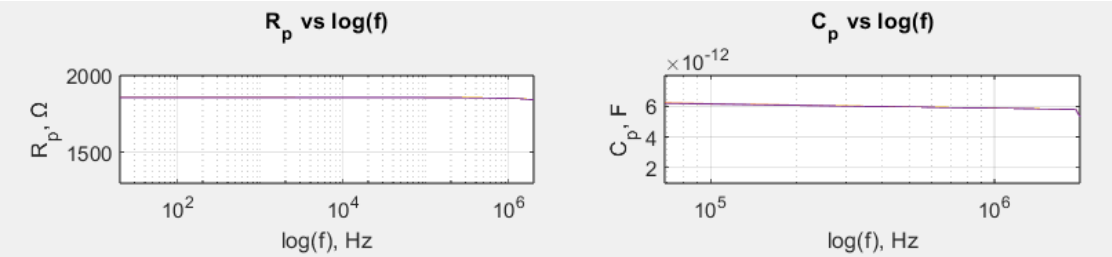

Figure A.16: R_p and C_p versus log(f)

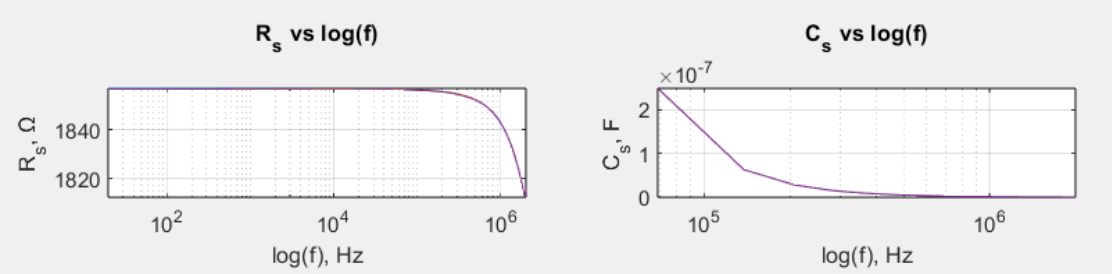

Figure A.17: R_s and C_s versus log(f)

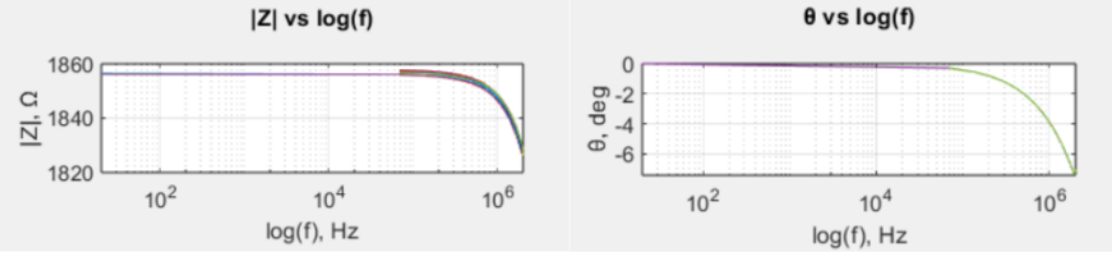

Figure A.18: $|Z|$ and θ versus log(f)

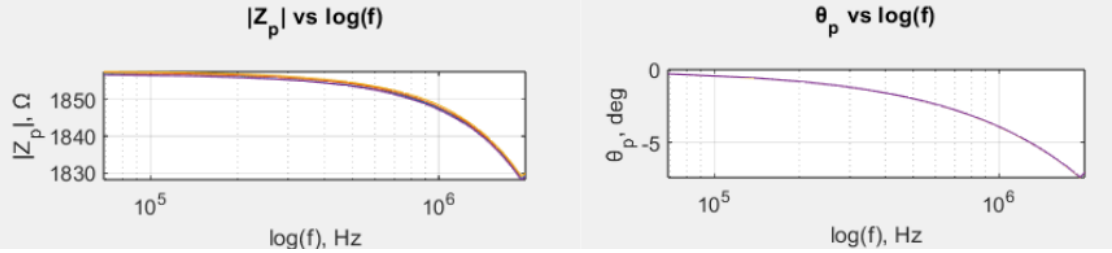

Figure A.19: $|Z_p|$ and θ_p versus log(f)

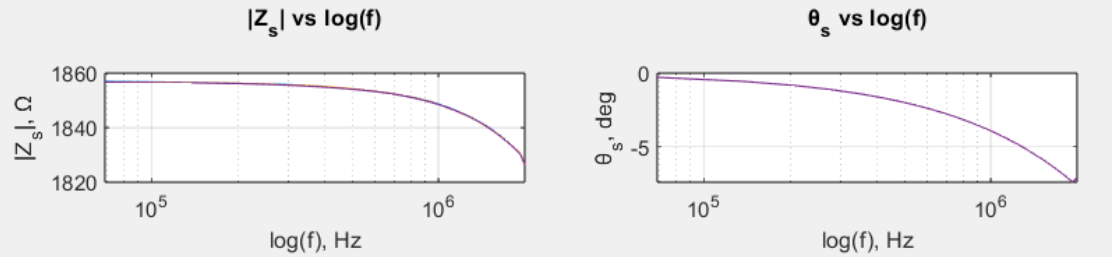

Figure A.20: $|Z_s|$ and θ_s versus log(f)

4^{th} sample

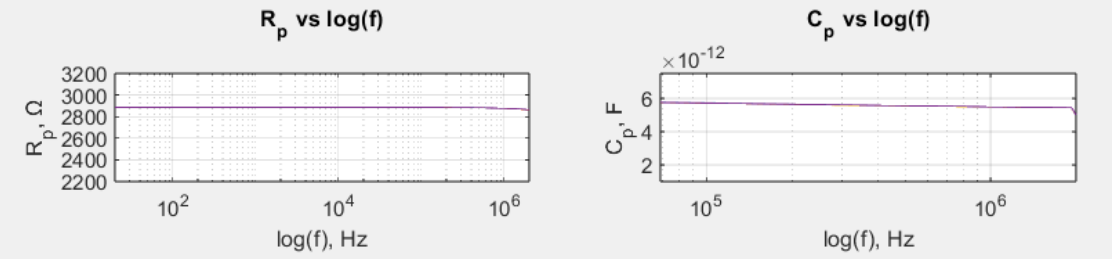

Figure A.21: R_p and C_p versus log(f)

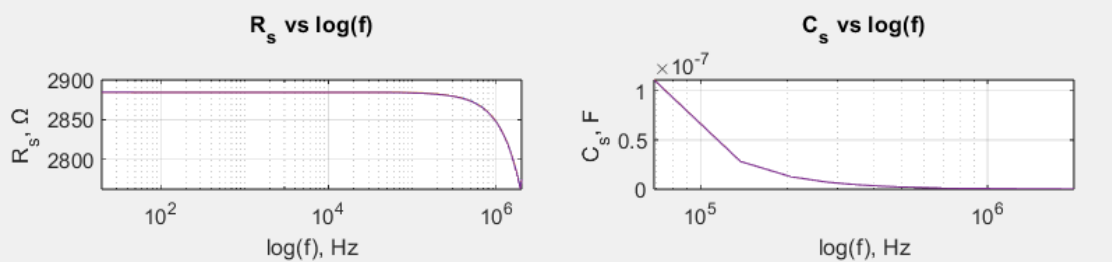

Figure A.22: R_s and C_s versus log(f)

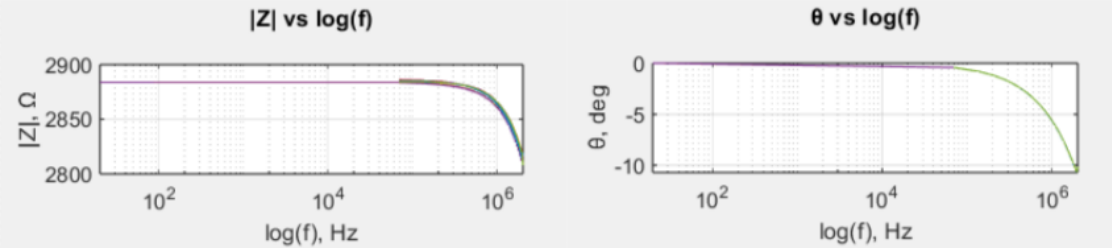

Figure A.23: $|Z|$ and θ versus log(f)

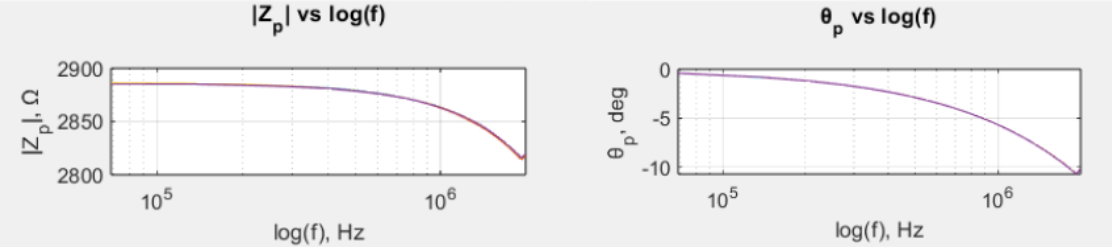

Figure A.24: $|Z_p|$ and θ_p versus log(f)

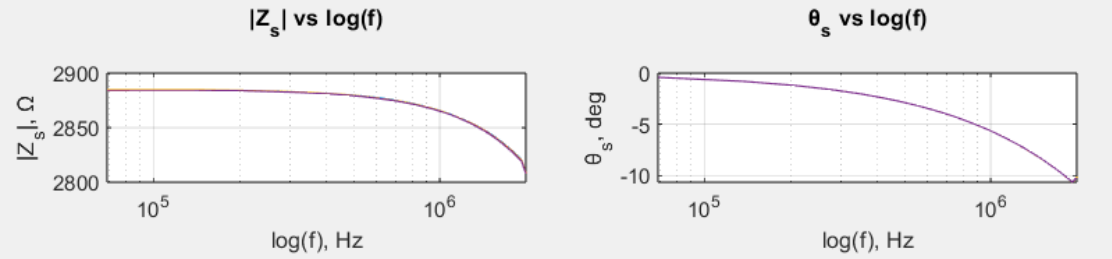

Figure A.25: $|Z_s|$ and θ_s versus log(f)

5^{th} sample

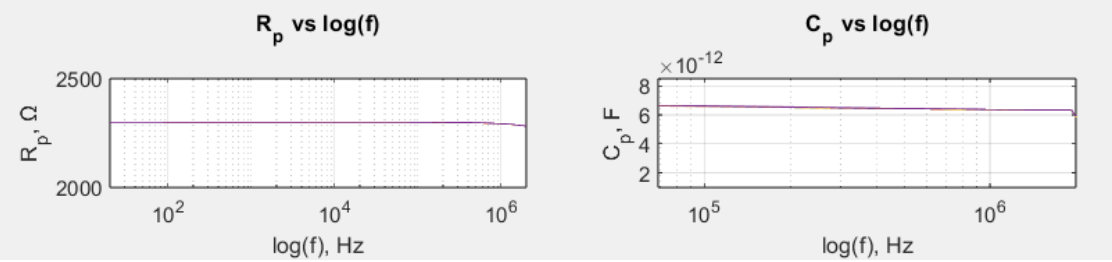

Figure A.26: R_p and C_p versus log(f)

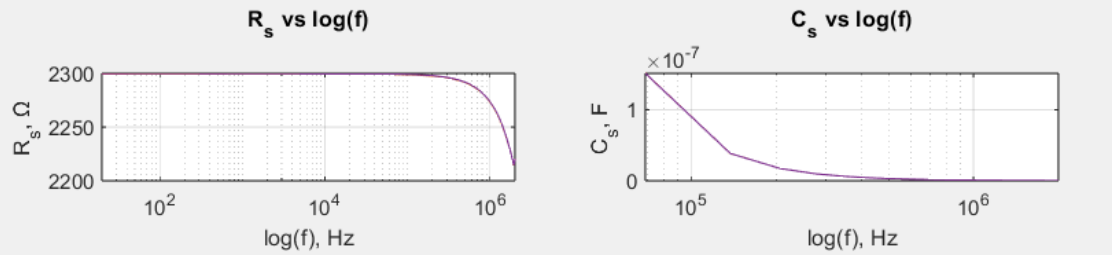

Figure A.27: R_s and C_s versus log(f)

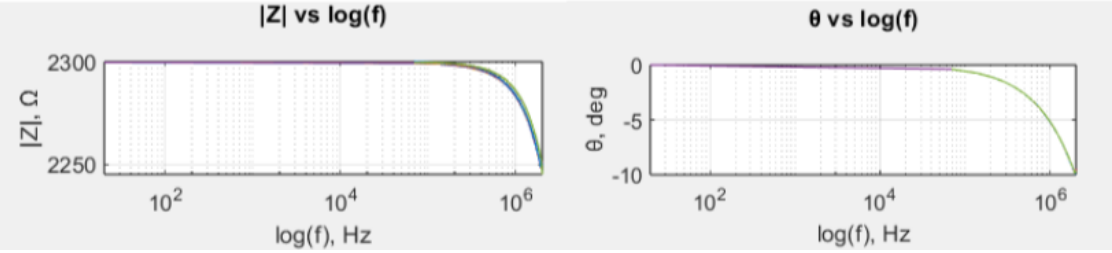

Figure A.28: $|Z|$ and θ versus log(f)

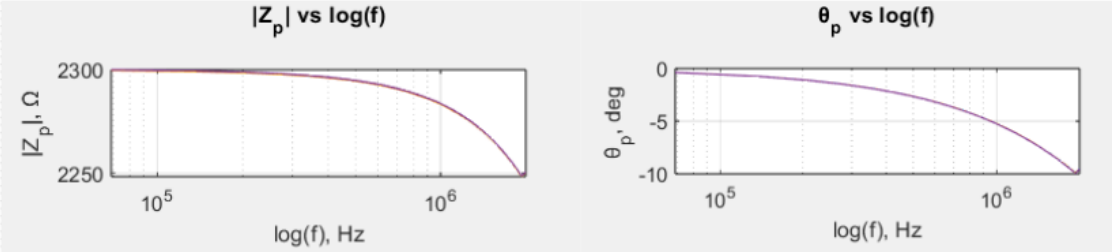

Figure A.29: $|Z_p|$ and θ_p versus log(f)

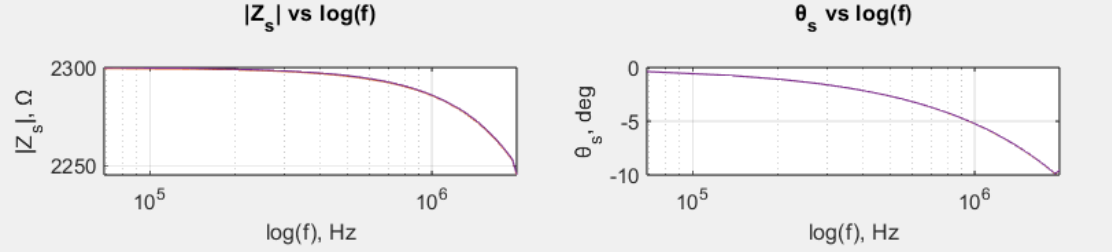

Figure A.30: $|Z_s|$ and θ_s versus log(f)

A.0.3 Three times coated thick cardboard

3^{rd} sample

Figure A.31: R_p and C_p versus log(f)

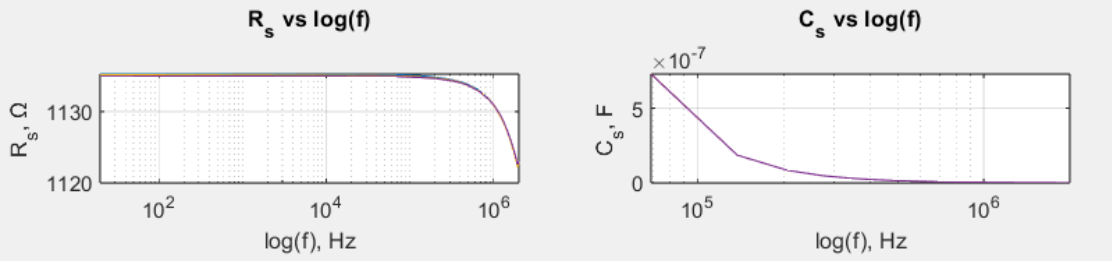

Figure A.32: R_s and C_s versus log(f)

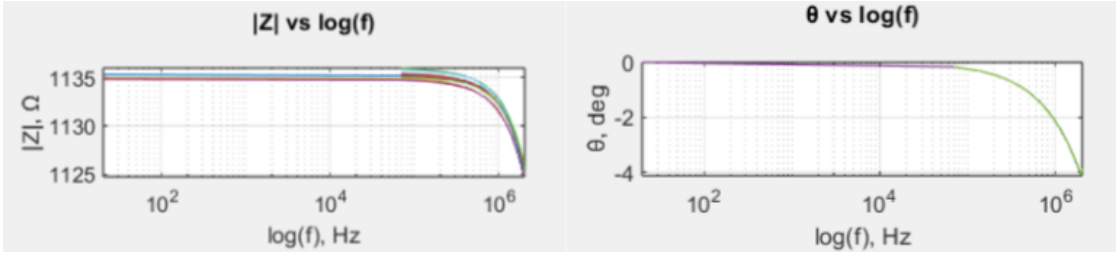

Figure A.33: $|Z|$ and θ versus log(f)

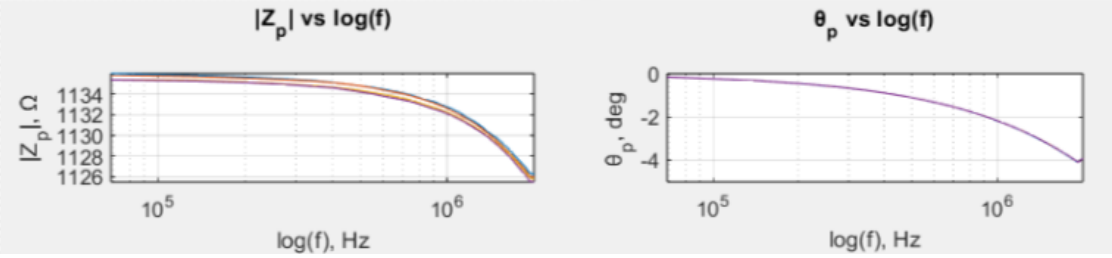

Figure A.34: $|Z_p|$ and θ_p versus log(f)

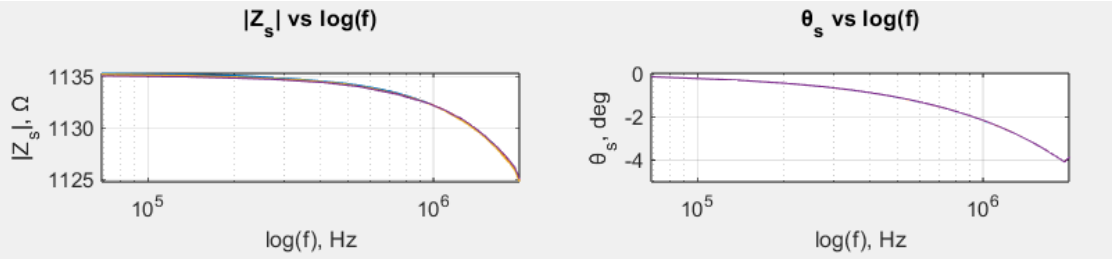

Figure A.35: $|Z_s|$ and θ_s versus log(f)

4^{th} sample

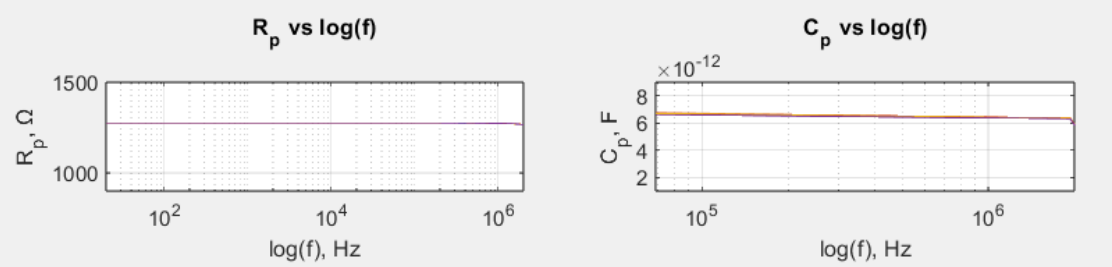

Figure A.36: R_p and C_p versus log(f)

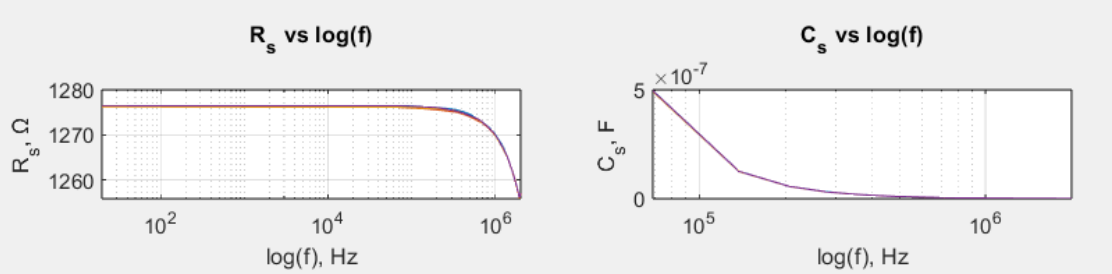

Figure A.37: R_s and C_s versus log(f)

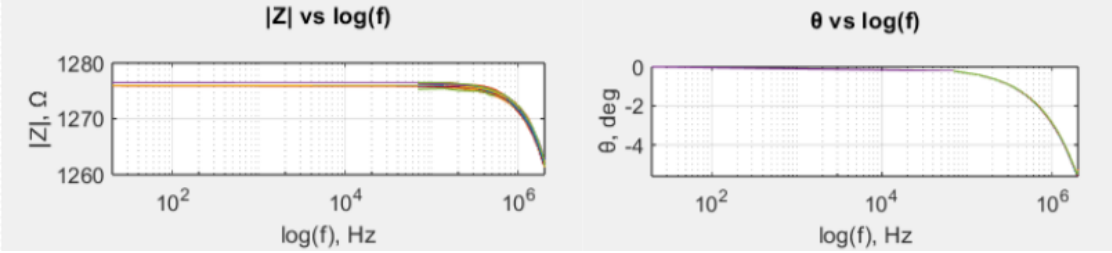

Figure A.38: $|Z|$ and θ versus log(f)

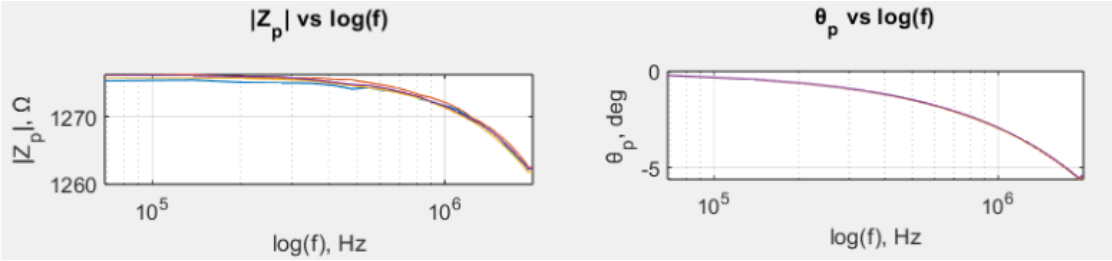

Figure A.39: $|Z_p|$ and θ_p versus log(f)

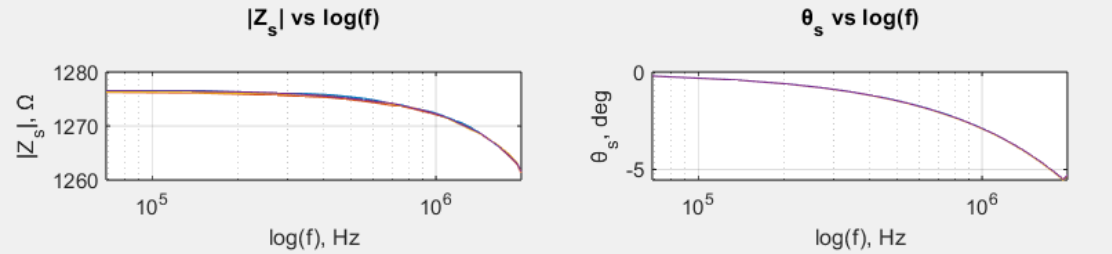

Figure A.40: $|Z_s|$ and θ_s versus log(f)

5^{th} sample

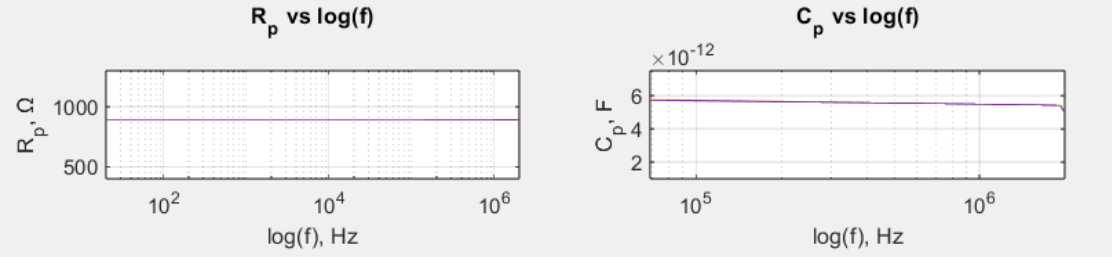

Figure A.41: R_p and C_p versus log(f)

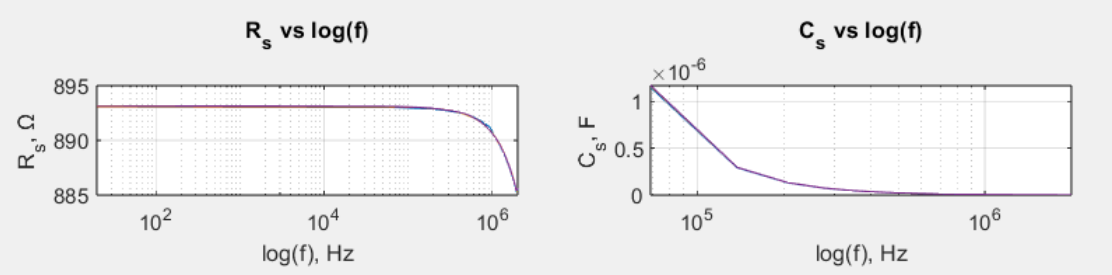

Figure A.42: R_s and C_s versus log(f)

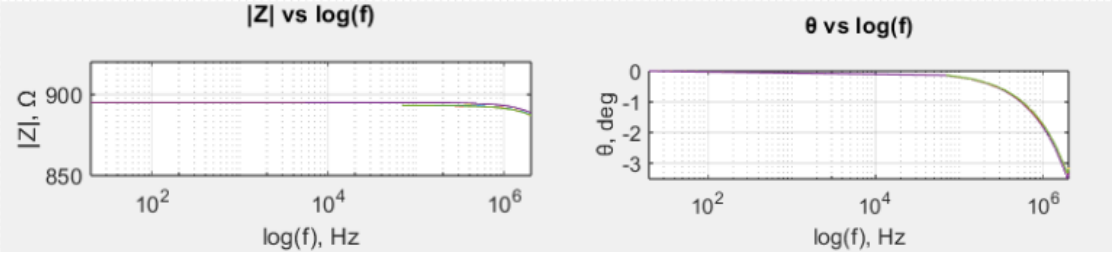

Figure A.43: $|Z|$ and θ versus log(f)

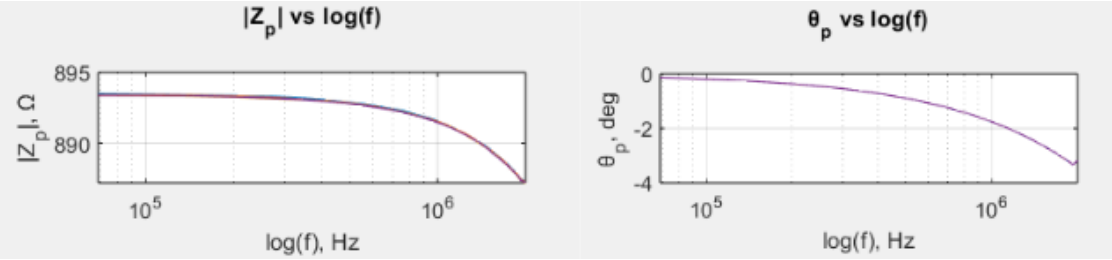

Figure A.44: $|Z_p|$ and θ_p versus log(f)

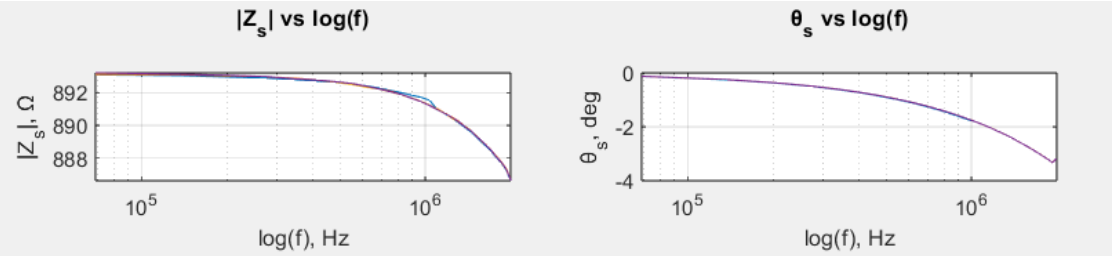

Figure A.45: $|Z_s|$ and θ_s versus log(f)

Bibliography

Mohamed R. R. Abdul-Aziz, Shaimaa A. Mohassieb, Nermeen A. Eltresy, Moataz M. K. Yousef, Badawi Anis, Sameh O. Abdellatif, and Ahmed S. G. Khalil. Enhancing the performance of polygon monopole antenna using graphene/tmdcs heterostructures. *IEEE Transactions on Nanotechnology*, 19:269–273, 2020. doi: 10.1109/TNANO.2020.2974994.

T. Araki, K. Li, D. Suzuki, T. Abe, R. Kawabata, T. Uemura, S. Izumi, S. Tsuruta, N. Terasaki, Y. Kawano, and T. Sekitani. Broadband photodetectors and imagers in stretchable electronics packaging. *Advanced Materials*, 36, 2023. URL https://www.semanticscholar.org/paper/Broadband-Photodetectors-and-Imagers-in-Stretchable-Araki-Li/3c6dcd6b9cdcdc3e17d2f09f1662eb73fa06a354.

F. Banhart, J. Kotakoski, and A. Krasheninnikov. Structural defects in graphene. *ACS Nano*, 5(1):26–41, 2011. doi: 10.1021/nn102598m.

K. B. Biji, C. N. Ravishankar, C. O. Mohan, and T. K. S. Srinivasa Gopal. Smart packaging systems for food applications: a review. *Journal of Food Science and Technology*, 52(10):6125–6135, Oct. 2015. doi: 10.1007/s13197-015-1766-7.

Francesco Paolo Chietera, Riccardo Colella, Akash Verma, Eleonora Ferraris, Carola Esposito Corcione, Carmen L. Moraila-Martinez, Denice Gerardo, Yann Houeix Acid, Almudena Rivadeneyra, and Luca Catarinucci. Laser-induced graphene, fused filament fabrication, and aerosol jet printing for realizing conductive elements of uhf rfid antennas. *IEEE Journal of Radio Frequency Identification*, 6:601–609, 2022. doi: 10.1109/JRFID.2022.3167518.

Y. Chyan, R. Ye, Y. Li, S. P. Singh, C. J. Arnusch, and J. M. Tour. Laser-induced graphene by multiple lasing: Toward electronics on cloth, paper, and food. *ACS Nano*, 12(3):2176–2183, 2018. doi: 10.1021/acsnano.7b08539.

European Commission. Packaging waste, a. URL https://environment.ec.europa.eu/topics/waste-and-recycling/packaging-waste_en.

European Commission. Food contact materials, b. URL https://food.ec.europa.eu/food-safety/chemical-safety/food-contact-materials_en.

Carlos M Fernandez, Joel Alves, Pedro Dinis Gaspar, Tânia M Lima, and Pedro D Silva. Innovative processes in smart packaging. a systematic review. *Journal of the Science of Food and Agriculture*, 103(3):986–1003, 2023. doi: https://doi.org/10.1002/jsfa.11863. URL https://scijournals.onlinelibrary.wiley.com/doi/abs/10.1002/jsfa.11863.

A. R. Ruiz Hernández, A. Gutierrez Cruz, and J. Campos-Delgado. *Chemical Vapor Deposition Synthesis of Graphene on Copper Foils*. IntechOpen, 2022. doi: 10.5772/intechopen.106058.

Yihe Huang, Lei Zeng, Chongguang Liu, Desen Zeng, Zhu Liu, Xuqing Liu, X. Zhong, W. Guo, and Lin Li. Laser direct writing of heteroatom (n and s)-doped graphene from a polybenzimidazole ink donor on polyethylene terephthalate polymer and glass substrates. *Small*, 14 44:e1803143, 2018. doi: 10.1002/smll.201803143.

Y. Jung, J. Min, J. Choi, J. Bang, S. Jeong, K. R. Pyun, J. Ahn, Y. Cho, S. Hong, S. Hong, J. Lee, and S. H. Ko. Smart paper electronics by laser-induced graphene for biodegradable real-time food spoilage monitoring. *Applied Materials Today*, 29:101589, 2022. doi: 10.1016/j.apmt.2022.101589.

S. Khalid, S. A. Hassan, H. Javaid, M. Zahid, M. Naeem, Z. F. Bhat, G. Abdi, and R. M. Aadil. Factors responsible for spoilage, drawbacks of conventional packaging, and advanced packaging systems for tomatoes. *J. Agric. Food Res.*, 15:100962, 2024. doi: 10.1016/j.jafr.2023.100962.

Bohdan Kulyk, Beatriz F. R. Silva, Alexandre F. Carvalho, Sara Silvestre, António J. S. Fernandes, Rodrigo Martins, Elvira Fortunato, and Florinda M. Costa. Laser-induced graphene from paper for mechanical sensing. *ACS Applied Materials & Interfaces*, 13(8):10210–10221, 2021. doi: 10.1021/acsami.0c20270. URL https://doi.org/10.1021/acsami.0c20270. PMID: 33619955.

Ibrahim Lawan, Panuwat Luengrojanakul, Krittapas Charoensuk, Hariharan Argunam, Cheol-Hee Ahn, and Sarawut Rimdusit. Improvements in properties of polybenzoxazine-based laser-induced graphene (lig) by alloying with polyimide and modeling of production process. *Nanoscale Adv.*, 6:1556–1564, 2024. doi: 10.1039/D3NA01026K. URL http://dx.doi.org/10.1039/D3NA01026K.

T. D. Le, H.-P. Phan, S. Kwon, S. Park, Y. Jung, J. Min, B. J. Chun, and et al. Recent advances in laser-induced graphene: mechanism, fabrication, properties, and applications in flexible electronics. *Advanced Functional Materials*, 32(48), 2022. doi: 10.1002/adfm.202205158.

J. Lin, Z. Peng, and Y. Liu et al. Laser-induced porous graphene films from commercial polymers. *Nature Communications*, 5(5714), 2014. doi: 10.1038/ncomms6714.

J. Liu, H. Ji, and X. Lv et al. Laser-induced graphene (lig)-driven medical sensors for health monitoring and diseases diagnosis. *Microchimica Acta*, 189, 2022. doi: 10.1007/s00604-021-05157-6.

S. Malik, Y. Zhao, Y. He, X. Zhao, H. Li, L. G. Occhipinti, M. Wang, S. C. Discovery, U. C. London, T. Place, K. London, W. 7JE, C. G. Centre, U. O. Cambridge, J. T. Avenue, and C. C. 0FA. Spray-coated graphene/quantum dots paper-based photodetectors, 2023. URL https://www.semanticscholar.org/paper/Spray-Coated-Graphene-Quantum-Dots-Paper-Based-Malik-Zhao/13493a9c22951f35abcf2c1d0c40421b0a35fd34.

U. Misra, N. Dixit, and S. P. Singh. Effect of laser parameters on laser-induced graphene filter fabrication and its performance for desalination and water purification. *ACS Applied Materials & Interfaces*, 15(6):7899–7910, 2023. doi: 10.1021/acsami.2c17106.

A. Mostaccio and G. Marrocco. Design, prototyping, and characterization of laser-induced graphene antennas on flexible substrates: consolidating current knowledge. *IEEE Antennas & Propagation Magazine*, pages 2–12, 2024. doi: 10.1109/MAP.2024.3457309.

Tomás Pinheiro, Ricardo Correia, Maria Morais, João Coelho, Elvira Fortunato, M. Goreti F. Sales, Ana C. Marques, and Rodrigo Martins. Water peel-off transfer of electronically enhanced, paper-based laser-induced graphene for wearable electronics. *ACS Nano*, 16(12):20633–20646, 2022. doi: 10.1021/acsnano.2c07596. URL https://doi.org/10.1021/acsnano.2c07596. PMID: 36383513.

C. Robert, J. L. Sinclair, P. V. Suter, and P. Coveney. Micromechanical exfoliation of graphene on the atomistic scale. *Physical Chemistry Chemical Physics*, 21(10):5716–5722, 2019. doi: 10.1039/C8CP07796G.

Aivaras Sartanavičius, Justina Žemgulytė, Paulius Ragulis, Karolis Ratautas, and Romualdas Trusovas. Laser-induced graphene in polyimide for antenna applications. *Crystals*, 13(7), 2023. ISSN 2073-4352. doi: 10.3390/cryst13071003. URL https://www.mdpi.com/2073-4352/13/7/1003.

R. Ye, D. James, and J. Tour. Laser-induced graphene: From discovery to translation. *Advanced Materials*, 31, 2018. doi: 10.1002/adma.201803621.

J. Zhang. Synthesis methods for graphene, 2022.